Design and Fabrication of micro- and nano-dielectric structures for imaging and focusing at optical frequencies

by

Satoshi Takahashi

M.S., Mechanical Engineering (2006)
Massachusetts Institute of Technology

Submitted to the Department of Mechanical Engineering
in partial fulfillment of the requirements for the degree of

Doctor of Philosophy in Mechanical Engineering

at the

MASSACHUSETTS INSTITUTE OF TECHNOLOGY

June 2011

Author .....
Department of Mechanical Engineering
February 15, 2011

Certified by .....
George Barbastathis
Professor of Mechanical Engineering
Thesis Supervisor

Accepted by .....
David E. Hardt
Chairman, Department Committee on Graduate Students

Design and Fabrication of micro- and nano- dielectric structures for imaging and focusing at optical frequencies

by

Satoshi Takahashi

Submitted to the Department of Mechanical Engineering
on February 20, 2011, in partial fulfillment of the
requirements for the degree of
Doctor of Philosophy in Mechanical Engineering

Abstract

In this thesis work, design and fabrication of micro- and nano-photonic structures both in the diffraction regime and sub-wavelength regime have been investigated.

In the diffraction regime, two types of optical systems and optical elements were investigated for application in LCD manufacturing. With the increasing demand for larger LCD screens at lower cost, technology for low-cost high-throughput manufacturing systems, as well as efficient repair systems within the manufacturing line for any manufacturing defects, are crucial for manufacturers. The first system investigated in this work is a novel optical lithography system for LCD manufacture using a computer generated hologram (CGH). The fabrication challenges for a highly complex pattern inherent in CGHs are addressed. The second system is a defect repair system utilizing a blazed grating matrix (BGM). The BGM generates multiple high intensity spots from a high-power pico-second pulsed laser, controlled by a spatial light modulator, which can ablate the surface of the substrate to eliminate residues and excess material. In both systems, high efficiency and pattern fidelity are required for the optical element, and micro- and nano-fabrication techniques were used in order to achieve the required specifications.

In the sub-wavelength regime, locally periodic dielectric photonic structures with adiabatic variation were designed and verified, with application in lensing in optical frequencies. Structures such as rod lenses and Luneburg lenses are investigated. Especially the latter type of lenses have been conventionally difficult to implement in optical frequencies due to its specific refractive index profile. With the high flexibility of gradient effective index design with the "aperiodic" dielectric nanostructures, along with the design method using Hamiltonian Optics investigated in this research, the Luneburg lens was designed, fabricated, and verified at the wavelength of $\lambda = 1.55\mu m$.

Thesis Supervisor: George Barbastathis
Title: Professor of Mechanical Engineering

Thesis Reader: Gang Chen
Title: Professor, Mechanical Engineering

Thesis Reader: Steven G. Johnson
Title: Professor, Mathematics

Acknowledgments

"*Kō-in Yano Gotoshi*", equivalent of "time flies" in Japanese, literally means light (*i.e.* sun; daytime) and shadow (*i.e.* moon; nighttime) is like a flying arrow.

Indeed, the time I spent at MIT as a graduate student flew past as if at the speed of light. And as is discussed in this thesis, the propagation of light and a flying arrow have much in common. Along this trajectory, I was very fortunate to meet, discuss, and be advised by many great people, without whose help the work presented here could not have been accomplished. I realize that there is no way I can do justice to the people that I am appreciative of, nor a way I can appreciate all of the people that I must, but I hope these acknowledgements will do their best in conveying my sincere appreciation.

First and foremost, I owe tremendous amounts of gratitude to my advisor, Prof. George Barbastathis. His insightful and critical thinking have influence me greatly and his comments have always aided my research path.

Also, I would like to thank my thesis committee members, Professor Gang Chen and Professor Steven G. Johnson. Discussion with them have always been inspiring and set paths for this research from different perspectives. Prof. Chen's insight into nanostructures and Prof. Johnson's deep knowledge and experience vitalized my research every meeting I had with them. I am greatly honored to have such a prestigious Committee for my research.

I also would like to thank my collaborators of the work I have done, particularly Pepe Dominguez-Caballero, James Sungjin Lee, Si Ho Seoung, Chihhao Chang, Se Young Yang, and Johnny Choi. They are great researchers, and I learned tremendously through working and discussing with them.

My labmates in the 3D Optical Systems Lab, both old and new, had always been great to turn to both professionally and for fun. They have made my lab life invaluable and hard to leave from. I have always appreciated their company.

I was very fortunate to meet a lot of great people outside of lab as well, either being roommates or through Japanese organizations. I cannot name all of them here,

but in terms of helping me through great advices for research, I would like to give my gratitude to Eiji Iwase and Haruka Tanji. Some of the results presented here would not have been produced without their valuable input.

The Microsystems Technology Lab (MTL) and the Nanostructures Laboratory (NSL), at MIT, as well as the Center for Nanoscale Systems (CNS) at Harvard were great facilities to work in with great staff maintaining the environment and the machines. Especially Vicky Diadiuk, Kurt Broderick, Jim Daley, and JD Deng were of tremendous help in fabricating devices and conducting experiments.

I would also like to thank my funding sources, Samsung Electronics, centre for environmental sensing and modeling (CENSAM) from the Singapore-MIT alliance, and the Institute of Soldier Nanotechnology (ISN).

Lastly, I cannot end this acknowledgement without mentioning my parents and brothers for supporting me all the way through my career here at MIT. Although living very far, I always felt safe and supported thanks to their warmth.

Contents

List of Figures

List of Tables

Chapter 1

Introduction

Electromagnetic waves behave quite differently depending on the feature sizes of the structure that it impinges on compared to the wavelength of the incident wave. Optical components such as phase gratings and holograms, whose feature sizes are similar but larger than the wavelength, function in the diffractive regime for imaging and spatial/spectral measurement. On the other hand, sub-wavelength structures, such as photonic crystals, possess functions that are not observable in the diffraction regime, bandgaps being one of the most commonly investigated among others. Both regimes provide opportunities for powerful optical functionalities, and proper design and fabrication of the components is critical in order to obtain the optical properties intended by the application.

1.1 Diffractive Optics

Diffraction is one of the most fundamental phenomena in classical optics, along with reflection and refraction. Diffractive optical elements (DOEs) are optical components that utilize this phenomenon for specific optical applications, such as intensity modulation from one optical plane to another. The feature size of DOEs are generally in the order of the wavelength of the radiation, since this size scale is where the effect of diffraction is largest.

Some examples of diffractive optical elements include gratings, which are widely

used in spectroscopy, and holograms, which are used in, besides art pieces, 3D information storage [56] and 3D imaging [18].

1.1.1 Computer Generated Holograms

A hologram is an optical element that can reconstruct wavefronts that have been recorded. The original holograms, one of the first discussed by Gabor [30], require optical recording of the 3D image to be reconstructed. However, holograms can be designed numerically considering the fact that the diffractive light propagation, either in the Fresnel or Fraunhofer regime, can be expressed mathematically with Fourier Transforms. These types of holograms, called computer generated holograms (CGHs), were first proposed by Brown and Lohmann in 1966 [22], and since then have been investigated widely for beam shaping [40], optical trapping [38], optical signal processing [44], optical communications [23], and 3D displays [39].

1.1.2 Fabrication of Diffractive Optical Elements

In order to reconstruct an arbitrary pattern with a hologram precisely, in general, the ability to produce arbitrary phase and intensity at the hologram plane is required. However, this is not practical from the fabrication point of view, when the feature sizes are in the order of microns to sub-microns. Especially, since much of the established fabrication technology in this length scale, such as optical lithography, is two-dimensional, the freedom to tune the phase is limited unless highly complicated and expensive manufacturing technology is introduced, such as ones discussed in [42].

1.2 Sub-wavelength Optics

There has been large research interest in sub-wavelength photonic structures especially in the past two decades. Especially for periodic structures known as photonic crystals, investigations have shown various interesting properties.

1.2.1 Periodic Subwavelength Structures

In 1987, Yablonovich found out that these structures possess bandgaps, equivalent of electric bandgaps in crystal structures [68], and since then, various interesting phenomena and applications have been investigated by numerous researchers, including slow light [20], super collimation [55], negative index [26], form birefringence [29], and so on.

In any of the above applications, the properties of the periodic nanophotonic structure can be expressed by the dispersion diagram. A dispersion diagram plots the frequency of the modes of interest as a function of the wavevector k. Figure 1.2.1 shows a dispersion diagram along the edge of the Brillouin zone for TM modes in a 2D square lattice of a dielectric circle (equivalent of an infinitely long dielectric rod) in air, shown in the inset. The red dotted lines show dispersion curves of air ($n = 1$), also known as the light cone. The bandgap between the first mode and the second mode is evident, as well as the flattening of the mode near point X. Noting that the gradient of the plot of the modes in this diagram, $\partial w/\partial k$ is equal to the phase velocity v_p, flattening of the mode implies slow light, and negative slope a negative index at that frequency. Super collimation and form birefringence can be explained with a 2D dispersion diagram, where the frequency of the modes are plotted both in k_x and in k_y (FIgure 1.2.2). Both utilize the highly nonlinear properties of the dispersion curves especially at high frequency regions, which are due to the periodicity of the structure [27].

1.2.2 Non-periodic Subwavelength Structures

Obviously, interesting sub-wavelength structures are not limited to periodic ones.

One interesting application of non-periodic nanostructures is an optical cloak. The theory of optical cloaks was first given by Pendry [37] and Leonhardt [47], and Valentine fabricated a version of a cloak with nano dielectric structures using focused ion beam for 2D [41], and Ergin for 3D [64]. Note that in either cases, nanostructures are used to obtain a spatial distribution of effective index of refraction through effective

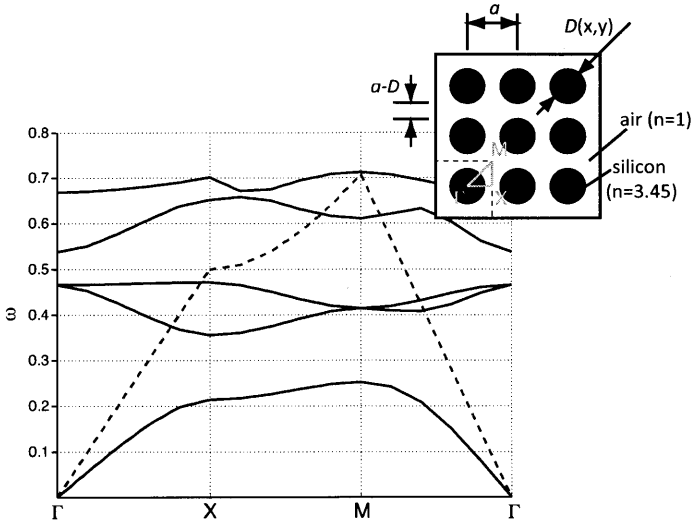

Figure 1.2.1: Dispersion diagram of a square lattice of silicon rods.

medium theory.

1.2.3 Hamiltonian Optics

In this work, Hamiltonian Optics will be used extensively for design and optimization of nanophotonic structures. Although this method originally was used with assumptions for a slowly varying medium, as was shown by Fan [66] and St. J. Russell [59], this method can also be utilized to trace rays in nanostructures with slowly varying periodicity, which actually have high frequency non-smooth variation of actual refractive index.

In Hamiltonian Optics, the ray trajectories through a gradient index medium can be obtained through solving the set of Hamiltonian equations along with a certain initial condition in position in space and momentum (corresponding to the k-vector), which can be expressed as,

$$\frac{dq}{dt} = \frac{\partial H}{\partial p}, \frac{dp}{dt} = -\frac{\partial H}{\partial q}, \tag{1.2.1}$$

where q is the geometrical position in Cartesian coordinates, p is the momentum, and H is the Hamiltonian, which is a conserved quantity along the ray trajectory.

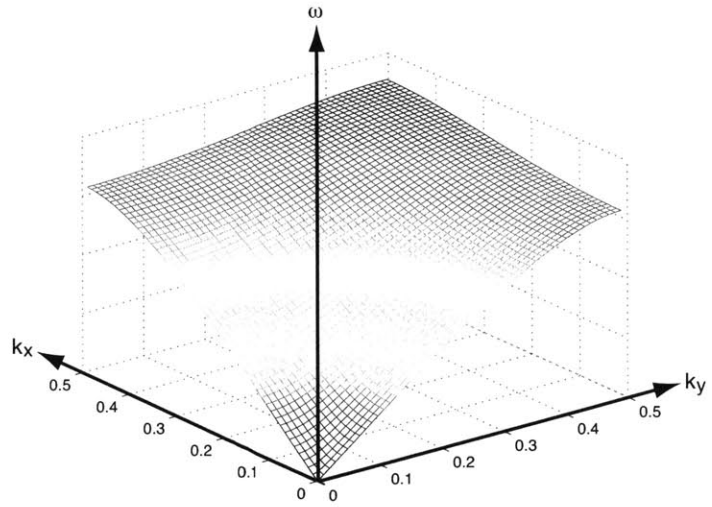

Figure 1.2.2: Dispersion surface of a square lattice of silicon rods.

Foundations of Hamiltonian Optics

Fermat's Principle states that light propagates from one point to another along a minimum path length, mathematically expressed as,

$$L = \int_{p_1}^{p_2} n(\vec{q}) ds, \tag{1.2.2}$$

where L is the optical path length, p_1 and p_2 are beginning and end points, $n(\vec{q})$ is the index of refraction at point in space with Cartesian coordinates $\vec{q}$.
In Cartesian coordinates,

$$\vec{q} = (x(z), y(z), z), \tag{1.2.3}$$

$$ds = \sqrt{(dx)^2 + (dy)^2 + (dz)^2}, \tag{1.2.4}$$

where z is the direction parallel to the optical axis.

Substituting 1.2.3 to 1.2.2,

$$L = \int_{p_1}^{p_2} n(x(z), y(z), z)\sqrt{(dx)^2 + (dy)^2 + (dz)^2} \tag{1.2.5}$$

$$= \int_{z_1}^{z_2} n(x(z), y(z), z)\sqrt{\left(\frac{dx}{dz}\right)^2 + \left(\frac{dy}{dz}\right)^2 + 1}dz \tag{1.2.6}$$

$$= \int_{z_1}^{z_2} n(q_x(z), q_y(z), z)\sqrt{\dot{q}_x^2 + \dot{q}_y^2 + 1}dz. \tag{1.2.7}$$

Now, we define the Lagrangian as:

$$\mathscr{L} = n(q, \dot{q}, z)\sqrt{|\dot{q}|^2 + 1}. \tag{1.2.8}$$

The Fermat's Principle can be described as:

$$L = \int_{z_1}^{z_2} \mathscr{L}(q, \dot{q}, z)dz = min., \tag{1.2.9}$$

and from

$$\mathscr{L}(q + \epsilon h, \dot{q} + \epsilon\dot{h}, z) = \mathscr{L} + \epsilon\left(\frac{\partial\mathscr{L}}{\partial q}h + \frac{\partial\mathscr{L}}{\partial\dot{q}}\dot{h}\right), \tag{1.2.10}$$

The variation in the optical path is,

$$L(\epsilon h) = \int_{z_1}^{z_2} [\mathscr{L}(q, \dot{q}, z) + \epsilon\left(\frac{\partial\mathscr{L}}{\partial q}h + \frac{\partial\mathscr{L}}{\partial\dot{q}}\dot{h}\right)]dz = min. \tag{1.2.11}$$

$$\delta L(\epsilon h) = \epsilon\int_{z_1}^{z_2}\left(\frac{\partial\mathscr{L}}{\partial q}h + \frac{\partial\mathscr{L}}{\partial\dot{q}}\dot{h}\right)dz \tag{1.2.12}$$

$$= \epsilon\int_{z_1}^{z_2}(\frac{\partial\mathscr{L}}{\partial q} - \frac{d}{dz}\frac{\partial\mathscr{L}}{\partial\dot{q}})hdz. \tag{1.2.13}$$

Therefore, in order for the path length L to have minimum path length,

$$\frac{\partial\mathscr{L}}{\partial q} - \frac{d}{dz}\frac{\partial\mathscr{L}}{\partial\dot{q}} = 0. \tag{1.2.14}$$

i.e.,

$$\frac{\partial n}{\partial q}\sqrt{|\dot{q}|^2+1}-\frac{d}{dz}\frac{n\dot{q}}{\sqrt{|\dot{q}|^2+1}}=0. \tag{1.2.15}$$

Now, the momentum and Hamiltonian are defined as,

$$p=\frac{\partial \mathscr{L}}{\partial x}=\frac{n\dot{q}}{\sqrt{|\dot{q}|^2+1}}, \tag{1.2.16}$$

$$H=p\dot{q}-\mathscr{L}. \tag{1.2.17}$$

Therefore we obtain the Hamiltonian equations as,

$$\dot{q} = \frac{\partial H}{\partial p}, \tag{1.2.18}$$

$$\dot{p} = -\frac{\partial H}{\partial q}. \tag{1.2.19}$$

1.2.4 Fabrication of Sub-wavelength Structures

With emergence and maturity of micro- and nano-fabrication technology, photonic crystal and other nano-photonic structures have been successfully fabricated to function in optical frequencies, either in 2D [50] or 3D [49].

Photonic crystals without defects can take advantage of their periodicity, either in 2D or 3D, and be fabricated with interference lithography [49] or self-assembly [67]. These techniques allows relatively fast fabrication of large-area structures. However, once defects are introduced to periodic structures, or if the structure is non-periodic, other fabrication techniques that are usually more time consuming, such as electron-beam (e-beam) lithography, must be incorporated. For 3D non-periodic structures, there are several different types of fabrication methods. One is the use of either two-photon ablation or polymerization in a 3D material [45, 34], another set of technology involves the use of a well established 2D lithography technique and stacking of multiple layers in order to build up the third dimension [51, 43, 54]

1.3 Thesis Objective and Contributions

This thesis work presents design and fabrication methods for optical components whose feature sizes are close to or smaller than the wavelength of light of interest. Especially for visible frequencies, these components possess feature sizes in the order of tens of microns to hundreds of nanometers. Both diffractive and sub-wavelength regimes will be investigated, and experimental verification is conducted to prove the capabilities of the design and fabrication techniques presented.

In the diffractive regime, two novel optical systems are designed, fabricated, and tested. One is a non-contact high-resolution LCD manufacturing system using a CGH, and the other is a multi-spot ablation system for LCD pixel repair using a blazed grating matrix. The former system resolves the problem with conventional lithography techniques, being very expensive in order to meet high-throughput and high-resoluction requirements at the same time. The latter system can be used to repair defects in LCD displays with high speed and low cost by parallel ablation of defects using multiple spots. The diffractive optical elements for both systems were fabricated using micro-fabrication technologies and tested in an optical setup.

In the subwavelength regime, an optical device was designed and fabricated for highly flexible lensing application in optical frequencies. Their design method using Hamiltonian Optics was established, along with fabrication of a proof-of-concept device and its verification. Although there have been reports on non-periodic nanostructures, not much research has been conducted to incorporate the extensive theory of photonic crystals and dispersion relations into non-periodic structures and use them as tools to design nanostructures for effective index control in optical devices such as lenses with functions that were not possible with conventional manufacturing techniques.

1.3.1 Outline of Thesis

In Chapter 1, overview of concepts and previous work regarding diffractive and sub-wavelength optics were discussed. The concept of diffraction and diffractive optical

elements have been introduced, and previous literature on analysis, design, and fabrication of DOEs, especially CGHs, have been discussed. Also, interaction of light with sub-wavelength structures have been discussed, both for periodic and non-periodic structures. Hamiltonian Optics was introduced as a ray-tracing technique as well as fabrication technologies for these structures.

The remainder of this thesis is structured as follows:

Chapter 2 will discuss two optical systems using DOEs, namely, an optical lithography system using a CGH, and a multi-spot laser ablation system with a blazed grating matrix. For both systems, the system concept and overall design will be discussed, as well as the specific components, especially the design and fabrication of the DOEs. The experimental results of the system will be discussed and analyzed.

In Chapter 3, sub-wavelength aperiodic structures will be discussed. The design method for these structures based on Hamiltonian Optics will be discussed in detail, and two example structures will be designed, namely, a rod lens and a Luneburg Lens. Simulation results of the designed structures using Hamiltonian Optics will be discussed, and will be compared with the finite difference in time domain (FDTD) method. Further, fabrication and experimental results of the Luneburg Lens structure will be presented.

The conclusions and suggestions for future work will be delivered in Chapter 5.

Chapter 2

Diffractive Optics for LCD manufacture and repair

Liquid crystal displays (LCDs) are omnipresent in our daily lives, from cell phone screens to advertisement displays. Due to high competition, it is critical to fabricate them at as low cost as possible to sell at a competitive price and gain revenue at the same time. Especially as the demand for larger LCD displays grow, it becomes more critical to use a manufacturing method that is fail-proof and fail-safe. The former can be achieved with a high-precision fabrication method, and the latter with an efficient repair system.

In this Chapter, two types of optical systems are introduced, one for LCD manufacturing and the other for repair within the manufacturing line of the displays. In either cases, high precision and high throughput are required, while keeping the overall cost of the system and process low. The optical systems are designed using analytical and numerical methods, an experimental setup is built and tested, and the diffractive optical device was fabricated using microfabrication techniques.

2.1 LCD Lithography Using CGH

Lithography has become a crucial technology to fabricate structures with micron to sub-micron features. Among the wide variation of lithography techniques, optical

lithography, especially steppers which have high efficiency and can obtain high resolution, have become the industry standard. While optical lithography is a very efficient fabrication method, since light propagation suffers diffraction in general, in order to replicate a high fidelity mask pattern close to the diffraction limit, either the substrate must be in close contact with the mask, or highly expensive and large optics must be used to image the mask pattern on to the substrate with minimum aberration.

In this section, a lithography system for LCD manufacturing using a computer generated hologram (CGH) will be introduced. The advantage of this system is that it is non-contact, hence high-throughput while allowing for diffraction-limited pattern generation on the mask without using expensive and massive optics.

CGH lithography has been proposed and investigated in the past. However, they suffer either problems with low efficiency and fidelity or fabrication complexity [42, 28]. The former can be alleviated with design and optimization methods for the CGH pattern, but the latter requires consideration in the fabrication technique of the CGH, which usually has highly complicated features at length scales of hundreds of nanometers.

Here, we use a phase-only CGH. This is due to the efficiency requirement of the system, where an amplitude CGH would decrease the amount of light propagating through. While the high efficiency is a great advantage, the phase CGH adds a complication to the fabrication, which is that the height and uniformity of the relief structures on the CGH becomes critical. This problem will be addressed as discussed later in this Chapter.

2.1.1 Design of the Optical System

The overall system is very simple, where the collimated and expanded beam from the laser directly illuminates the CGH, which diffracts light onto the substrate separated by approximately 100 μm. This simplicity is very important since the more complex the system, the more likely any errors, such as aberration from the optics, will arise and will be enhanced.

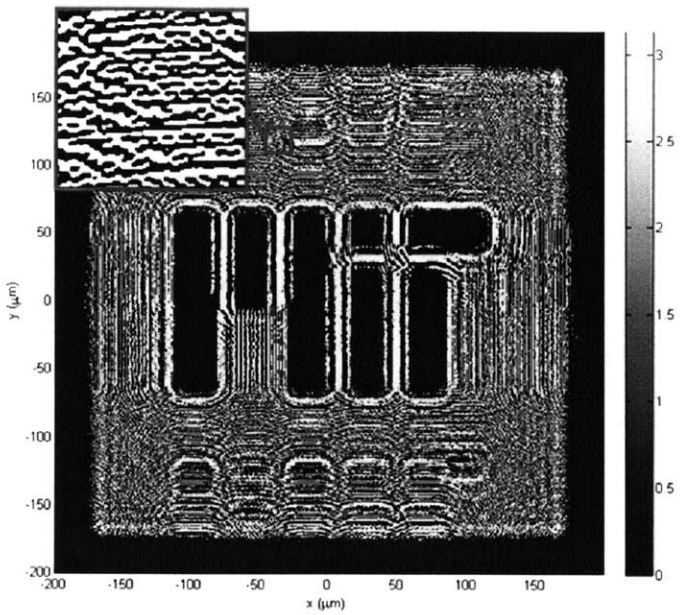

Figure 2.1.1: Optimized binary phase in-line CGH that reconstructs the MIT logo.

In [25], Dominguez-Caballero successfully investigated a method to optimize Fresnel domain CGHs, which are suitable for lithography applications, using modified error reduction and genetic algorithms. He also incorporated the use of local diffusers to generate more efficient CGHs. In this Section, fabrication of the CGHs designed by his optimization schemes will be discussed.

2.1.2 Fabrication of the CGH

In this section we describe the fabrication process and associated technologies for the manufacture of in-line binary phase CGH using e-beam lithography. The two CGH designs fabircated are those of Figure 2.1.1, Figure 2.1.2, and Figure 2.1.7. The overall fabrication process is shown in Figure 2.1.3.

The first step in the fabrication process is to spin a layer of Hydrogen Silsesquioxane (HSQ, Dow Corning FOx-series [8]) onto a fused silica substrate. The thickness of the HSQ is equivalent to the required optical phase difference given by:

$$t = \frac{\phi\lambda}{2\pi\left(n_2 - n_1\right)}, \tag{2.1.1}$$

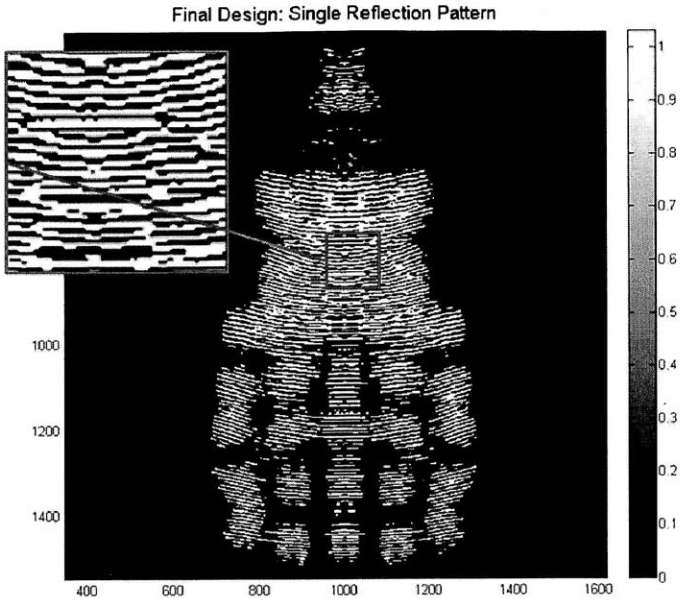

Figure 2.1.2: Optimized binary phase in-line CGH that reconstructs a grating matrix.

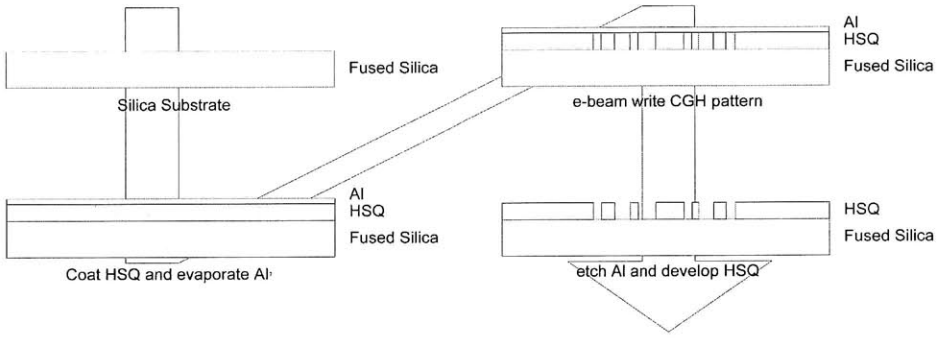

Figure 2.1.3: Fabrication method for the CGH using HSQ and e-beam lithography.

where ϕ is the required phase range (R of Equation 2), λ is the operating wavelength in free space, n_2 is the HSQ's refractive index at the operating wavelength and n_1 is the refractive index of the surrounding medium, which in this case is air ($n_1 = 1$). The spin speed is determined from the spin (spin speed-thickness) curve of the HSQ with the particular dilution. After spinning, the HSQ is baked at 150 degrees for 2 minutes, then at 220 degrees for another 2 minutes using hotplates. Next, a thin (5-6nm) metal layer is deposited on the HSQ by e-beam evaporation. This metal layer is required in order to avoid charging during the e-beam exposure as all the layers underneath are non-conductive. Any type of conductive material that does

not react with HSQ and can be easily deposited and removed without significantly damaging the underneath layers is appropriate for this layer. In our process, we used either aluminum or chromium. After this step, the CGH patterns were written with a Raith150 e-beam exposure system. The time for the e-beam write varies according to the holograms size, pixel size and dose, taking approximately 30 minutes to 1.5 hours to write the patterns described in this section. Finally, the metal layer is removed by wet chemical etching, and the HSQ is developed either for 2 hours with Shipley Microposit MF CD26, a TMAH-based developer, or for 2 minutes with an aqueous mixture of NaOH alkali and NaCl salt [69].

HSQ is a negative resist sensitive to e-beam radiation and X-ray. It is also known as spin-on dielectric, and can be spun on similarly to photoresists, but acquires mechanical and optical properties similar to glass upon exposure to e-beam. Therefore, HSQ is a very useful material for CGH fabrication, since it can provide the diffraction layer, eliminating the necessity to etch through the fused silica substrate, and making the overall process simple. HSQ is known to be capable of patterning in high resolution, some reports claiming gratings patterned in HSQ with 10nm line thickness [36]. The thickness of the HSQ layer can be controlled down to an error of around 1%, which does not add significant noise to the reconstructed results, as shown in the sensitivity analysis section [32].

In general, e-beam writing is known to suffer from proximity effects that distort the resulting pattern in the resist. In order to minimize this effect, the dose of the beam must be properly chosen according to the beam energy, pattern, and the stack of layers that the e-beam writes on. Due to the complex structure of the CGH mask, the exposure dose of the e-beam write must be determined for each mask through dose experiments. Further, different dose must be used for each section of the mask in order to reproduce the mask pattern faithfully onto the HSQ. An alternative method for correcting the proximity errors is by the implementation proximity error correction (PEC) software [52]. However, these software usually require either material parameters, which can be difficult to characterize, or the point spread function of the electron beam through the stack of materials on the substrate, which requires

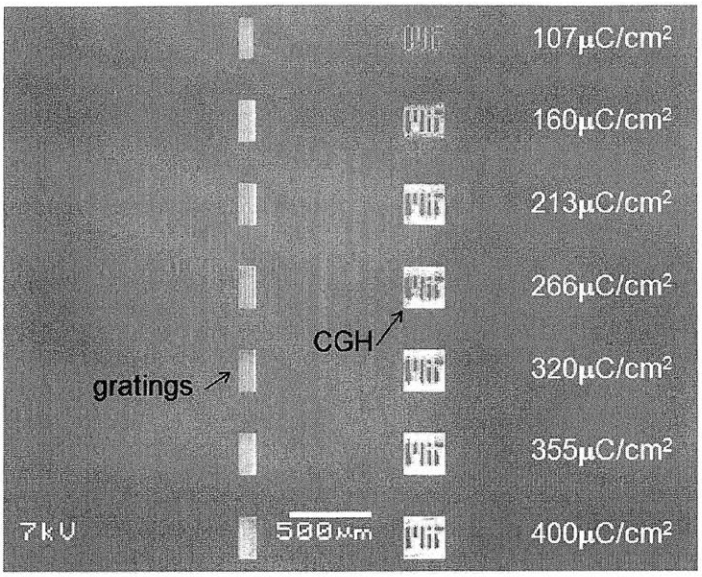

Figure 2.1.4: Dose Matrix to determine the proper dose for the CGH.

extensive experimental investigation.

A scanning electron microscope (SEM) image of an example of a dose experiment for the in-line CGH manufactured on a silicon substrate is shown in Figure 2.1.4. Chirped gratings were written at each dose as well as the CGH mask in order to evaluate the writing characteristics (line edge roughness, minimum resolution, etc.) decoupled from the complex CGH structure. From this experiment, we can see that for the smaller doses, the hologram is underexposed and the HSQ is overly removed by the developer. Also, several other patterns are overexposed and a substantial amount of HSQ is left over after development where they should be cleared out due to proximity effects as explained later. The best hologram in this case has a dose of $320\mu C/cm^2$ (Figure 2.1.5). Figure 2.1.6 shows a comparison between the over and under dosed cases for the in-line CGH fabricated on a silicon substrate.

Figure 2.1.8 shows an SEM image of the fabricated in-line CGH for the design shown in Figure 2.1.7. Note that the periodicity of the fringes have become more uniform across the structure. This is due to the redistribution of the energy on the CGH, done through a virtual diffuser [25]. Figure 2.1.9 shows more close-up SEM images of the fabricated CGH. Highly complicated features are reproduced clearly

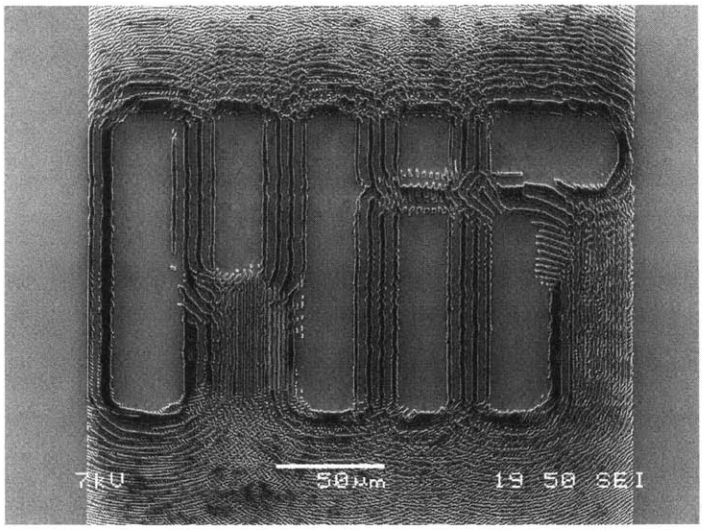

Figure 2.1.5: SEM image of the fabricated CGH with design shown in Figure 2.1.1

down to smaller than 200nm.

Figure2.1.10 shows a comparison of a section of this hologram with the original CGH pattern. Most of the patterns on the mask, including many of the finer details, are transferred with high accuracy onto the HSQ. However, additional optimization steps, such as dose matrices with smaller dose steps, are required in order to get the exact pattern reproduced. In addition, the results from the sensitivity analysis explained in a later section can be used to redesign the CGH mask to compensate for different manufacture errors.

The second fabricated design was that of Figure 2.1.2 that reconstructs a grating matrix at the photoresist plane 50μm away. Figure 2.1.11 shows an SEM image of a fabricated CGH for the reflection pattern. This CGH was fabricated with the Raith 150 system at 10keV, and the dose was varied across the structure to compensate for the proximity effect.

The dose at each section of the pattern was determined through a dose matrix, in which small sections were compared to the original design and the best-fitting dose was determined for each section. Figure 2.1.12 shows a comparison of the fabricated pattern with different doses at two different locations within the mask. It can be seen that different dose are required for different features on the CGH.

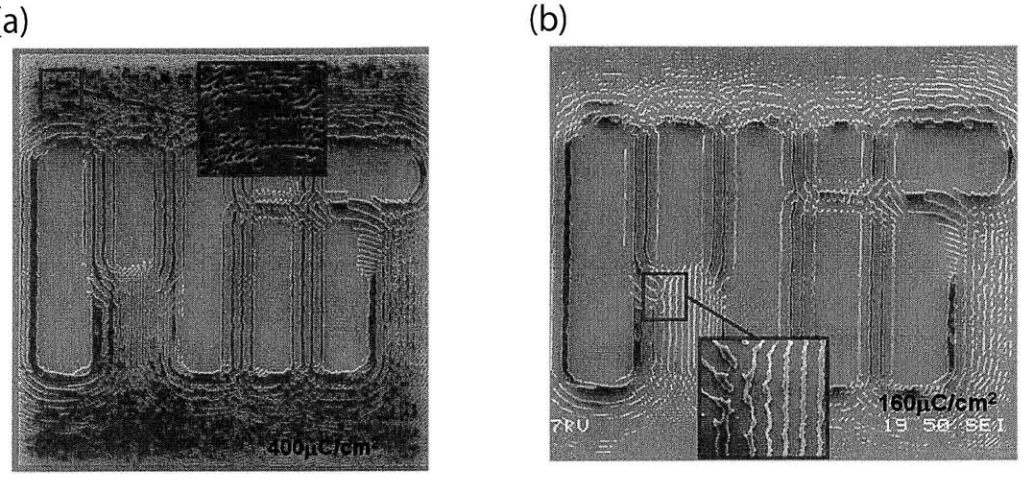

Figure 2.1.6: Comparison of fabricated CGHs with (a) over- and (b) under-exposure.

Evaluation of Fabrication Accuracy

The fabricated CGH patterns contain geometrical distortion due to fabrication errors such as non-ideal dose of the e-beam, proximity effects, stitching errors, positioning of the beam and the stage in the e-beam writing system, etc. In order to quantitatively evaluate these errors, first, a 2D error map was computed using a spectral based cross-correlation algorithm using data from a confocal microscope. Second, a global mean square error (MSE) was computed and used as a point of comparison between different fabricated samples. Finally, the expected reconstructed intensity at the photoresist from the actual fabricated sample (sample with fabrication errors) is simulated.

Figure 2.1.16 shows the block diagram of the evaluation algorithm. The first step in this algorithm consists of capturing confocal microscope images of the fabricated samples such as those shown in Figure 2.1.14. These images require high magnification and due to the limited field-of-view of the confocal microscope, multiple images from a single CGH must be taken.

The second step consists of noise reduction with a binarization processes. Then the subimages are stitched together with the result shown in Figure 2.1.15 for an example of a fabricated sample. In order to compare the resultant binary image of the fabricated sample with the original design, the image needs to undergo a rotation, scale and lateral shift correction processes. These processes are computed using the

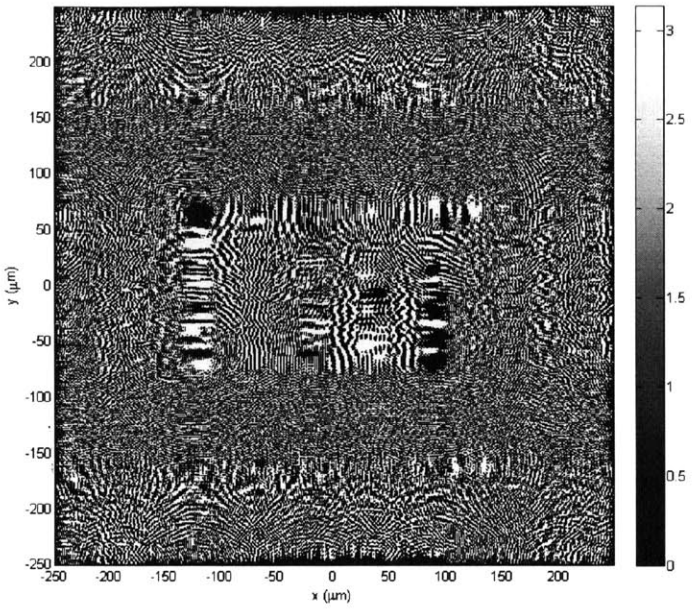

Figure 2.1.7: Design of in-line CGH optimized using the simulated optical diffuser initial guess.

spectral cross-correlation algorithm shown in Figure 2.1.16. An example of a cross-correlation map is shown in Figure 2.1.17. After computing the cross-correlation map, the peak magnitude and position are extracted and are used to estimate the adequate lateral shift, scale and rotation parameters.

The last step consist of the computation of a 2D error map (Figure 2.1.18) and a global error metric based on the MSE of the difference between the fabricated and the designed CGH patterns. The 2D error map is very useful to understand what sections of the fabricated pattern require more or less proximity effect compensation (dose correction). Alternatively, the original pattern could get modified, for example by thinning the fringes, so that after fabrication the sample is compensated for proximity effects.

Spectral cross-correlation is computationally efficient compared to spatial cross-correlation. This method can be automated in order to evaluate the fabricated sample. The error was calculated to be approximately 10%.

As a final evaluation step the expected intensity distribution of the fabricated sample is computed. Figure 2.1.19 shows a comparison of the desired intensity from

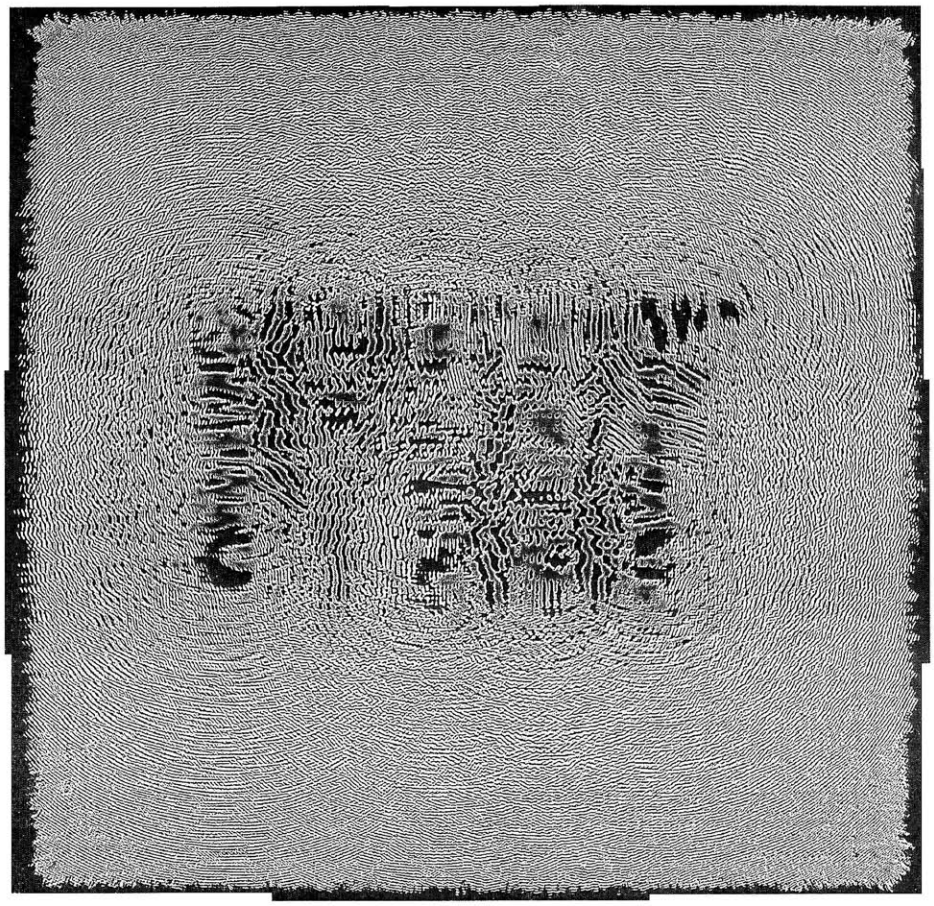

Figure 2.1.8: SEM image of the fabricated CGH with design shown in Figure 2.1.7

the original design and the expected intensity from the fabricated CGH of sample 7. A comparison between the original CGH pattern and sample 7 is shown in Figure 2.1.20. It is clear from this figures that the 10% residual error of this sample reduces the holograms diffraction efficiency allowing undesirable diffraction orders to distort the reconstructed pattern.

2.1.3 Optical Characterization

An optical setup was design to perform the optical characterization of the fabricated CGH. The optical setup is shown in Figure 2.1.21. A green laser (532nm) is spatially filtered and collimated to produce a plane wave that probes the fabricated in-line hologram with an incidence angle normal to the surface of the hologram. The diffracted

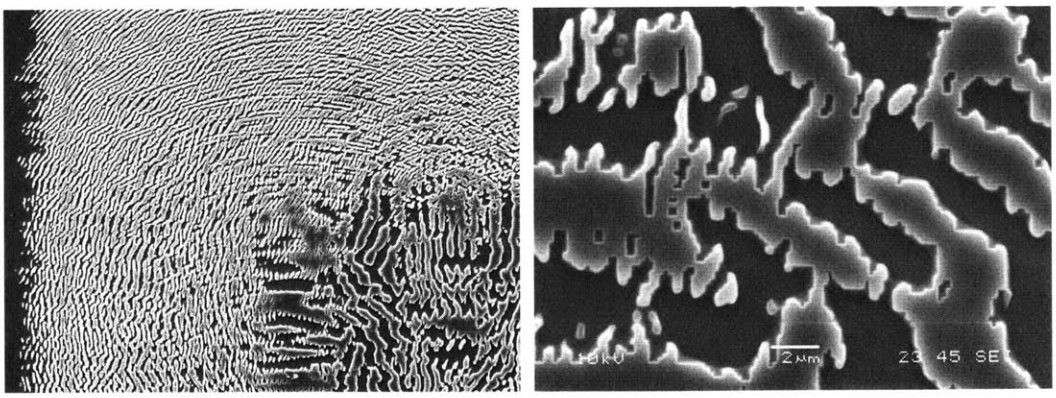

Figure 2.1.9: SEM image of the fabricated CGH with design shown in Figure 2.1.7

field is imaged by a 100× (NA = 0.75) microscope objective onto a 16 megapixel CCD with pixels of 9μm×9μm. The microscope objective and CCD are placed on top of a motorized linear stage with an axial resolution of 1μm that allows axial scanning.

Figure 2.1.22 shows the reconstructed intensity distribution from the fabricated hologram of the design of Figure 2.1.7. The reconstructed pattern shows good contrast and well defined edges of the letters which indicates that many of the high spatial frequency fringes survived the fabrication process. Any errors in the fabrication cause lower diffraction efficiency than that of the original design giving rise to more visible background noise.

2.1.4 Exposure Test

In terms of the reflection grating patterns, we have conducted a printing experiment onto a photoresist in order to characterize the actual exposure characteristics of the CGH. A 364nm laser was used for the exposure in an in-line configuration, for which the CGH has been designed. Figure 2.1.23 shows the exposure results obtained from this experiment, compared with the predicted intensity distribution at the photoresist for the fabricated sample of Figure 2.1.20. Many of the grating patterns have clearly been reproduced, while some sections are washed out, which resemble the simulated exposure result as expected.

The discrepancy between the experimental result and the simulated result can

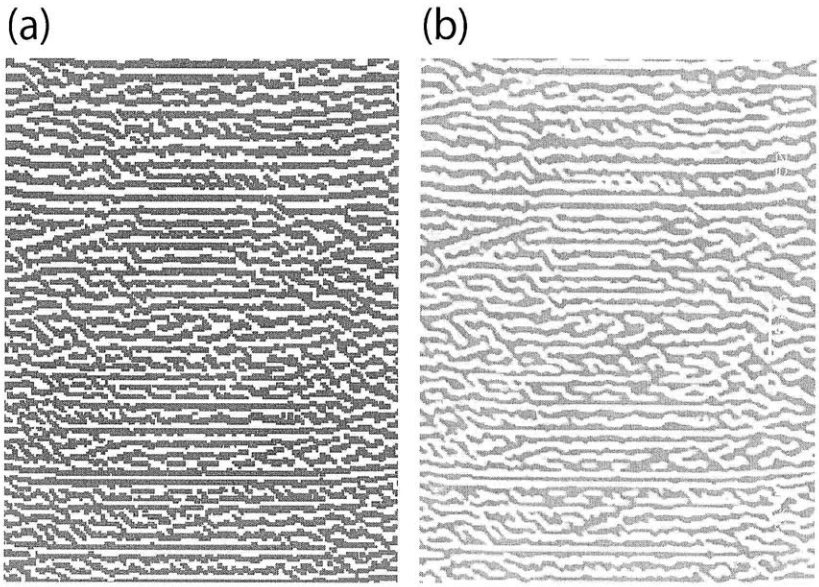

Figure 2.1.10: Comparison of fabricated CGHs with design for the same section.

be regarded to be due to experimental errors. First, the exact dose required for the photoresist was unknown, and further experiments and data are needed to obtain the exact dose required to generate the ideal grating pattern. Second, the experimental setup for the exposure was not ideal for the required working distance of $50\mu m$ and a depth of focus (DOF) of $\pm 0.3\mu$m, and practical difficulty aroused in adjusting the working distance within the DOF. This problem can be alleviated by designing the working distance and the DOF of the CGH to be much larger. Third, the developing conditions for the photoresist also needed further experiments and optimization. Lastly, the drying process after the development can also play a critical role in producing the gratings.

2.1.5 Conclusion

The feasibility of computer generated holographic technology for high-resolution and high-throughput lithographic applications was investigated. The design flexibility, reconstruction quality, simplicity of system and life span makes CGH technology a promising technology. Experimental fabrication process and systematic evaluation of fabricated samples was performed. A sensitivity analysis to understand the implica-

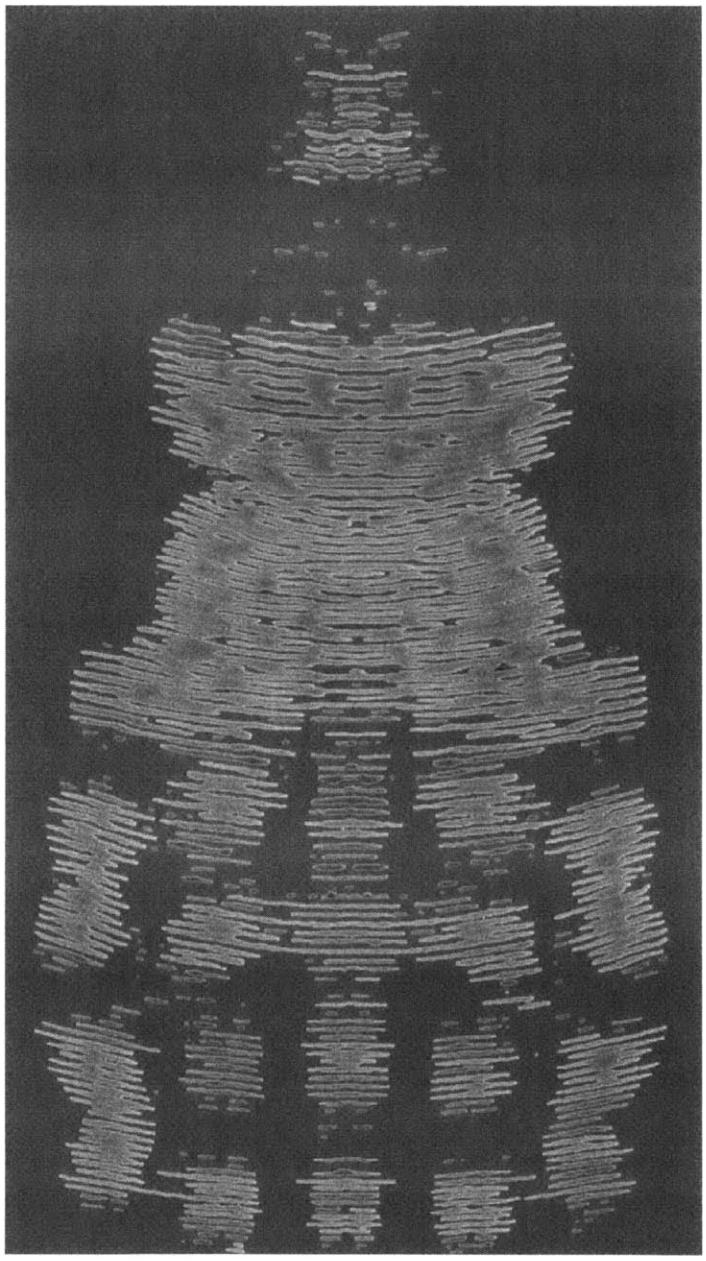

Figure 2.1.11: SEM image of fabricated CGH for grating matrix.

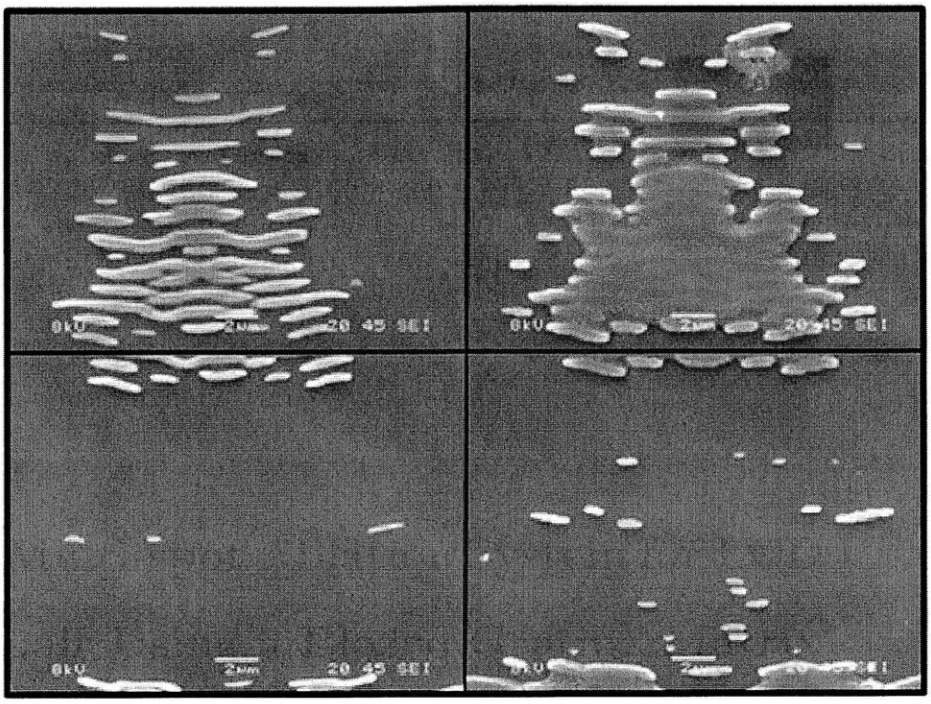

Figure 2.1.12: Comparison of various dose conditions at various sections of the pattern. Note that while $1.25\mu C/cm^2$ (left side) is a better dose for the features in the top row, the features in the bottom row require a dose of $80\mu C/cm^2$ (right side).

tions of potential manufacture errors was implemented.

2.2 Multi-spot Ablation System for LCD Pixel Repair Using a Blazed Grating Matrix

As the demand for larger liquid crystal displays (LCDs) and lower prices grow quickly, the ability to repair any manufacturing defects within the manufacturing process line becomes crucial. Further, being able to do this efficiently is an advantage to the manufacturer.

In this Section, a system for multi-spot ablation will be introduced. Two main types of defects were considered: open defects (open circuits) and closed defects (left over residue, redundant circuits). For the open defect type, the missing patterns are deposited by means of a laser chemical vapor deposition (LCVD) process. For the

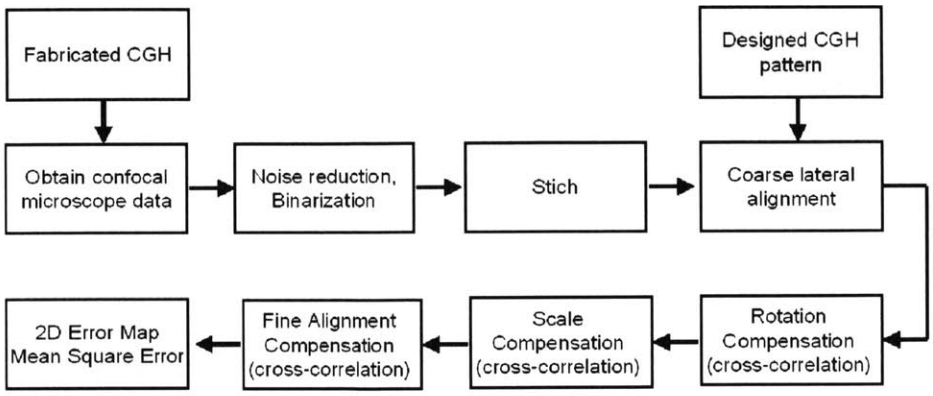

Figure 2.1.13: Block diagram of CGH evaluation algorithm.

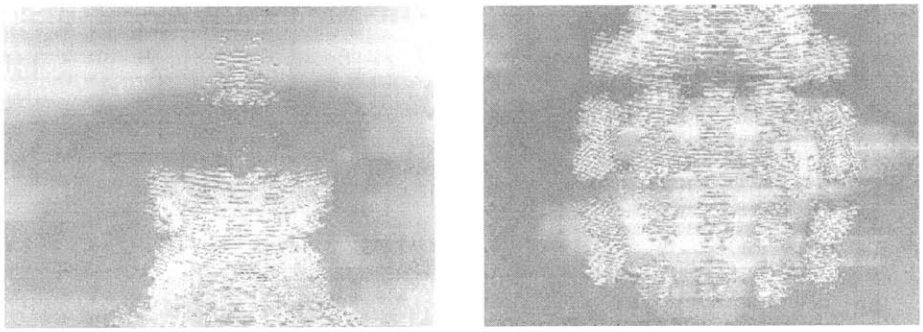

Figure 2.1.14: Example confocal microscope data of the reflection grating CGH.

closed defect type, the residual material is eliminated by means of an ablation process. The proposed system will be designed to perform the following three tasks: 1. Metal deposition for the correction of open defects, 2. Laser ablation for the correction of closed defects, 3. Monitoring/imaging for the inspection of the pixel before/after correction.

The system will form high-energy spots in the form of a matrix on the substrate with 30 μm separation between each other. Some of the main challenges of the system include design of the optical system using cost effective methods and meeting the resolution criteria while maintaining the large operation area, as well as fabrication of the required components of the system.

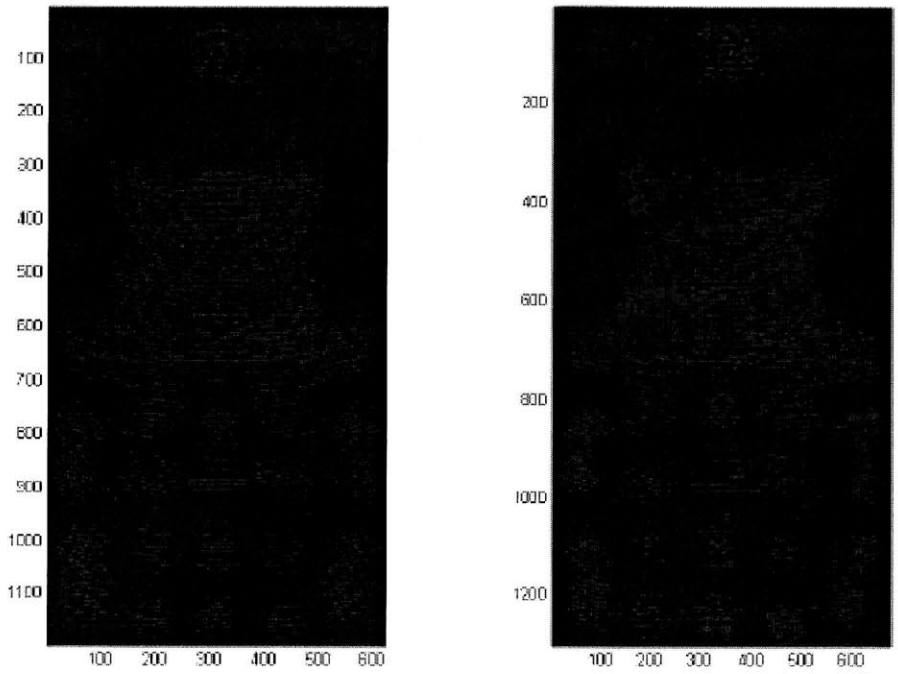

Figure 2.1.15: Example of binarized and stitched data: (left) desired CGH; (right) actual fabricated CGH.

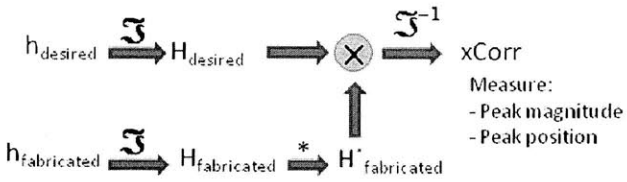

Figure 2.1.16: Spectral cross-correlation method.

2.2.1 Design of the Optical System

Figure 2.2.1 shows a schematic of the entire system. In this section, we will go over the functionality and characteristics of each component, as well as choice of parameters or devices.

Objective Lens

The objective lens was chosen to meet the requirements to have high numerical aperture, a working distance of over 10mm, and also a small effective focal length. We

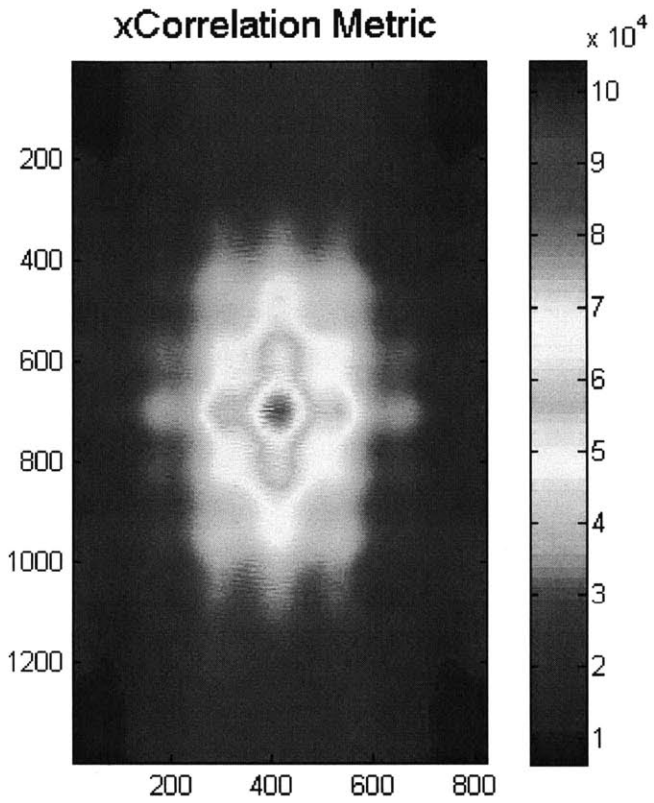

Figure 2.1.17: Example of cross-correlation map.

Table 2.2.1: Specifications of Mitutoyo M Plan Apo NUV 100x [11]

Working Distance	**Numerical Aperture**	**Focal Length**	**Resolution**	**Depth of Focus**
11.0mm	0.50	2mm	$0.6\mu m$	$1.1\mu m$

have found the Mitutoyo M Plan Apo NUV 100× lens [11] to be the optimum choice for our application. Specifications of this objective lens are shown in Table 2.2.1.

Relay Optics

Relay optics between the objective lens and the grating matrix is important in order to provide more flexibility in the design of the system, considering the fabrication limitations of the grating matrix. In addition, the diffraction artifacts resulting from the elemental grating cell finite size are minimized. The selection and optimization

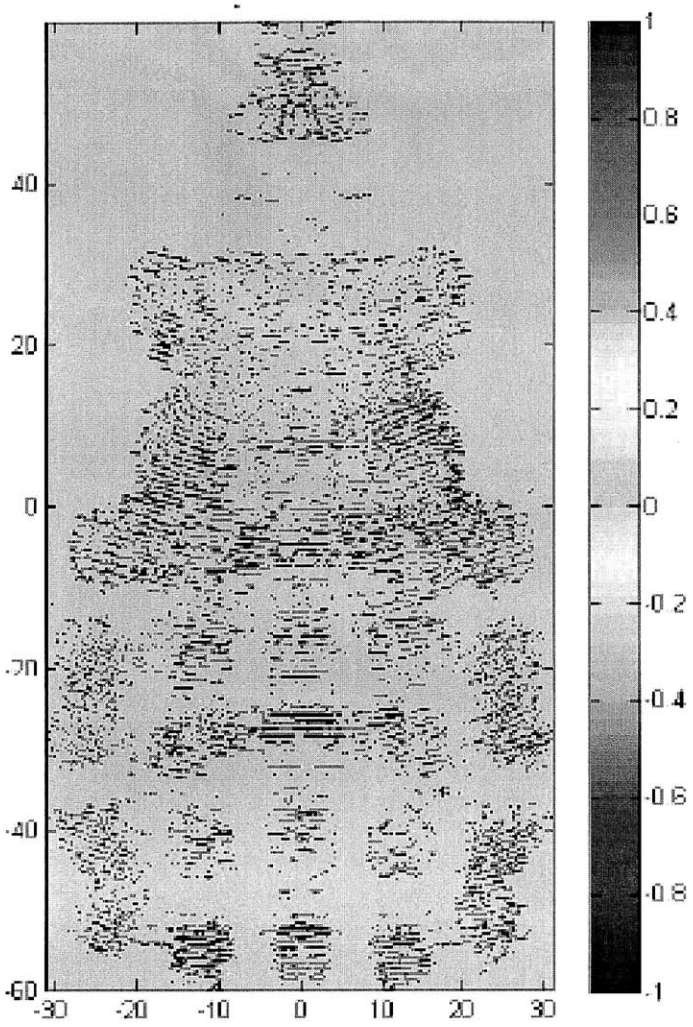

Figure 2.1.18: Error Map of the best fabricated reflection grating.

of the optics used is discussed in the next Section.

Grating Matrix

The grating matrix consists of an array of gratings with different pitch and orientation. The purpose of this component is to steer the beam so that the spot at the image plane is precisely at the required location. As was seen in the previous section, the size of the gratings, as well as their design, play an important role in the design of the system. We designed both binary and blazed gratings to obtain high efficiency in the required diffraction order, and the former was fabricated with conventional optical

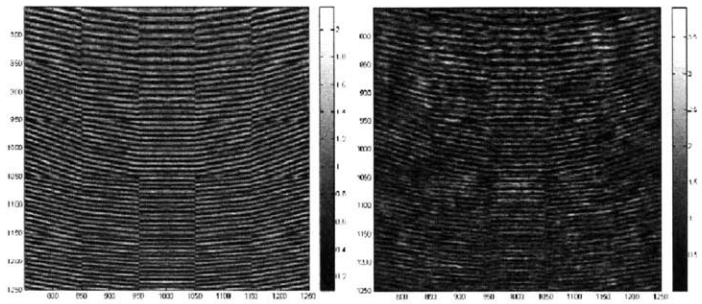

Figure 2.1.19: The designed reconstructed intensity (left) and the numerically reconstructed intensity of the fabricated CGH.

lithography, and the latter was designed to be fabricated with gray scale lithography. Details of the design and fabrication methods will be discussed in a later section.

Spatial Light Modulator (SLM)

A spatial light modulator (SLM) is used in our system to control the on/off of each ablation spot, as well as to compensate for the variation in efficiency of the multiple gratings with different pitches. In general, there are two types of SLMs, micro-actuated mirrors such as Boston Micromachines deformable mirrors [6] and Texas Instruments digital micromirror devices (DMDs) [7], and liquid crystal (LC)-based modulators such as ferroelectric liquid crystals (FLCs) and twisted nematic liquid crystals (TNLCs).

In the case of the discussed system, the LC modulators are more suitable for the following reason. In this system, all beams must have equal power at the exposed substrate in order to have proper ablation characteristics. However, due to variation in diffraction efficiencies from the gratings, the intensity of each beam must be tuned individually. This tuning can be done by an LC light modulator, since the device has capabilities of tuning the attenuation of the beam passing through. Note that even though digital mirrors can also attenuate light, this is through high-frequency vibration of the mirrors, which is not applicable to pico-second pulsed lasers.

In our setup, we installed the LCoS system from Holoeye [9] due to its availability as an integrated device. Figure 2.2.2 shows the installation of the device in the setup.

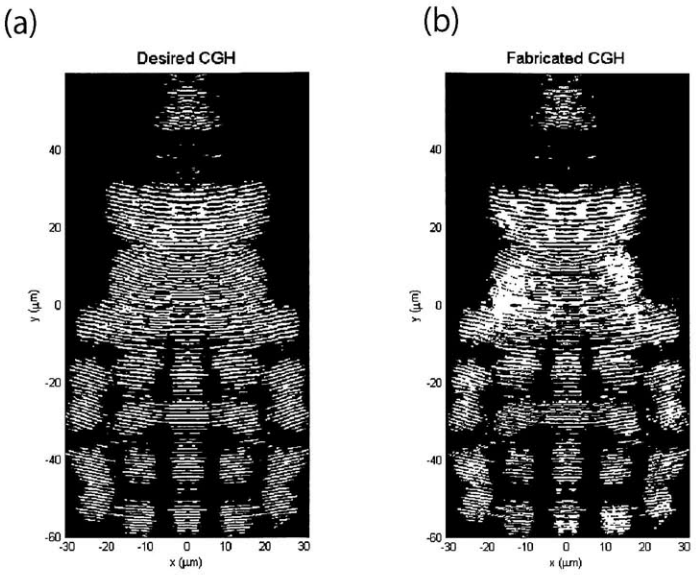

Figure 2.1.20: Comparison of designed and fabricated CGH patterns. (a) desired CGH pattern; (b) fabricated CGH pattern

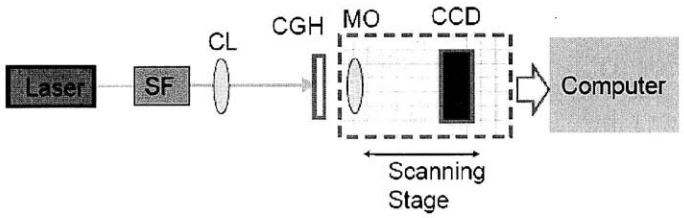

Figure 2.1.21: Schematic of optical characterization setup.

The SLM is installed at about 45 degrees from the beam path. The exact angle was calculated to be 44.8314 degrees from the aspect ratio of a square generated by the SLM, imaged between the SLM and the CCD. The magnification of the 4f system was also calculated from this method to be 1.97625. Note that the pixel size of SLM is $20\mu m$ and that of the UV camera by Sony, which was used to inspect the image at the substrate plane, is $4.65\mu m$. Matlab was used to create the required pattern on the SLM.

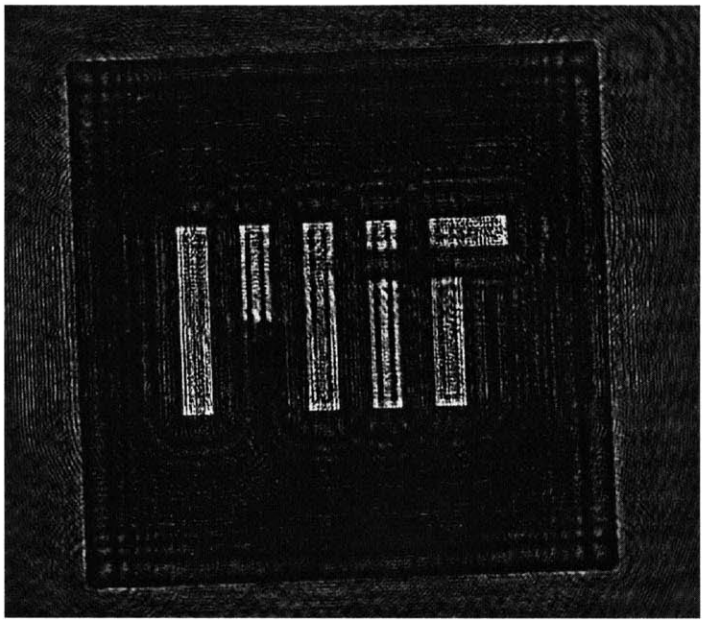

Figure 2.1.22: Reconstructed intensity distribution by fabricated in-line CGH

Laser

For the laser, we use a diode pumped pico second laser [4] with specifications indicated in Table 2.2.2. As can be seen from the table, the laser has a specified average power of 3W at 10kHz and pulse energy of 1mJ/pulse at 1kHz. Given that the total energy density that is required at the substrate for ablation is $5\text{J}/cm^2$ [16], and that the target spot size is $2\mu m$ in diameter, the total energy required for ablation at 1000

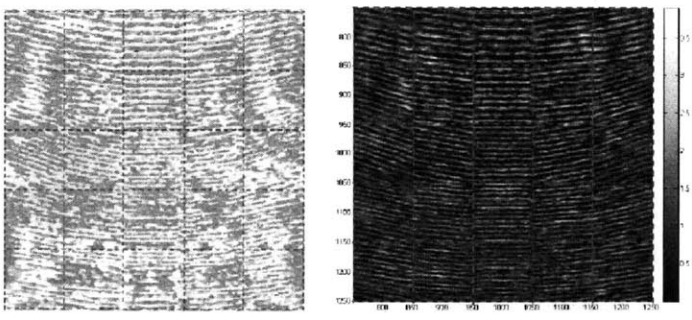

Figure 2.1.23: Confocal microscope image of experimentally printed pattern on photoresist (left) and numerically reconstructed intensity of the reflection grating CGH used in the experiment.

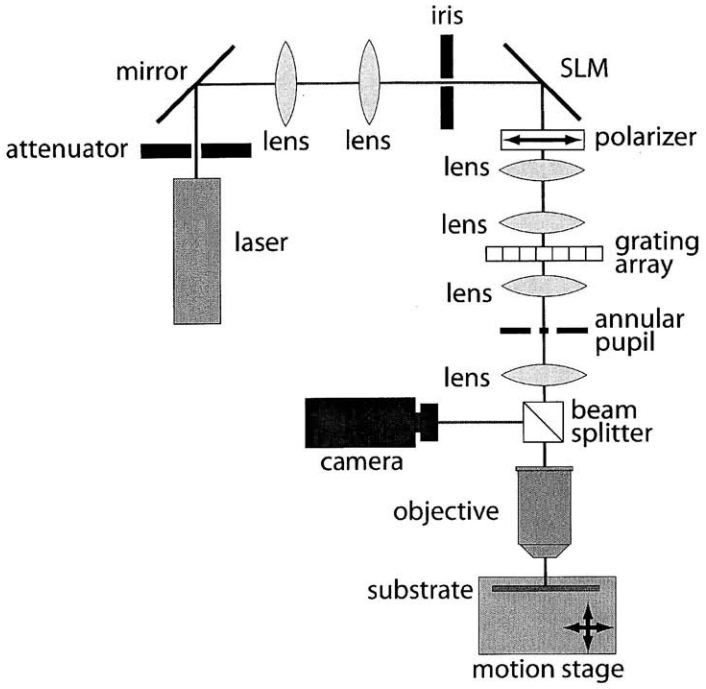

Figure 2.2.1: Schematic of the optical setup for laser ablation system.

Table 2.2.2: Specifications of the laser [4]

Wavelength	355nm
Average Power	3W @ 10kHz
Pulse Energy	1mJ/pulse @ 1kHz
Pulse Width	< 25ps
Repetition Rate	single shot to 25kHz
Output Beam Diameter	0.9mm

spots is,

$$5[\mathrm{J}/cm^2] = (2\mu m)^2 \times 1000 = 0.2\mathrm{mJ}. \tag{2.2.1}$$

Therefore, the required energy is 20% of the full energy that can be provided by the laser at 1kHz.

Prior to ablation experiments with the laser, power was measured at multiple points along the propagation of the beam while the laser current was set to its maximum of 43.2A and pulse width of 21.7nm, with repetition rate of 10kHz. Figure 2.2.3 shows the schematic of the setup for the beam power measurement and the power at each point. It was found that the laser could not output the maximum power

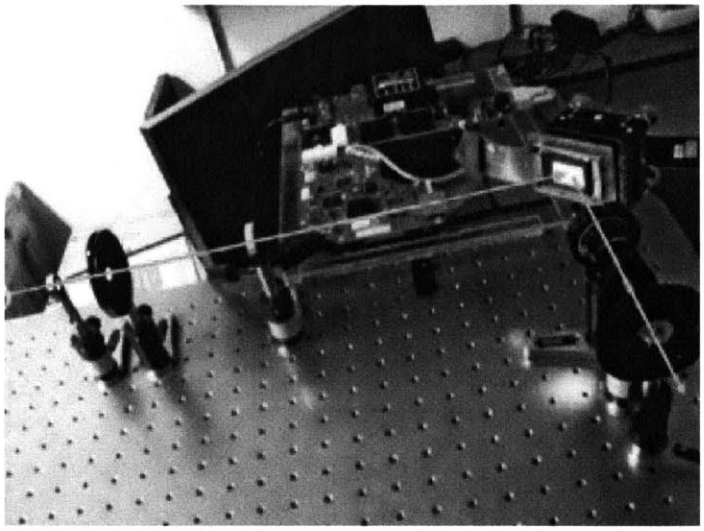

Figure 2.2.2: Optical setup of the SLM at approximately 45 degrees.

specified, and further, the output power was highly unstable at all times. This had significant effects on the experiments discussed below.

2.2.2 Optical Relay System

Figure 2.2.4 shows the geometry of the main imaging section of the proposed pixel repair system. The light diffracted by the grating array is relayed to the microscope objective by a pair of lenses: L1 and L2. This allows minimizing the diffraction artifacts produced by the small elemental grating aperture. In addition, the relay optics introduces a new degree of freedom by the magnification or demagnification of the field. The selection of the optimum relay lenses is critical for the overall system performance. An inadequate choice of relay optics would result in severely aberrated point spread functions (PSFs). Traditional optimization of optical systems relies on the use of ray tracing software such as Zemax. The optimum radius of curvature, glass and thickness of the lenses is found and the design is sent for custom fabrication. While flexible, this process is costly and requires long lead times. In order to minimize system cost (and time), an alternative approach is adopted. The optimum relay optics is found from a database of commercially available lenses. The pair of lenses is chosen to satisfy a set of constraints and their performance is evaluated using geometrical and

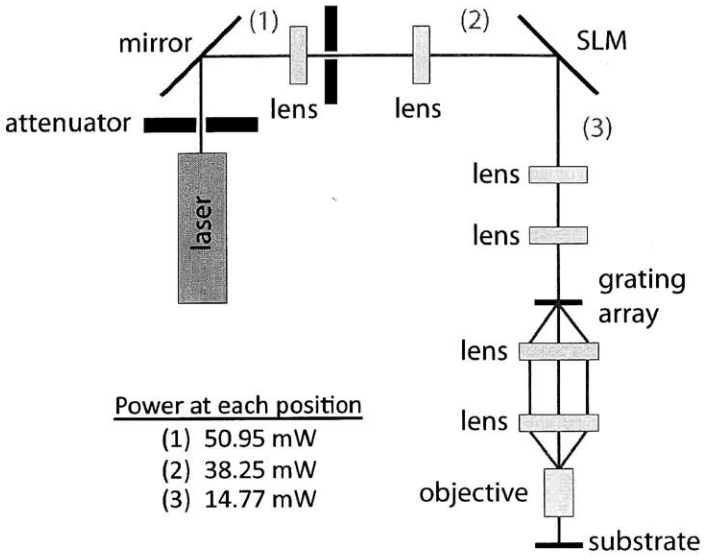

Figure 2.2.3: Schematic of optical setup and measured maximum power at each position along the beam path. Details of the optical setup will be discussed in Section 5.

Fourier optics formulations. The specifics of the optimization algorithm are explained in detail below.

The general specifications of the system are indicated in Table 2.2.4. The chosen microscope objective is Mitutoyos M Plan NUV infinity corrected 100x. The objective specifications are: $\mathrm{NA_{MO}} = 0.5$; working distance WD $= 11mm$; effective focal length, EFL $= 2mm$; depth of focus, DOF $= 1.1\mu m$; resolution, $R = 0.6\mu m$. Figure 2.2.5 shows a diagram of the microscope objective with its corresponding spectral

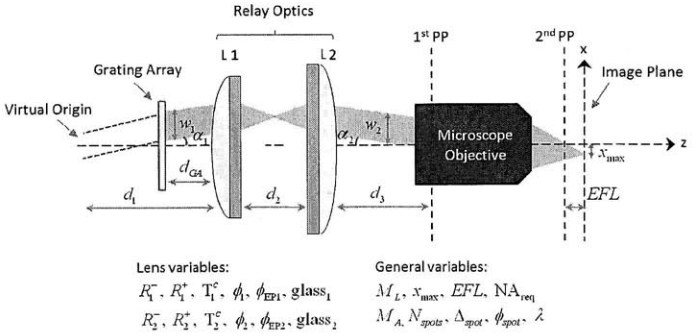

Figure 2.2.4: Schematic of the geometry of the main imaging section with relay optics and gratings to be optimized.

Table 2.2.3: General system specifications

Operating Wavelength λ	355nm
Spot Diameter ϕ_{spot}	$2\mu m$
Number of Spots N_{spots}	31×31
Spot Spacing Δ_{spots}	$30\ \mu m$
Required Numerical Aperture NA_{req}	0.2166
Maximum Spot Spacing x_{max}	0.45mm

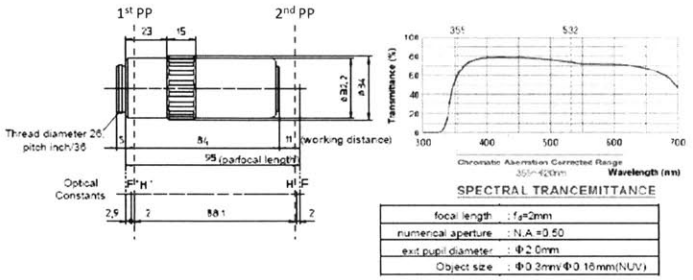

Figure 2.2.5: Specifications of Mitutoyo M Plan Apo NUV 100X **??**.

transmittance plot. The beam width, w_2, required to produce a spot of diameter, ϕ_{spot}, is given by:

$$w_2 = 2\text{EFL}\tan[\sin^{-1}(\text{NA}_{req})] = 0.887mm. \tag{2.2.2}$$

The input beam width (before the relay optics), w_1, is related to the output beam width by: $w_2 = M_L w_1$, where M_L is the desired lateral magnification. The angular magnification of the relay optics is: $M_A = 1/M_L$. The maximum angle, $\alpha_{2,max}$, to produce an off-axis point at a distance x_{max} from the optical axis is: $\alpha_{2,max} = 12.68\ °$. The complete desired grid at the image plane is shown in Figure 2.2.6. In this section we present preliminary optimization results designed to optimize the system performance of the optimization region indicated in Figure 2.2.6. Future work includes the extension of the optimization region to cover the entire field-of-view ($1 \times 1mm$).

The optimization algorithm begins by finding a feasible lens L2 that satisfies a set of prescribed constraints. In general, the lens variables are: radius 1, R_2^-; radius 2, R_2^+; center thickness, T_2^C; glass type, $glass_2$; lens diameter, ϕ_2; entrance pupil

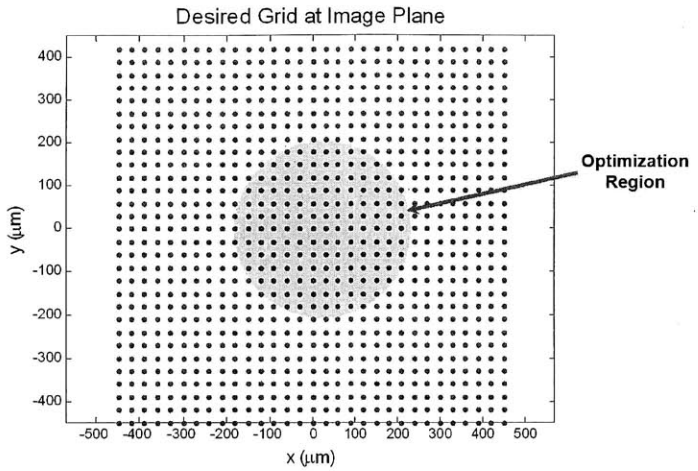

Figure 2.2.6: Desired grid at the image plane.

diameter, ϕ_{EPD2}. To minimize spherical aberrations, we only consider plano-convex lenses (i.e., one of the radius values is set to infinity). The lens parameters are chosen from a database of 356 commercially available lenses from the following major companies: Melles Griot, Thorlabs, and Newport.

Two constraints are imposed on the selection of lens 2. For the first constraint, the distance, d_3, is assumed to be equal to the lens effective focal length and the required diameter is computed. The required diameter is given by:

$$\phi_{req} = 2\left[\mathrm{EFL}_{k,2}^{(k)} \tan\left(\alpha_{2,max}\right) + \frac{w_2}{2}\right], \tag{2.2.3}$$

where, $EFL_{k,2}^{(k)}$ is the effective focal length of the k-th lens. To satisfy this constraint, the actual lens diameter, ϕ_2, needs to be equal or larger than the required diameter of equation 2.2.3. For the second constraint, the lens diameter is compared to the minimum grating array size given by: $GA_{size} = w_1 N_{spots}$. The distance between the grating array and lens 1 is computed by:

$$d_{GA} = \left(\frac{\phi_1 - GA_{size}}{2}\right)\frac{1}{\tan\alpha_1}. \tag{2.2.4}$$

To satisfy the second constraint, the lens diameter needs to be larger than the minimum grating array size, and the corresponding grating distance given by equation

2.2.4 needs to be physically possible (avoid configurations in which the grating array is in close contact with the lens).

Once a set of feasible lens 2 is found, the possible lens 1 combinations for each lens in the set is found by analyzing the database and imposing similar constraints as above, but with the additional constraint of the required magnification of the relay optics.

2.2.3 Blazed Grating Matrix

Here, we introduce the design and fabrication method of the blazed grating matrix.

Design of the Gratings

Some of the key parameters to be considered for design of the gratings are efficiency, accuracy, and fabrication feasibility. Blazed gratings (Figure 2.2.7) are capable of concentrating most of the energy into one diffraction order whose angle matches the refraction at the tilted face of the gratings [35], hence large efficiency can be obtained for that order. The grating equation is,

$$\sin\beta = \frac{m\lambda}{\Lambda}, \tag{2.2.5}$$

where β is the diffraction angle, m is the order of diffraction, λ is the wavelength, and Λ is the grating period. The refraction from the angled surface is,

$$n\sin\theta_b = \sin(\theta_b + \beta), \tag{2.2.6}$$

where $n$is the index of refraction of the gratings, and θ_b is the angle of the tilted surfaces. Therefore, considering the height of the wedges to be $t = \Lambda\tan\theta_b$, the condition for blazed gratings to diffract at angle β with wavelength λ and index of

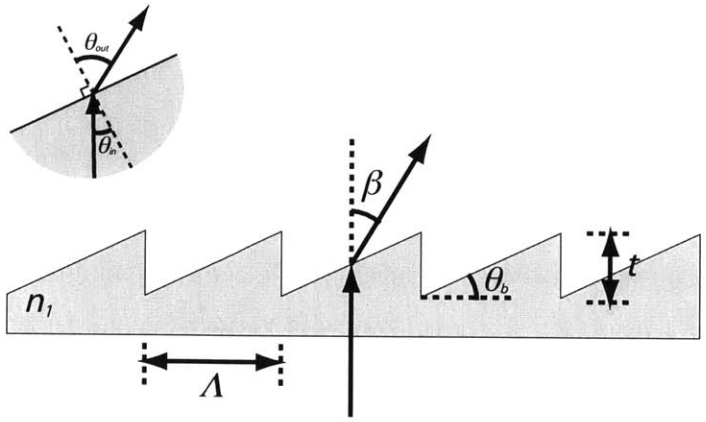

Figure 2.2.7: Schematic of the blazed grating.

refraction of n is,

$$\Lambda = \frac{m\lambda}{\sin\beta} \tag{2.2.7}$$

$$t = \frac{m\lambda}{n - \cos\beta}, \tag{2.2.8}$$

At the farthest corner of the matrix, the required grating period and height of the wedge are $\Lambda = 1.17\mu m$, and $t = 649nm$ when $m = 1$ and the angular magnification of the following relay optics M_A is 1, while for the cell next to the center, the period and height are $\Lambda = 23.7\mu m$, and $t = 709nm$ (Fig. 2.2.8).

2.2.4 Analysis of Fabrication Parameters and Tolerance

It should be noted that errors in the grating pitch, flatness of the wedged surface, angle of the wedge, or rounding of corners can lead to efficiency loss, aberration, or deviation in the diffraction angle. These factors must be analyzed and taken into account when designing the blazed gratings.

Analysis on the Number and Heights of Steps

Due to fabrication limitations, usually when blazed gratings are fabricated, their heights are discretized into finite number of steps, their features resembling stairs

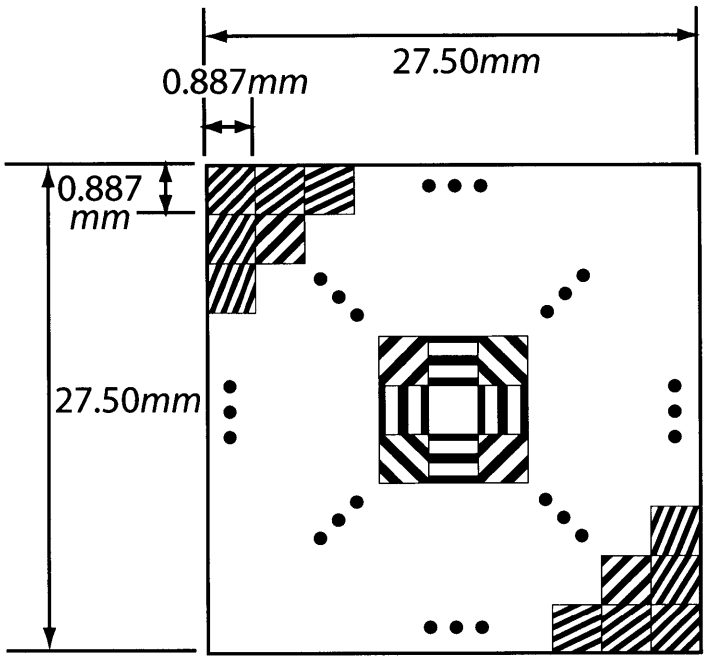

Figure 2.2.8: Design of the grating matrix. The blazed gratings are denoted as stripes, and not to scale. The grating in the red box (at the corner of the matrix) has the smallest pitch of $1.17\mu m$ when $M_A = 1$, $m = 1$, and the grating in the blue box (next to the center) has the largest pitch of 23.7m for the same conditions.

(hence sometimes called stair-case gratings). The number of steps that can be fabricated and their tolerance in height depend on the fabrication method and cost. In this section, we analyze the effect of this height disretization over the efficiency of the gratings in order to determine the minimum number of steps that is achievable.

We used finite difference in time domain (FDTD) method, particularly the Lumerical software package [10], to conduct this analysis. Bloch boundary conditions are imposed over a single tooth, and this is illuminated by a plane wave from the bottom of the structure, which is the side of the structure without the teeth. Figure 2.2.9 shows the transmission efficiency in terms of the number of steps of the grating. It can be seen that the efficiency asymptotically reaches 78%, and does not significantly change after around eight layers. Therefore, we choose our design of the structure to be eight layers, which is also a reasonable number in terms of the fabrication cost of the grayscale mask.

Optimization of the height of the blazed gratings was also achieved using the same

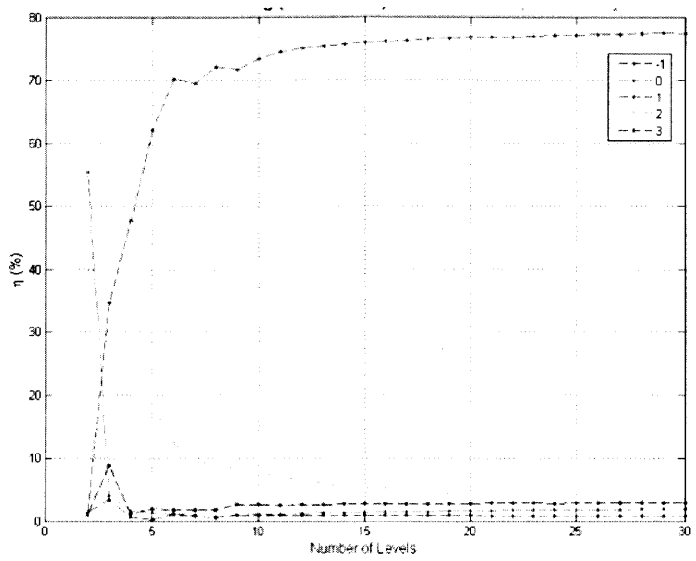

Figure 2.2.9: Simulated transmitted efficiency as a function of the number of steps for stair-case blazed gratings.

FDTD analysis method. It was found that the analytical height of ideal blazed teeth gave suboptimal efficiencies (fraction of the input power that goes into the desired diffraction order) for these structures at 72.2%, while an optimal height gave a higher efficiency of 74.6%. Note that although the optimal height of the blazed gratings are different for different pitches, due to fabrication cost and simplicity, we use a single height of 563nm, which is the mean of the optimum thicknesses. As can be seen from the below analysis, the efficiency is kept over 70% from using this single height.

Tolerance Analysis

There are a few types of errors that can be anticipated from fabrication of the blazed gratings. Here we analyze two types of errors: slope of the vertical edge and error of the heights of each grayscale step, which is equivalent to the error in angle of the angled surface of the ideal alternative (Figure 2.2.10). The influence of these errors was analyzed using FDTD, whose setup is as shown in Figure 2.2.11. Note that edge rounding is also taken into account in the simulation. Gratings at three positions in the matrix were analyzed for the two above-mentioned errors. Figures 2.2.12-2.2.14 show the results from the analysis, where the parameters for each grating

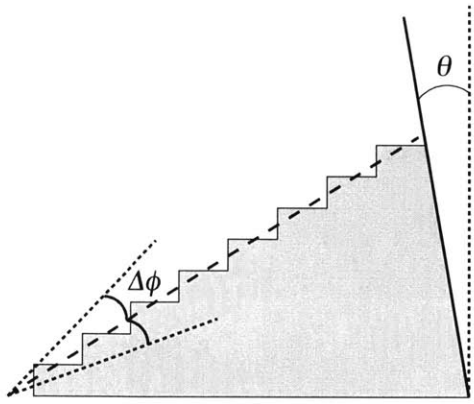

Figure 2.2.10: Schematic of the analyzed angle tolerances. θ is the angle of the vertical plane, and $\Delta\phi$ is the angle error of the inclined plane.

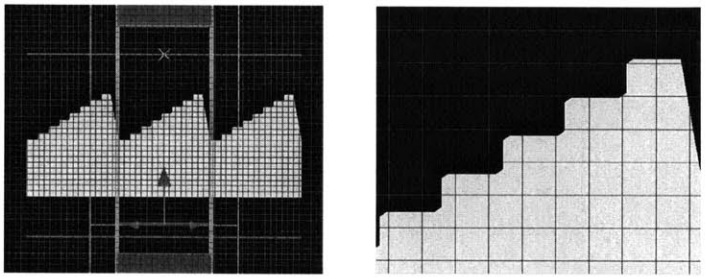

Figure 2.2.11: FDTD simulation setup for blazed grating fabrication tolerance analysis. Notice that discrete steps and edge-rounding was taken into account in the simulation.

are shown in Table 2.2.4. The corresponding height range, which is shown in the table, is the height of the total structure when the inclined surface angle is changed. Considering the fabrication techniques and tools that are used to fabricate these structures, as discussed below, this range is much larger than the expected tolerance range of fabrication. It can be seen from the figures that significant drop in efficiency can be observed at high errors, especially with errors in the angle of the inclined surface.

2.2.5 Fabrication of the Grating Matrix

The blazed grating array designed above can be fabricated using contact optical lithography. In order to obtain the blaze teeth structure, grayscale lithography is

Table 2.2.4: General system specifications

pitch [μm]	23.67	2.98	1.617
height for ideal case [nm]	655	655	655
efficiency for ideal case [%]	88	82.79	74.74
simulated range of inclined surface angle [degrees]	$-0.5 < \Delta\theta < +0.5$	$--2.5 < \Delta\theta < +2.5$	$-5.0 < \Delta\theta < +5.0$
corresponding height range [nm]	$450 < t < 860$	$520 < t < 792$	$495 < t < 825$
simulated range of vertical angle [degrees]	$0 < \Delta\phi < 10$	$0 < \Delta\phi < 10$	$0 < \Delta\phi < 10$

used, which is a method in which the exposure mask (or in some cases the dose of the e-beam, laser, etc) is varied continuously, providing continuously varying dose to the photoresist, which results in variation in its height. Here, we used a grayscale mask provided by Canyon Materials, Inc. [3]. These grayscale masks have true grayscale, for which they use patented glass products whose opacity is sensitive to electron beam exposure. This technology allows them to obtain a practical manufacturing resolution in the order of 0.25μm, as opposed to half-toned grayscale lithography techniques, which are typically limited to much lower resolutions with the same fabrication cost. Note that, for example, if eight levels of grayscale is required for the teeth of a blazed grating, the required resolution at the mask must be 1/8 of the pitch, hence if the resolution of the grayscale mask is 0.25μm, the minimum pitch of a blazed grating would be 2.0μm. In order to obtain smaller pitches using the same resolution, the number of graylevels must be decreased, which of course leads to lower diffraction efficiencies, more scattering, etc.

The fabrication process follows a typical one-layer lithography as shown in Figure 2.2.15. A fused silica wafer is coated with HMDS and then with standard photoresist OCG 825-20, provided by Clariant, Inc., and then prebaked in an oven at 90 °C for

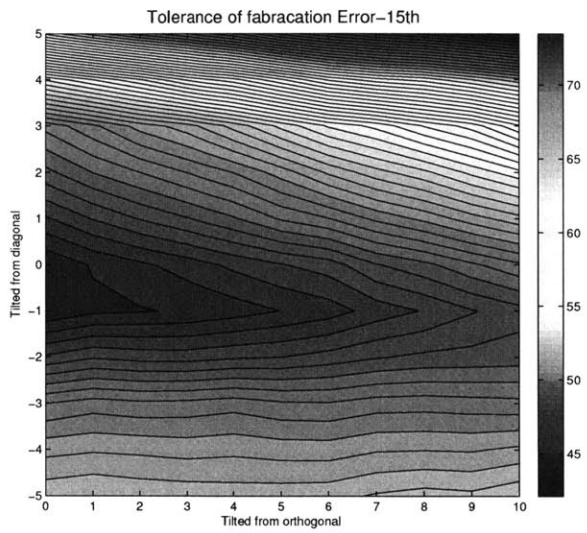

Figure 2.2.12: Efficiency variation with fabrication errors in vertical surface and diagonal surface for 1.617m pitch grating (closest to corner).

20 minutes. HMDS is a standard adhesion promoter to help the photoresist stay intact during and after developing. It is claimed by Canyon Materials Inc. that other photoresists work well with their graymasks as well, but this was not tested. After exposing the substrate with the grayscale mask for 2-4 seconds, the resist is developed with developer OCG934 1:1 for about 1.5 minutes, and then postbaked at 90 °C for around 2 hours. Reactive ion etching (RIE) is used to transfer the substrate with the three-dimensional resist profile to the fused silica substrate. The gases, their flow rate and chamber pressure used in this process are critical to the transfer of the profile, and are discussed in detail below. Finally, residual photoresist is ashed with oxygen plasma.

The transfer of the grayscale mask pattern into the blazed grating matrix in glass can be divided into two steps: transferring the grayscale mask pattern to the photoresist profile through the lithography steps, and transferring that profile into the glass through the etching step. Both steps must be optimized in order to achieve the desired structure, and each step will be discussed below. First, the relationship between the developed photoresist structure and the grayscale pattern must be determined. This relationship is dependent on the resist, exposure and bake parameters, as well as

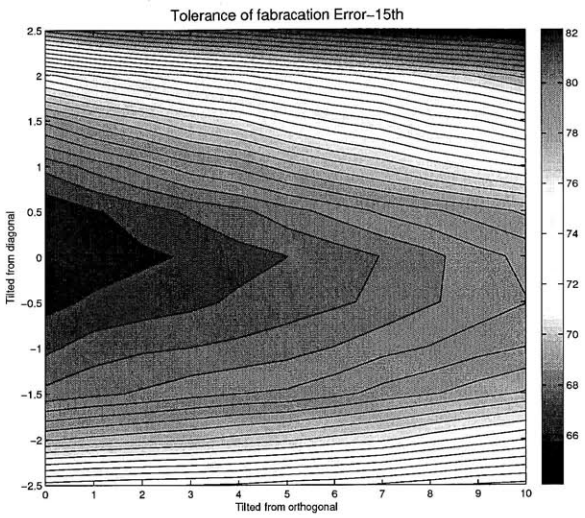

Figure 2.2.13: Efficiency variation with fabrication errors in vertical surface and diagonal surface for 2.98m pitch grating.

other process conditions. We conducted the following experiments with a calibration mask provided by Canyon Materials Inc., which consists of blazed and sinusoidal gratings, lens array structures, wedge structures, etc. with varying parameters including the optical densities of the pattern. The optical density (OD) is defined as,

$$OD = -\log(T), \tag{2.2.9}$$

where T is the transmission. First, the above-mentioned process is conducted with the calibration mask, while parameters such as prebake time, exposure time, etc. are varied. The profile of the resist is inspected using an optical microscope and measured using a contact surface profilometer. From multiple trials, the optimum parameters have been obtained for the process, many of which are critical for the success of creating the desired resist profile. For example, baking at temperatures too high or for too long time will reflow the resist and will have negative effects on its profile, hence these parameters must be adjusted accordingly and over-baking must be avoided. Also, the developing process must be conducted with care, since it is easy to wash away or delaminate the structures. Figure 2.2.16 shows the relationship

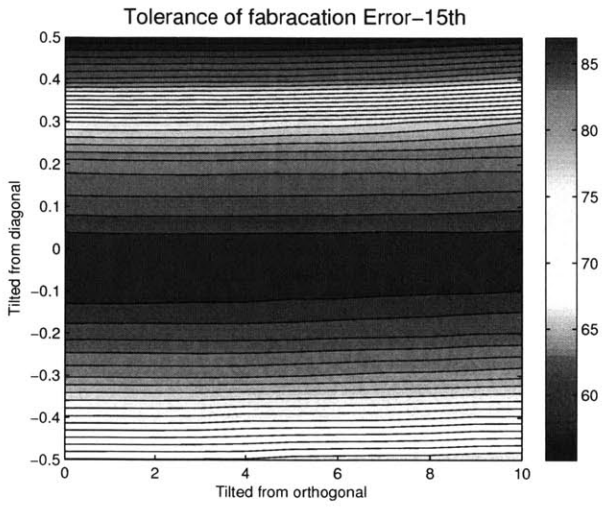

Figure 2.2.14: Efficiency variation with fabrication errors in vertical surface and diagonal surface for 23.67mm pitch grating (closest to center).

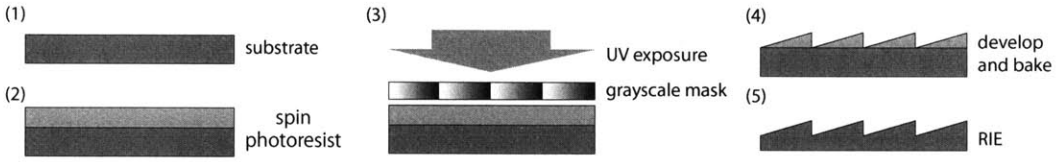

Figure 2.2.15: Fabrication process for blazed grating array with a grayscale mask.

between the optical density of the grayscale mask and the height of the resulting feature on the photoresist.

After the photoresist patterning process has been established, transfer of the pattern onto the glass substrate is investigated. The profile of the surface of the substrate is measured three times during the process with the above-mentioned parameters for lithography: before RIE, after RIE, and after oxygen plasma ash. With this method, the etch rate of both the photoresist and fused silica can be obtained, along with the profile of both the resist and fused silica. Figure 2.2.17 shows a profile of test blazed gratings with 10μm pitch. The original mask has 20 graylevels for these structures. Although the surface of the blazed gratings becomes rough from the etching, it can be seen that the triangular blaze pattern is reliably transferred to the fused silica wafer. There is a tilt of the vertical surface measured to be around 3 degrees, and also round-

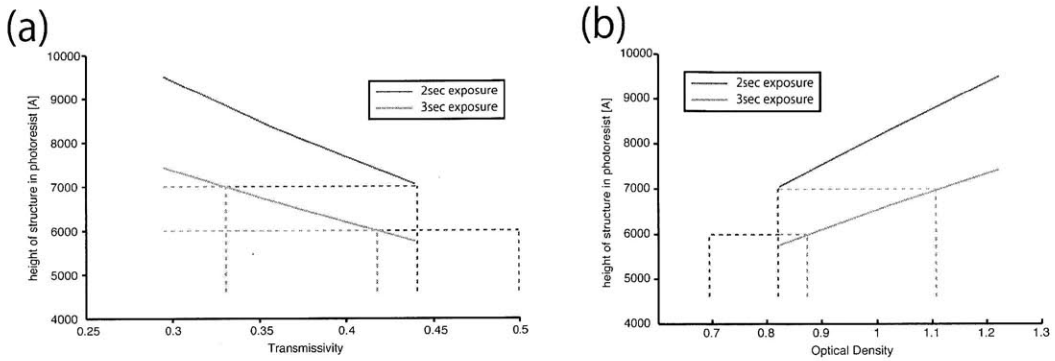

Figure 2.2.16: Relationship between transparency and profile height of the developed photoresist (a) and between the optical density and profile height of the developed photoresist (b) for optimized fabrication process parameters, obtained experimentally. (b) was obtained from (a) and equation 2.2.9. In both figures, red line shows the profile with 2 sec exposure with contact lithography, and the green line shows the profile with 3sec exposure.

ing of the tip can be observed. The gases that were used for the RIE process were: CF_4 30sccm and O_2 2sccm, and the chamber pressure was set to 100mTorr. CF_4 is the main etchant gas for fused silica, and O_2 etches photoresist slowly. The adjustments of the flow rates are important to control the etch selectivity and anisotropy of the etch, which determine the profile of the glass substrate after etching. The etch rate was around $20\mathring{A}$/sec with these parameters.

Once a mask is fabricated with the above method, it can be transferred with nanoimprint lithography onto another substrate (Figure 2.2.18) [62]. The key advantage of this process is that it is a large-area high-resolution low-cost method for nanofabrication, making either the CGH lithography or BGM multi-spot ablation technology even more cost effective. Especially, by using HSQ, a glass mask can be directly fabricated without further processing such as lift-off or etching.

2.2.6 Experimental Results

Single Spot Ablation Experiment

First, a single spot ablation test was conducted to verify the ability of the system to ablate without the grating array. Figure 2.2.19 shows the setup for this experiment,

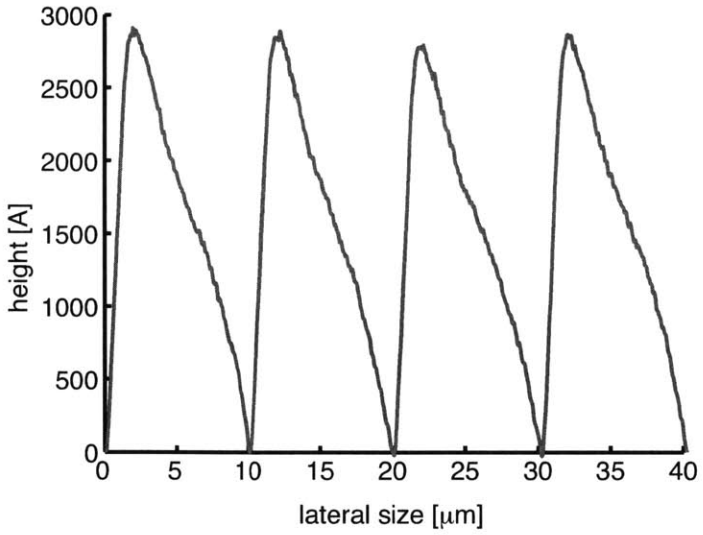

Figure 2.2.17: Profile of the fabricated blazed gratings with $10\mu m$ pitch.

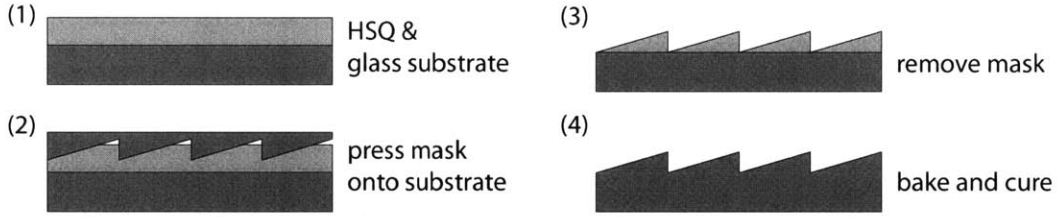

Figure 2.2.18: Process for nanoimprint lithography using HSQ.

and a glass substrate with 200nm of aluminum, 100nm of molybdenum and 1.5μ m of photoresist was used as a sample to be ablated. The power of the laser was varied to determine the effects of fluence at the substrate to the structure of the ablation that can be obtained, and a motion stage was used to move the substrate at 1mm/sec while the laser pulsed at 100Hz frequency for 1 second, hence ablating a spot every 10μm along a line of 1mm. Table 2.2.5 summarizes the fluences that were used for this experiment. Note that these fluences were calculated from the power at the laser and assuming a spot radius of 2.5μm, where since the exact spot radius at the substrate is difficult to measure, an approximate number was used.

The sample was measured under a scanning electron microscope (SEM) and an atomic force microscopy (AFM). The SEM micrograph and 1D, 2D, and 3D views of the measurements from the AFM are shown in Figures 2.2.20 to 2.2.23. Note that

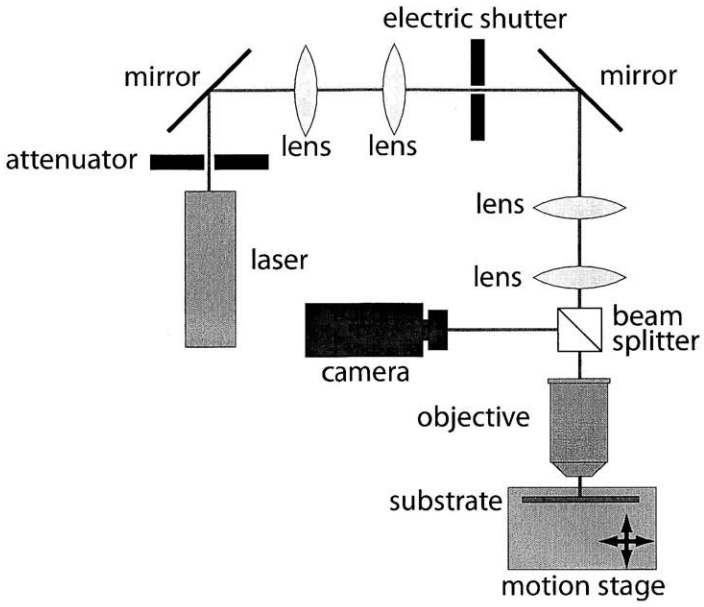

Figure 2.2.19: Schematic of the optical setup for single-spot ablation experiment.

Table 2.2.5: Power and fluences used for single-point ablation experiment

	Power at laser [mW]	Fluence at substrate [J/cm^2]
Experiment 1	0.26	7.945
Experiment 2	0.16	5.194
Experiment 3	0.07	2.139
Experiment 4	0.01	0.305

the measurement contains noise that is difficult to remove. It can be seen that the metal layers get fully ablated above fluences of $7.9J/cm^2$, but below that, only a small defect on the surface is observed. Further, below $0.3J/cm^2$, the photoresist on the top layer of the structure does not fully ablate. We call this the critical fluence, and is in good agreement with literature. Note that the beam intensity has a Gaussian profile, and therefore the power is larger at the center than at the edges of the beam, which is the reasons for the non square shape ablation and small damage spots. The hump that can be observed for higher power ablations are thought to be due to the aberration and fluctuation of the laser input and the optics that the beam passes through.

From the above measurements, we confirm the possibility of ablation of metal

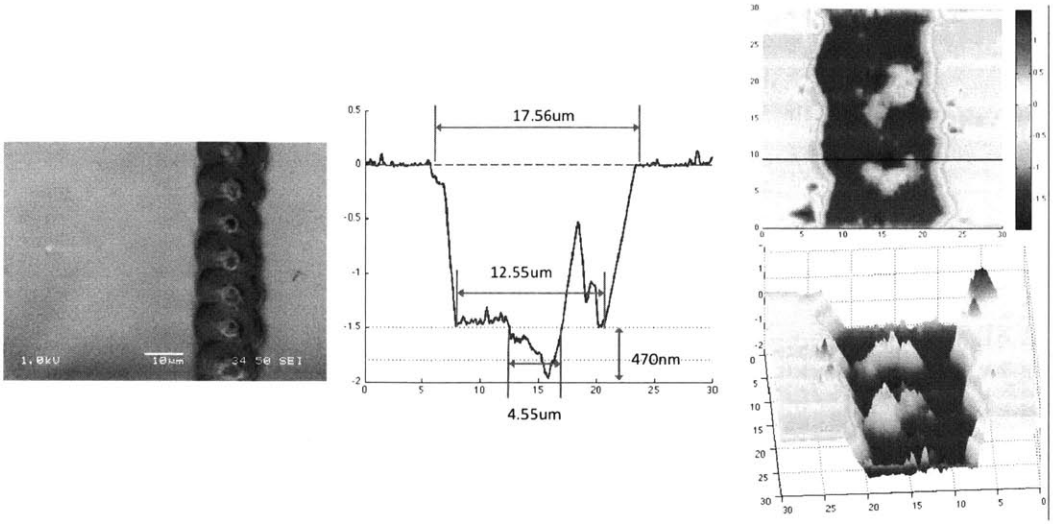

Figure 2.2.20: SEM images and AFM measurements for experiment 1 (c.f. Table 2.2.5).

and photoresist layers with our optical setup discussed above. Further, by tuning the laser power accordingly, we are able to obtain selective ablation of either only the photoresist or photoresist and metal together, not affecting the glass substrate underneath.

Multi-spot Ablation and Spot Control with Binary Grating Matrix

After understanding the single spot ablation characteristics, we conducted a multi-spot ablation experiment using a grating array. Before using blazed gratings as mentioned above, first, we used binary phase gratings to obtain the parameters for the setup and verify the possibility of multi-spot ablation. In order to do so, we fabricated a binary grating array of 7×7 (Figure 2.2.24 (a)) with a chrome mask purchased from Advanced Reproductions, Inc. [5]. Their limit for critical dimensions was $3\mu m$, hence the minimum pitch for the binary gratings was $6\mu m$. The binary phase grating array was fabricated using a similar process as the blazed gratings with modifications in some of the parameters. Figure 2.2.24 (b) shows an optical microscope image of the fabricated gratings. This grating was set into the experimental setup in place of the blazed grating array, and was tested. Note that since binary gratings have multiple

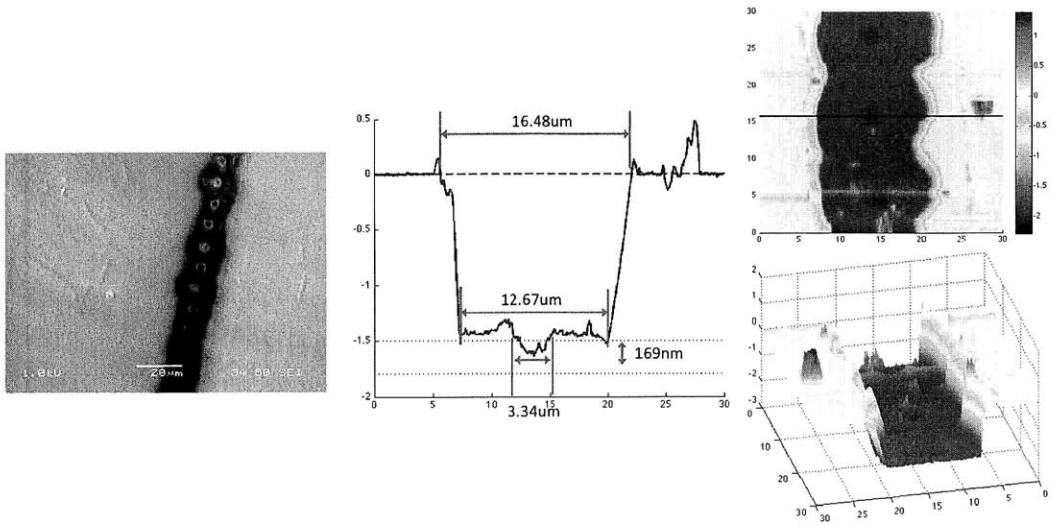

Figure 2.2.21: SEM images and AFM measurements for experiment 2 (c.f. Table 2.2.5).

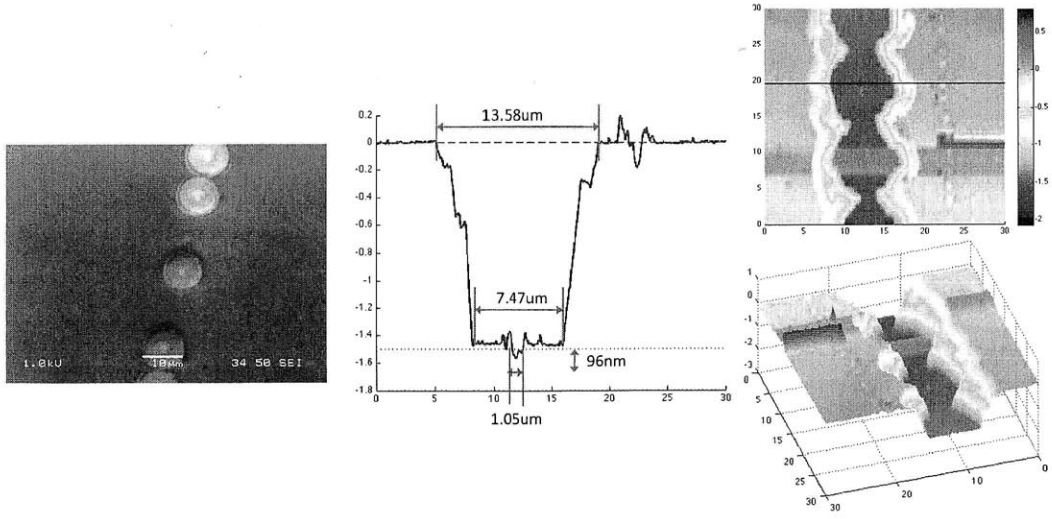

Figure 2.2.22: SEM images and AFM measurements for experiment 3 (c.f. Table 2.2.5).

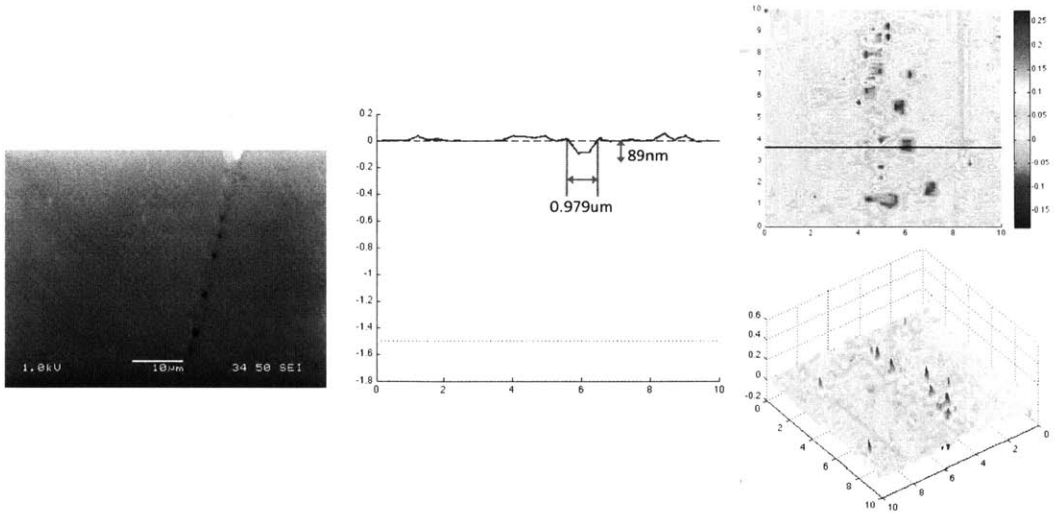

Figure 2.2.23: SEM images and AFM measurements for experiment 4 (c.f. Table 2.2.5).

diffraction orders, the transmission efficiency of each order will be lower than the case of a blazed grating. Beam from the first diffraction order will be used for all gratings. Sets of apertures and annular pupils were used to eliminate beams from higher order diffraction, but otherwise, the system was identical to the one for blazed gratings. In order to verify the formation of spot matrix on at the substrate plane, a camera was set behind the substrate plane along with an objective lens for magnification (Figure 2.2.25). From the image taken by the camera, it was verified that a spot matrix of 7×7 was formed, which corresponds to the 7×7 binary phase grating matrix (Figure 2.2.26).

Further, we conducted an experiment to turn on/off each spot individually by using the SLM. Figure 2.2.27 (a) shows an image at the substrate plane when the SLM was controlled to turn on every other spot, resembling a checkerboard, as shown in Figure 2.2.27 (b). Similarly, the SLM can be configured to arbitrarily control the state of each spot, for example, every other vertical line (Figure 2.2.29 (a,b)), or every other horizontal line (Figure 2.2.29 (a,b)).

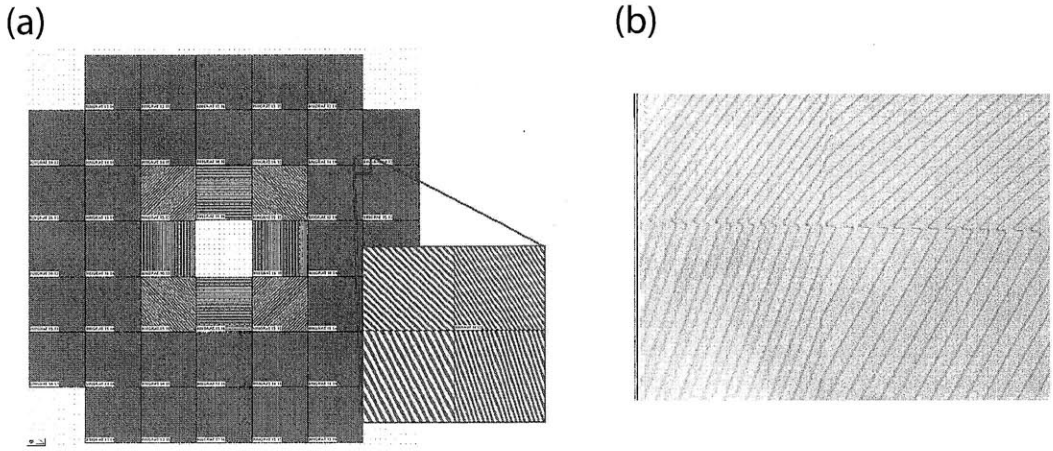

Figure 2.2.24: (a) Design of the binary grating matrix. (b) Optical micrograph of the grating structure.

Multi-spot Ablation Experiment with Blazed Grating Matrix

Multi-spot generation experiment was conducted with the BGM as well, with a similar setup as shown in Figure 2.2.25. Figure 2.2.30 shows the intensity profile at the camera, corresponding to the substrate plane. The spots have been measured to show less than 5% difference from each other, generated from different pitch gratings.

2.2.7 Conclusion

A system to ablate multiple spots on a substrate has been designed and experimentally verified, using a high-power pico-second UV laser, relay optics, an SLM, and a blazed grating array. Especially, we have pursued the use of off-the-shelf optical components and optimization of their selection. The relay lens system where lenses with minimum aberration over the imaging area were selected from a database of components. We have designed and fabricated a blazed grating matrix with grayscale optical lithography, and experimentally verified its capabilities of single-spot ablation and multi-spot distribution to a matrix with dynamic switching of individual spots.

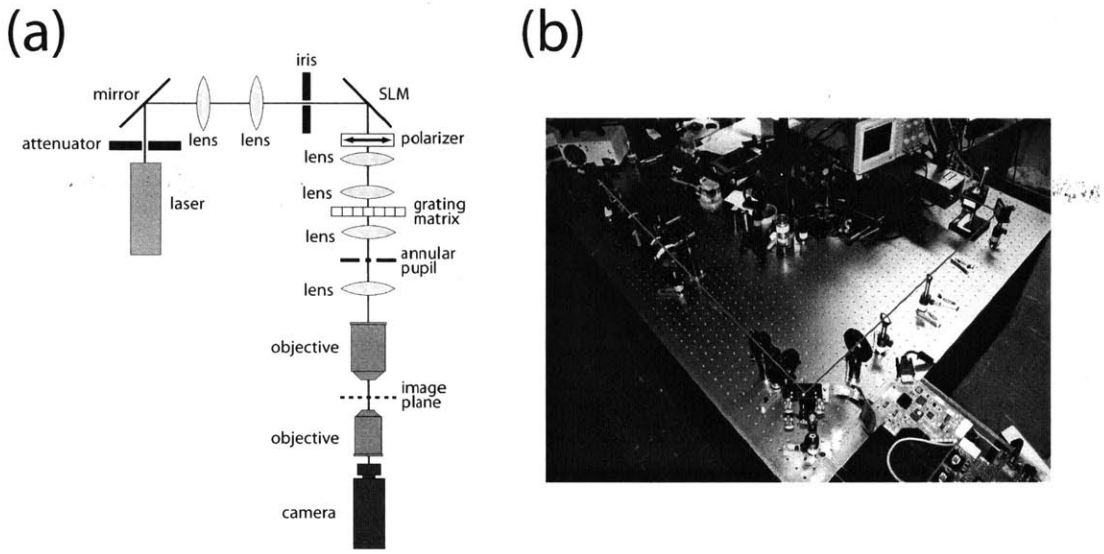

Figure 2.2.25: (a) Schematic and (b) Photograph of optical setup for multi-spot imaging at substrate plane.

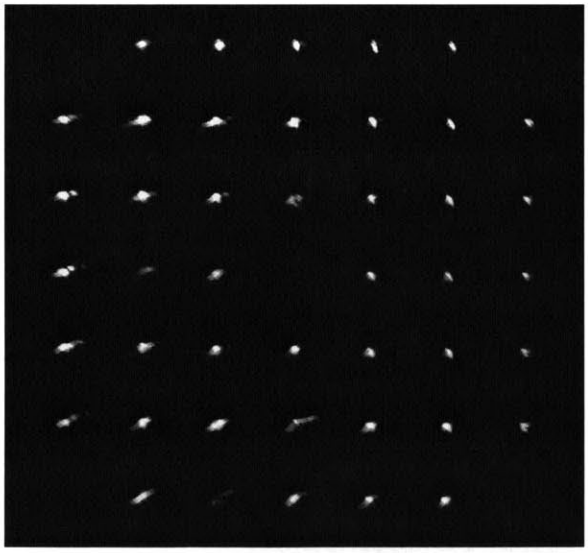

Figure 2.2.26: Multi-spot image at substrate plane, corresponding to the grating matrix as shown in Figure 2.2.24. The distance between the spots was approximately $29\mu m$ (designed for $30\mu m$). Aberration for some spots can be observed due to fabrication and alignment errors.

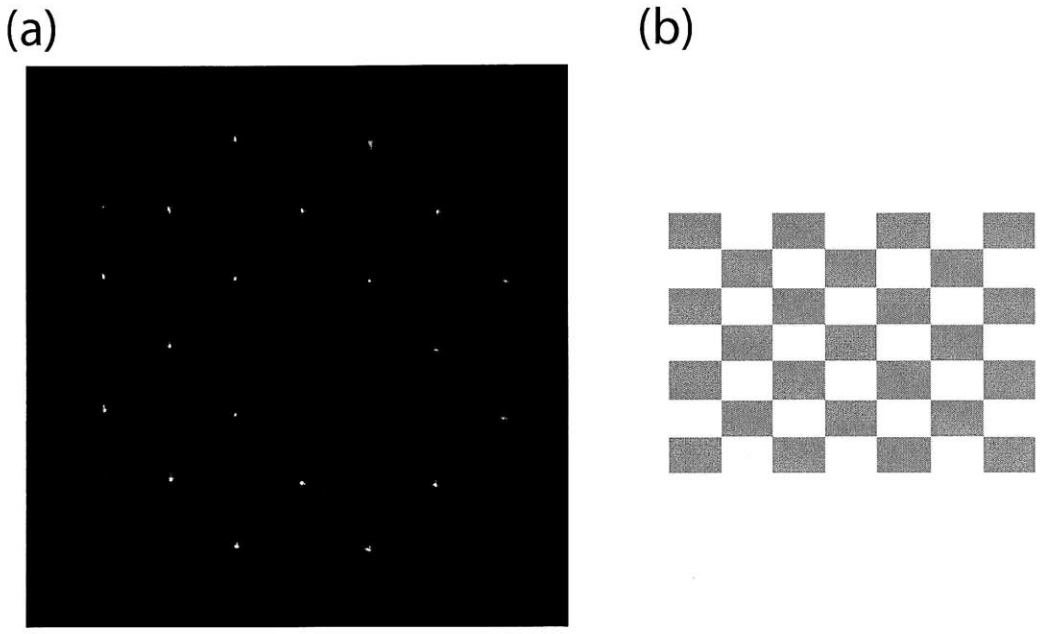

Figure 2.2.27: Patterns of spots at the substrate plane generated by controlling the SLM. SLM configuration for the checkerboard (a) and the image of the spots at the substrate plane (b).

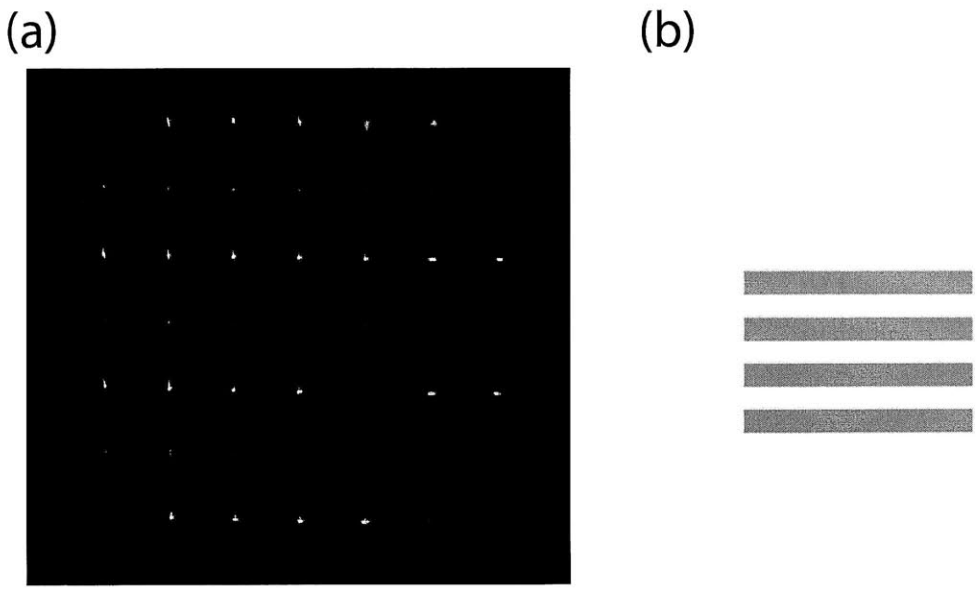

Figure 2.2.28: Patterns of spots at the substrate plane generated by controlling the SLM. SLM configuration for the horizontal stripes (a) and the image of the spots at the substrate plane (b).

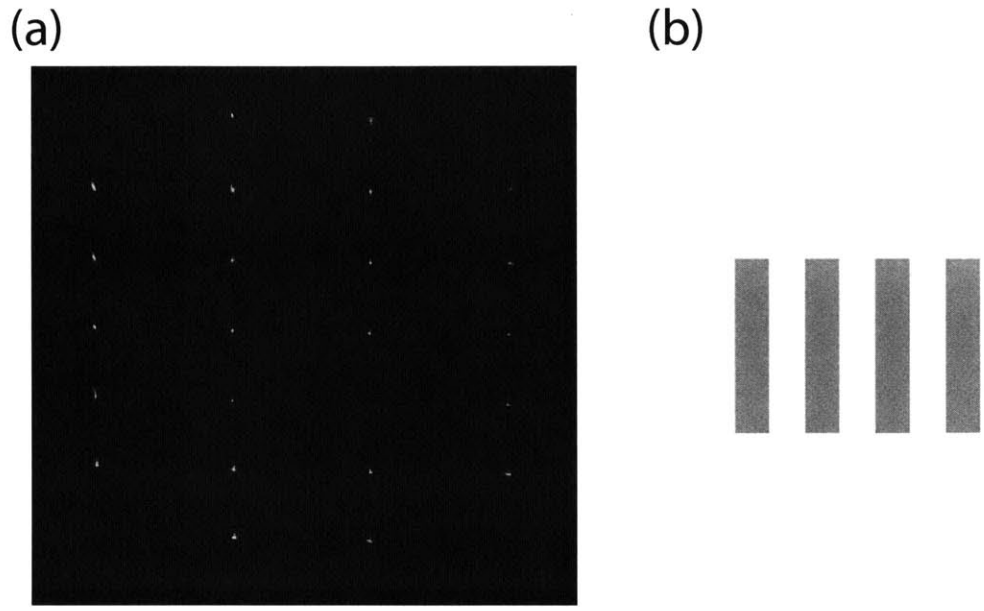

Figure 2.2.29: Patterns of spots at the substrate plane generated by controlling the SLM. SLM configuration for vertical stripes (a) and the image of the spots at the substrate plane (b).

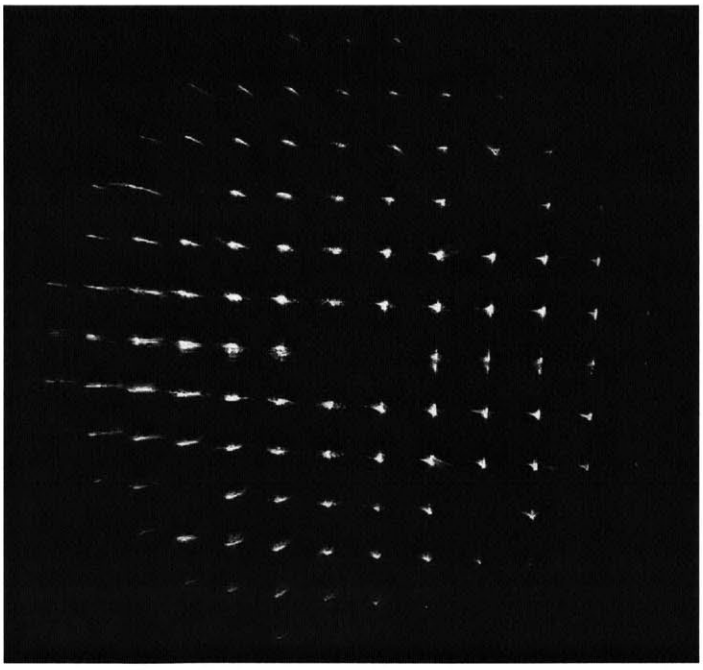

Figure 2.2.30: Intensity at the substrate plane from the multi-spot experiment with the blazed grating matrix. Aberration can be seen at the spots which are due to misalignment of the optics in the setup.

Chapter 3

Sub-wavelength Optics for Imaging

While refractive lenses have been widely used in many industries due to its ease of fabrication, gradient index (GRIN) lenses possess large potential, controlling light propagation utilizing its entire volume as opposed to using only the interaction at the surface as with refractive lenses. However, the problem with GRIN lenses has been the difficulty in its fabrication. Although techniques such as ion doping and layered structures have been used to fabricate GRIN lenses, these techniques are limited in the type of gradient that can be embedded into an optical component. In this work, sub-wavelength nanostructures will be used to design and fabricate an almost arbitrary effective index gradient in a structure. Especially, design and fabrication of a 2D Luneburg lens will be investigated.

3.1 Hamiltonian Optics

In order to obtain the required functionalities and performances of such devices based on non-periodic nano-photonic structures, it is crucial to establish an effective design and optimization method. There has been work on methods to use the "effective index" of the structure [46], but since in general the index is dependant on the direction of wave propagation as well as position in space, it is not straight forward to apply classic methods of electromagnetic propagation in inhomogeneous materials.

Here, we use Hamiltonian optics as a computationally inexpensive and accurate

method to obtain ray trajectories within non-periodic nano-photonic structures, given the initial positions and k-vectors of the rays. This method consists of solving a set of coupled ordinary differential equations that include the Hamiltonian, which is a conserved quantity along the ray trajectory. By using the Hamiltonian optics method, the propagation of rays can be calculated with significantly less computational cost compared to methods such as the finite difference in time domain (FDTD) method. This makes the use of optimization techniques feasible for structure design with the Hamiltonian optics method.

3.1.1 Hamiltonian Optics for Sub-wavelength Structures

If the spatial variation in a structure is slow enough, the electromagnetic field propagates adiabatically [60] throughout the structure, preserving the mode. Moreover, the dispersion relation of the locally periodic lattice remains approximately valid, the propagating electromagnetic waves behaving similar to Bloch waves. Some examples of spatial variations in a structure include variations of lattice spacing as in Figure 3.1.1 (a), or variations of rod diameter as in Figure 3.1.1 (b). Since the temporal frequency ω of the optical field is fundamentally a conserved quantity in the linear optics regime, in [66] it was shown that $\omega(\mathbf{r}, \mathbf{k})$ expressed as function of the Cartesian coordinate $\mathbf{r}$ in the lattice and the momentum coordinate $\mathbf{k}$ (*i.e.*, the wave vector) can serve as the Hamiltonian for optical field propagation. In Hamiltonian optics, ray trajectories through a smoothly varying structure are expressed as a set of differential equations consisting of the Hamiltonian, which is a conserved quantity along the ray, position, and momentum. Note that in conventional Hamiltonian optics, the index of refraction of the material was assumed to vary slowly, while here, the dispersion surface, which is dependent on the local periodic structure, is assumed to change slowly while the actual index of refraction changes with rather high spatial frequency. The solution to these Hamiltonian equations

$$\frac{d\mathbf{r}}{dt} = \frac{\partial\omega}{\partial\mathbf{k}}, \frac{d\mathbf{k}}{dt} = -\frac{\partial\omega}{\partial\mathbf{r}}, \tag{3.1.1}$$

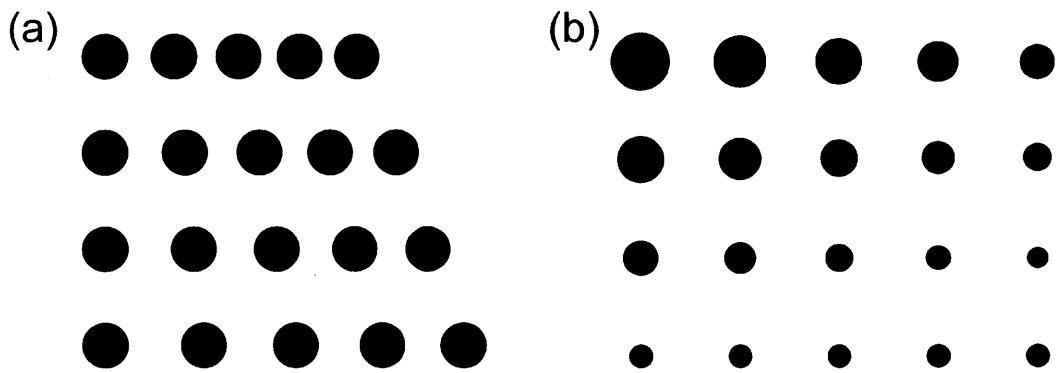

Figure 3.1.1: Schematic diagram of a lattice with (a) varying lateral spacing and (b) varying radius).

where **r** is the position, **k** is the k-vector, and t is time, can be thought of as ray trajectories. These differ from conventional ray trajectories, for example in GRIN optics [65], in that the concept of the macroscopic refractive index has been replaced by the local dispersion diagram. The notion of an effective refractive index can still be retained as the inverse of the gradient $|\partial\omega/\partial\mathbf{k}|$, but caution must be taken since, in general, the vector gradient has strong directional dependence. The analysis developed in [66] and adopted here is valid provided the critical length in the variation of the structure does not exceed the ratio of the Hamiltonian over the magnitude of its gradient.

It is assumed that the variation in the effective index along the surface of the structure is small enough that it can be approximated as being uniform around the point of entrance of the ray. This assumption has been verified by comparing with the FDTD simulations.

Matlab program for Hamiltonian Optics for Sub-wavelength Structures

In order to implement Hamiltonian optics into ray propagation analysis of non-periodic structures, first, a library of dispersion relations for periodic lattices are created using MPB, which is a mode solver developed by S. Johnson et al. [2].

Using Matlab's Runge-Kutta solver ode45, equations 3.1.1 are solved incrementally along the ray path. First, from the current coordinates r and the lattice distri-

bution, the local lattice constant is obtained and its dispersion diagram is looked up from the library that has been created and stored. Using the current k-cooridnates $\mathbf{k}$, the position on the dispersion diagram is determined, from which $\partial\omega/\partial\mathbf{k}$ can be calculated. Also, $\partial\omega/\partial a$ is calculated in the vicinity of the lattice constant at that position, and combined with $\partial a/\partial r$, the right hand side of the second equation of 3.1.1 can be calculated. Refer to Appendix C for the code.

Along the ray trajectory, the optical path length is also calculated at each point as,

$$OPL = \int_{\Gamma} n_{eff}(q)\sqrt{\dot{q}_x^2 + \dot{q}_z^2}ds, \tag{3.1.2}$$

where Γ is the ray trajectory, the dot denotes the derivative with respect to the time variable s, and n_{eff} is the effective index at each spatial coordinate along the ray. It is worth noting that the OPL is the Lagrangian corresponding to the Hamiltonian system of equations 3.1.1 and is, therefore, stationary for any congruence of rays propagating through the medium. The stationarity property is consistent with Fermats principle [24, 21]. Effective indices in two orthogonal coordinates $n_{eff,i}(i = x, z)$ are also calculated in MPB using the Hellman-Feynman theorem [63].

In terms of the boundary between the structure and air, the effective index of refraction at the point of ray entrance is taken and phase matching conditions are applied.

The required computation cost of the Hamiltonian method is significantly smaller than FDTD (few minutes for the Hamiltonian optics method versus a few hours for the FDTD method in the 2D simulations in Section 4), since once the library is created, the differential equations are only solved along the ray trajectories as opposed to being solved throughout the whole field of interest (plus the extra boundary layers) in FDTD methods. This enables the use of this method as a design and optimization tool for non-periodic photonic structures on top of being an analysis tool.

Note that, however, as either the variation range of the lattice parameter becomes large or the number of parameters for the lattices become large (for example, if the vertical and lateral lattice constants are assumed to vary independently across the

structure, or if a rod structure is allowed to have ellipticity), the size of the dispersion library becomes large and takes more space in the memory of the computational system. Therefore, it is important to tailor the library to store only the required lattice variation in the structure of interest.

3.1.2 Phase Space Representation

The propagation of state in k-space can be calculated from equations 3.1.1, similar to the ray propagation in physical (r-) space. Since the free-space frequency ω_0 is conserved, at each point in space, where a dispersion relation is defined, there is an equi-frequency contour in k-space which the ray must lie on when it is at the specific position in space. As the ray propagates, along with the change in the local structure and hence the change in the local dispersion relation, the equi-frequency contour on which the ray lies shifts. Figure 3.1.2 (a) shows the equi-frequency contours of lattices when the lateral lattice spacing is varied, and Figure 3.1.2 (b) shows those when the diameter of the rods are varied. The state in k-space shifts accordingly, where the direction is defined by the first Hamiltonian equation. Notice that for the contours for smaller lateral spacing in Figure 3.1.2 (a), there are certain regions in k_x which a state does not exist. This suggests a bandgap for the specific condition, and the ray is prohibited from being in this state.

The trajectory in k-space can be plotted just like the rays in r-space. By obtaining the region in which the ray can propagate in k-space from the range of variation in the local periodic structures and the input frequency, the characteristics of the ray trajectories can be analyzed, and this can be used for the design of the non-periodic structures.

3.2 Design of GRIN Rod Structures

Rod lenses are one of the most widely used type of GRIN lens due to its fabrication feasibility using ion diffusion in glass. However, there are problems associated with this fabrication method, such as limitation in the control of the gradient in the index

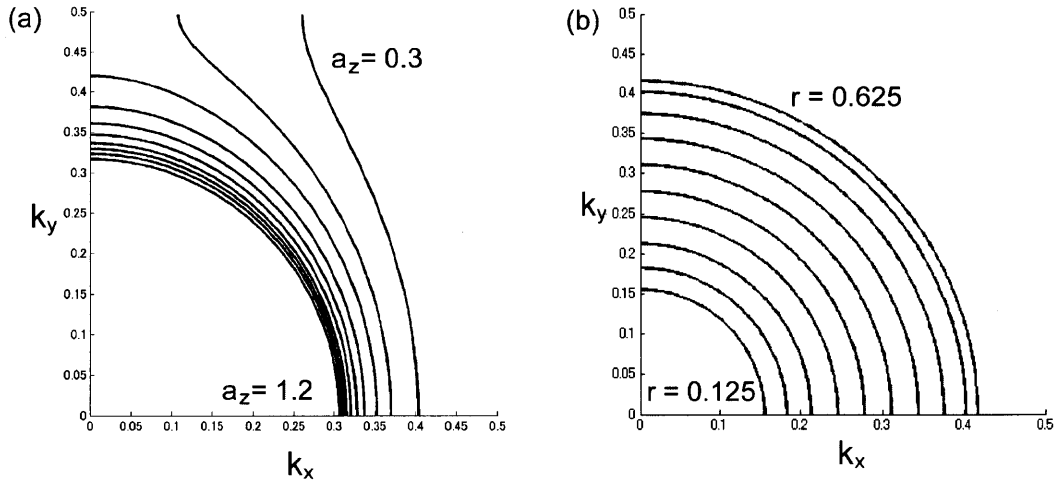

Figure 3.1.2: Equi-frequency contours at various lateral lattice spacing with same rod radius (a), and various radius with same lattice spacing (b).

that can be applied to the structure. Therefore, it is difficult to correct for the spherical aberration within the structure, or comatic aberration when the application requires incident beam that is not parallel to the optical axis.

In the case of the example GRIN structure discussed below, we start with a four-fold-symmetric structure of cylindrical rods in 2D and add gradual variation in the radii of the rods. The refractive index of the rods is $n_{rod} = 3.45$ and they are surrounded by air ($n_{air} = 1$). Figure 3.2.1 shows an example of an electromagnetic field propagating through a nanostructured GRIN with a quadratic variation in the radial direction

$$R(r) = a_0\left(1 + a_2\frac{r^2}{2}\right), \tag{3.2.1}$$

simulated with Hamiltonian Optics and a finite-difference-in-time-domain (FDTD) software, MEEP [2]. The dielectric rods have $n = 3.45$, and variable radius $0.3856a < R < 0.4a$, where a is the lattice constant. The structure is probed with a plane wave whose electric field is polarized out of plane with frequency, where c is the speed of light in free space. It can be seen that the light focuses at focal length $176.37a$. The intensity at the focal plane is as shown in Figure 3.2.2. The wavefronts extracted from the FDTD simulation are within $\lambda/8$ RMS over the entire wavefront surface compared to the wavefronts obtained from Hamiltonian ray tracing outside of the

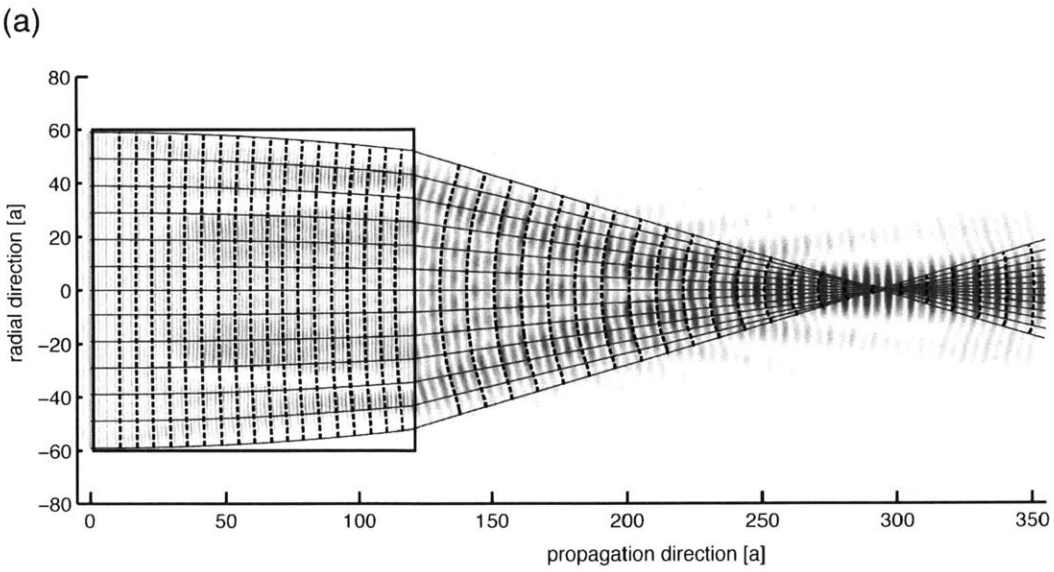

Figure 3.2.1: Hamiltonian ray tracing and FDTD results overlaid for comparison. The solid lines show the rays, and the dashed lines show the wavefronts obtained by calculation of optical path lengths along the rays.

structure, and $\lambda/6$ RMS inside. Note that while FDTD simulations, which solves Maxwell's equations directly, take into account the effect of interference between the propagating rays and reflected rays at the interface of the structure, as can be seen in the FDTD results in Figure 3.2.1, the Hamiltonian ray tracing is a geometric optics approach where these effects are not considered. Therefore, the wavefront distortion caused by the interference increases the wavefront error between the two methods. Designing of an anti-reflective structure at the boundary to reduce this effect will be pursued in the future.

The Hamiltonian ray trace was two orders of magnitude faster than the FDTD when run on the same computer. Further improvement would be expected in fully three-dimensional geometries.

We now demonstrate the design of a nanostructured GRIN lens with with spherical aberration correction We implement this in the lattice of Figure 3.1.1 (b) as

$$R(r) = a_0 \left(1 + a_2 \frac{r^2}{2} + a_4 \frac{r^4}{4}\right). \tag{3.2.2}$$

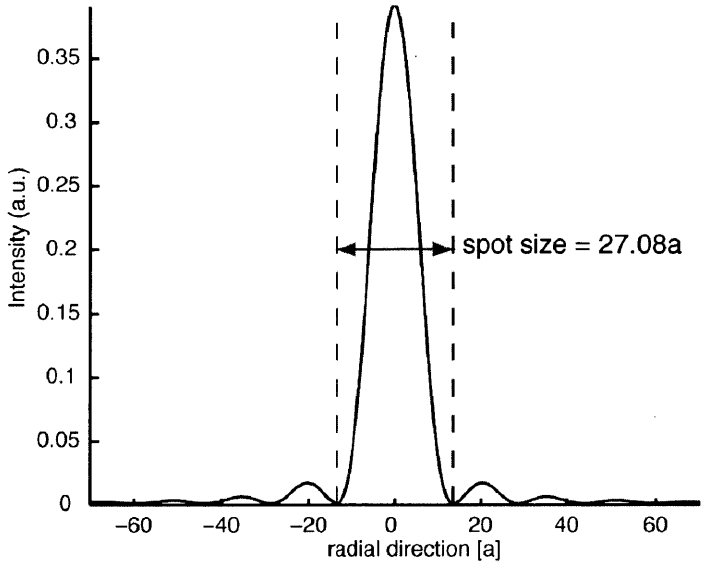

Figure 3.2.2: The intensity profile from FDTD at the focal plane of Figure 3.2.1.

Note that we use a quartic effective index term in addition to the quadratic index distribution normally seen in conventional bulk rod lenses, since spherical aberration are known to be quartic, and as shown in [53], for example, a quartic term in the index distribution are known to be able to compensate for it.

The linear and quadratic coefficients are kept constant at $a_0 = 0.4$ and $a_2 = -2 \times 10^{-5}$, and the quartic coefficient is varied for minimum aberration. As cost function for our optimization process, we use the RMS spot center and spot size as defined in terms of the rays by:

$$r_{RMS}^2 = \frac{1}{N}\sum_{i=1}^{N}(x_i - x_R)^2 \text{, where } x_R = \frac{1}{N}\sum_{i=1}^{N} x_i. \tag{3.2.3}$$

The focal length is defined as the distance to the plane with minimum RMS spot size.

Figure 3.2.3 shows the RMS spot size as function of angle as obtained from Hamiltonian ray tracing and the ratio of spot size as obtained from FDTD simulations to the diffraction limited spot size. Figure 3.2.4 shows the same as function of the parameter a_4. For small angles, the RMS spot size in Hamiltonian ray tracing tends to zero, while the FDTD spot size, which takes into account diffraction effects, tends

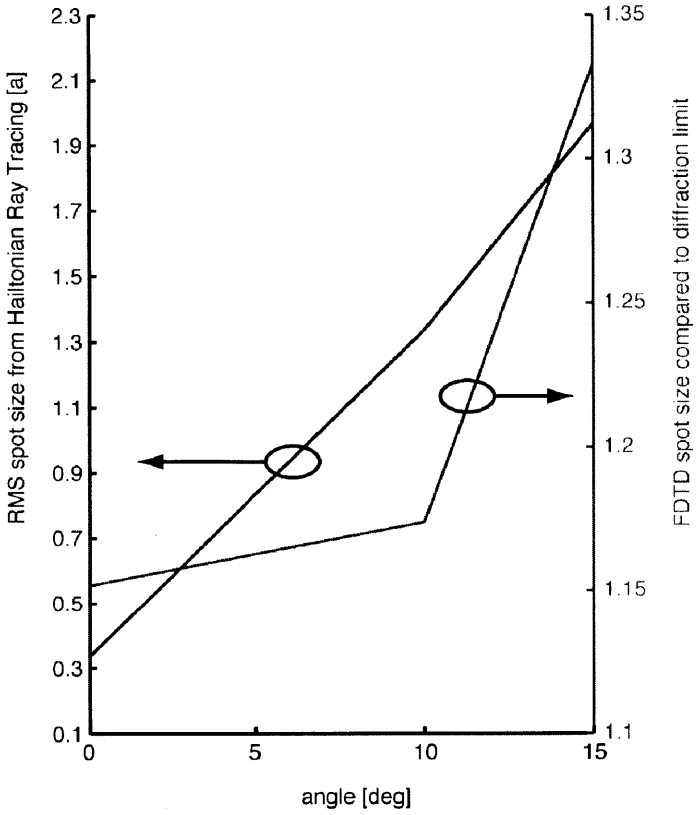

Figure 3.2.3: Comparison of RMS spot size from Hamiltonian Optics and FDTD spot size as a function of angle.

to the diffraction limited spot size $w = \lambda/NA$, where NA is the numerical aperture, and is approximately 0.34 in this case, whose value varies according to the specific structure. Due to discretization in space and time in the FDTD method, the spot size measured from these results has a finite grid resolution limit. This limit could be comparable or larger than the improvement in spot size obtained by optimization. Of course, the grid resolution can be improved by having a finer discretization in the computation, but with the cost of quickly increasing computational power. The resolution of the Hamiltonian method is currently under investigation.

Figure 3.2.5 shows the RMS focal length and spot size as function of a_4 for different values of the angle of incidence θ with respect to the optical axis. The minimum spot size at $\theta = 0$ is at $a_4 = 2 \times 10^{-10}$.

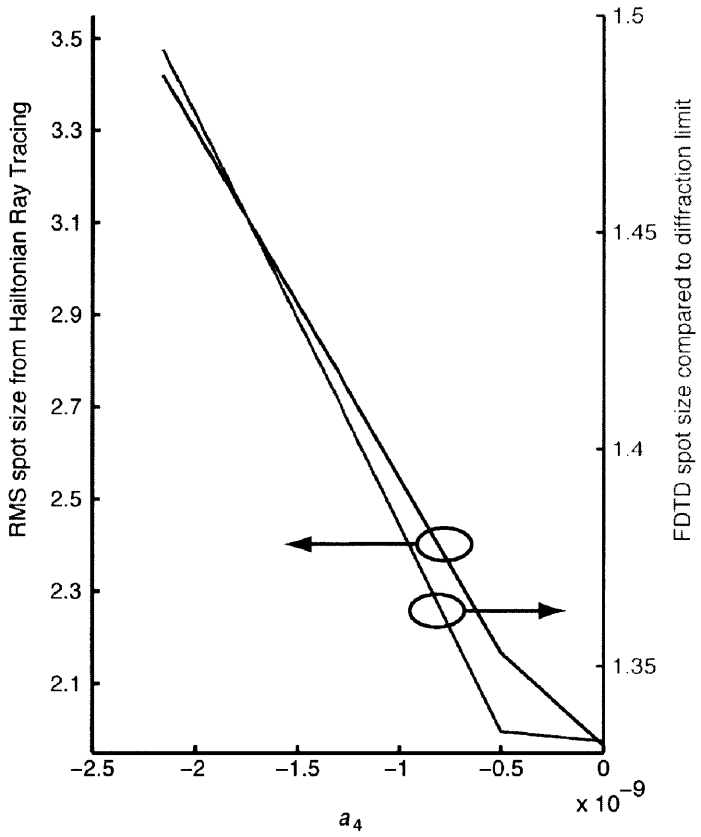

Figure 3.2.4: Comparison of RMS spot size from Hamiltonian Optics and FDTD spot size as a function of the parameter a_4.

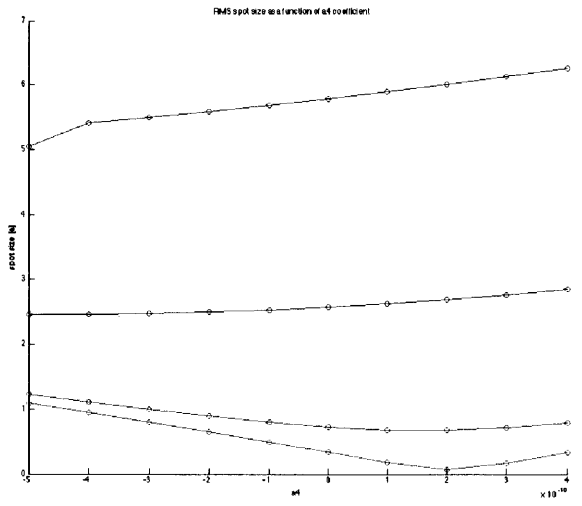

Figure 3.2.5: Equi-frequency contours at various lateral lattice spacing with same rod radius (a), and various radius with same lattice spacing (b).

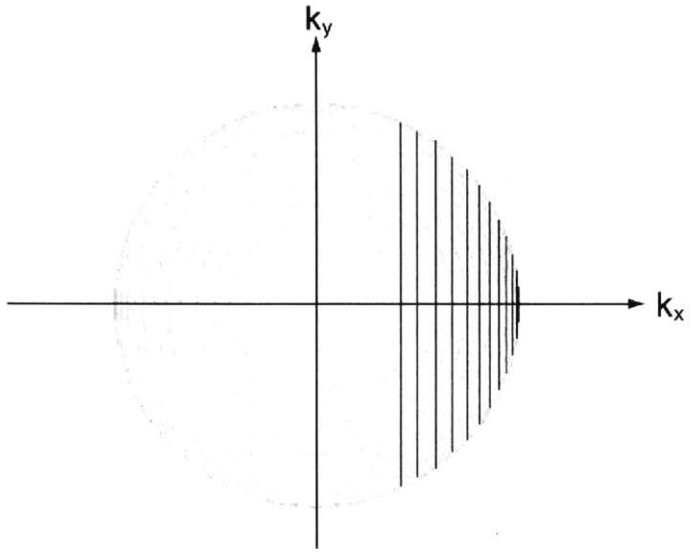

Figure 3.2.6: Equi-frequency contours at various lateral lattice spacing with same rod radius (a), and various radius with same lattice spacing (b).

3.2.1 Phase Space Representation

Figure 3.2.6 shows the k-space plot of the ray trajectories along a rod lens structure described by equation 3.2.1. Each line corresponds to a single ray, where the rays starting closest to the edge of the structure experience the largest variation in k_y. Note that k_x does not vary for each ray, since the periodicity is infinitely symmetric in x.

Figure 3.2.7 shows the effective index n_{eff} seen by the rays as a function of the radial (x-) axis of the GRIN structure. Note that each ray "sees" a different index distribution along its propagation, depending on its initial position when it enters the structure.

3.3 Design and Fabrication of Luneburg Structures

We have extensively investigated on the design and fabrication of a Luneburg lens at optical frequencies using aperiodic photonic nanostructures.

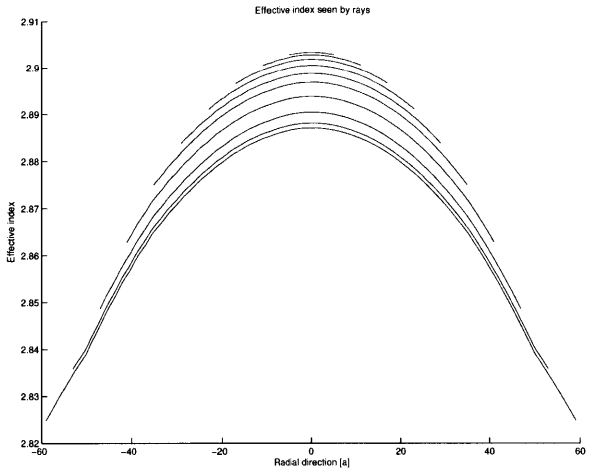

Figure 3.2.7: Local index of refraction seen by each ray, corresponding to each curve, propagating as shown in Figure 3.2.1, plotted along the radial direction.

3.3.1 Luneburg Lens

A Luneburg lens is a lens that has capabilities to focus an incoming plane wave from any incident angle to a diffraction-limited point on the edge at the other side of the lens (Figure 3.3.1). Originally, it was proposed by Rudolf Karl Luneburg in 1944 [48] as a lens with an index distribution where parallel rays converge to a diffraction limited spot at the edge of the lens. The index distribution obtained by Luneburg was $n(r) = n_0\sqrt{2-(r/R)^2}$, where R is the radius of the lens, n_0 is the index of the surrounding medium, and r is the position in the radial direction. Note that the index distribution is spherically symmetric, hence a focus forms on the surface of the lens regardless of the direction of the incoming plane wave. Since Luneburg, there have been numerous attempts to apply this to microwaves as antennas [19, 33, 61, 17], where the index distribution is implemented either as multiple shells with varying density, or with metamaterials [57]. However, it has been difficult to implement the device especially in optical frequencies despite its unique and useful properties due to the difficulty in producing the required gradient index profile. In this Section, the design and fabrication of a Luneburg lens for operation at near infrared optical frequencies is described.

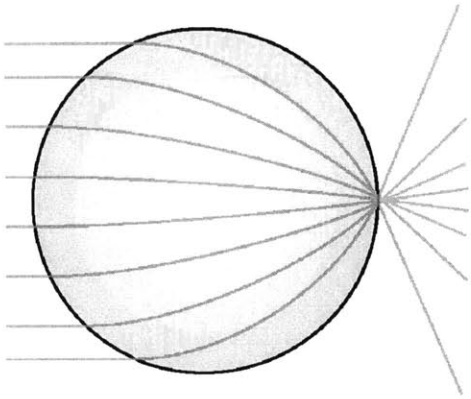

Figure 3.3.1: Schematic illustration of ray propagation through a Luneburg lens. A plane wave incident to the lens forms a focus at the opposite edge of the lens.

3.3.2 Design of Aperiodic Luneburg Lens

Similarly to the method used for the rod lenses, a square lattice of silicon rods with varying diameter are designed through Hamiltonian Optics in order to materialize a Luneburg lens in the optical frequencies.

In order to obtain the effective index distribution that defines the Luneburg lens, first, the relationship between the lattice parameter (in this case, the rod radius) and the effective index is established. This can be done through the library of dispersion diagrams, by investigating the relationship between the lattice parameter and effective index for a given frequency. As discussed earlier, since the effective index varies in direction, two extrema, which are along the edges of the first Brillouin zone, are taken.

After the relationship between the effective index and lattice parameter is determined through either taking one of the extrema or an average, for example, the structure can be further optimized to correct for the angular dependence of the effective index. Then, this relationship can be implemented into the Hamiltonian ray tracing to obtain a structure with intended effective index profile.

The example structure that we discuss here is as shown in Figure 3.3.2. The radii of the rods range from 0.27a to 0.42a, where a is the lattice constant. In Figure 3.3.3, we show the Hamiltonian ray tracing results of this structure overlaid with FDTD analysis results. The green dots depict equal OPL points of the rays, which represent

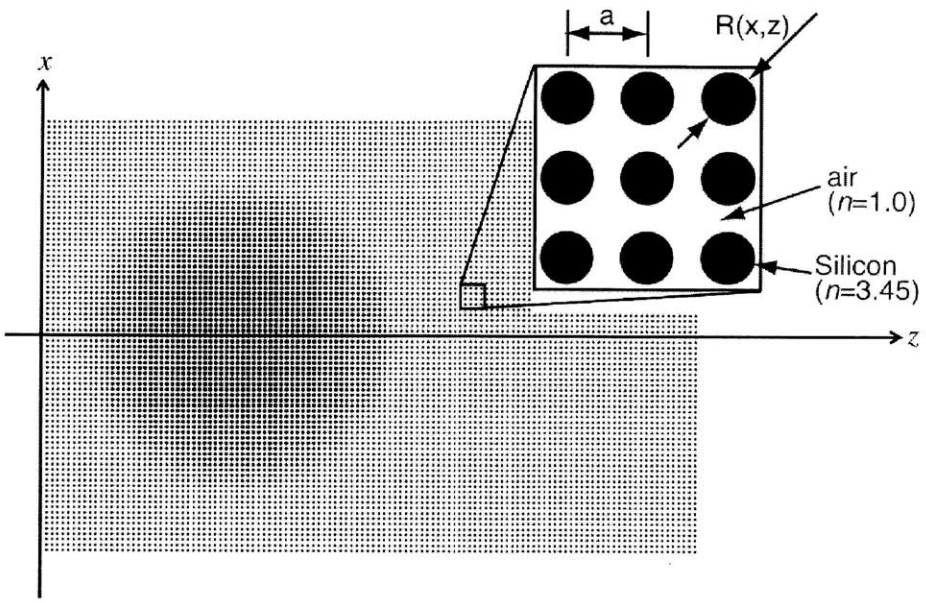

Figure 3.3.2: Geometry of the nanostructured Luneburg lens.

wavefronts when they are connected. It can be seen from the figure that the two results match well, and the wavefront error between the two methods is below $\lambda/8$. Further, it can be seen that the structure focuses a plane wave at the opposite edge, in agreement with the theory for the originally proposed bulk Luneburg lens.

Holes Versus Rods, TE Versus TM Polarization

In terms of the geometry of the lattice, air holes in silicon material (Figure 3.3.4) can be considered as an alternative to the silicon rods in an air lattice. Also, in terms of polarization of the incoming light, TE polarization can be considered instead of the TM polarization that has been used for the simulations above. Here, the two possibilities will be discussed from the point of view of the anisotropy that the structures cause.

Figure 3.3.5 shows the first modes of the dispersion diagrams for TE and TM modes for hole and rod structures with same diameter rods and holes of $r = 0.255a$. The TE mode in rod structures have a noticeably small dispersion, which implies that this mode is least confined to the structures. Figure 3.3.6 shows the same modes for

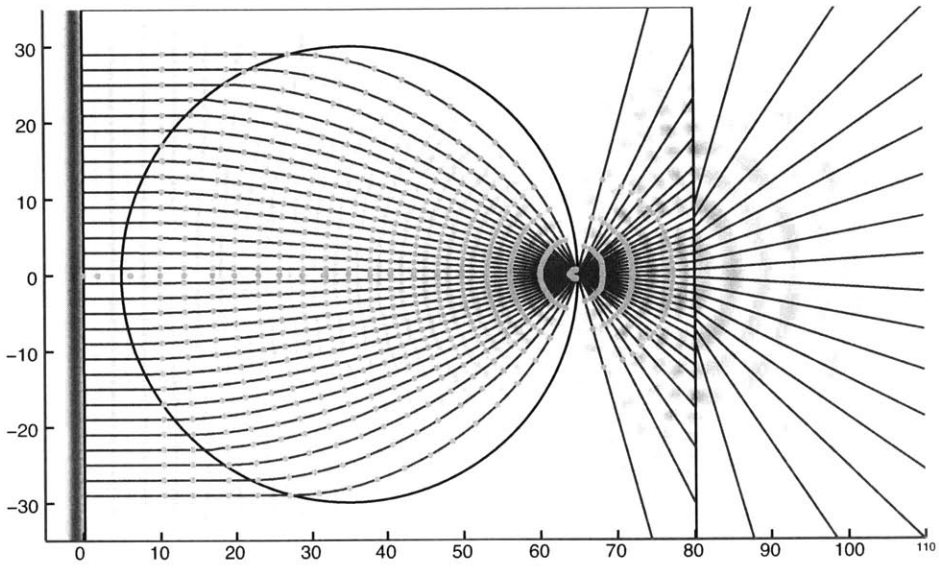

Figure 3.3.3: Hamiltonian ray tracing results (blue lines) overlaid with FDTD analysis (red and blue shading) for the Luneburg structure in Figure 1. The green dots represent equal-OPL points on each ray. It can be seen that the equal-OPL points align well with the wavefronts from the FDTD simulation.

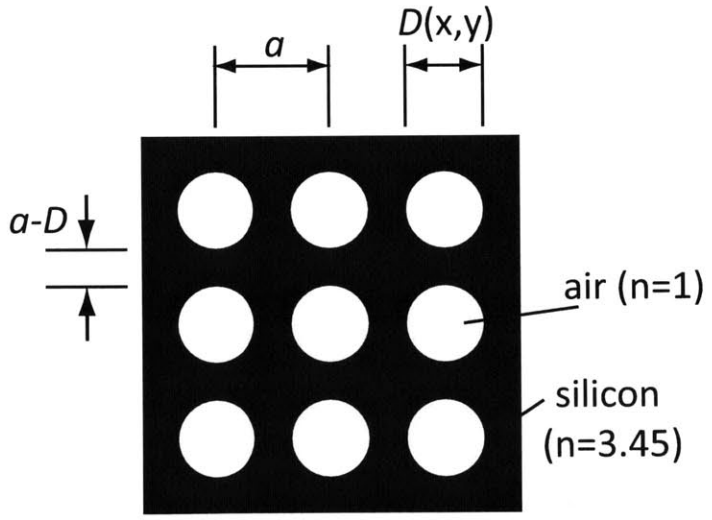

Figure 3.3.4: Schematic illustration of a hole structure in a silicon material.

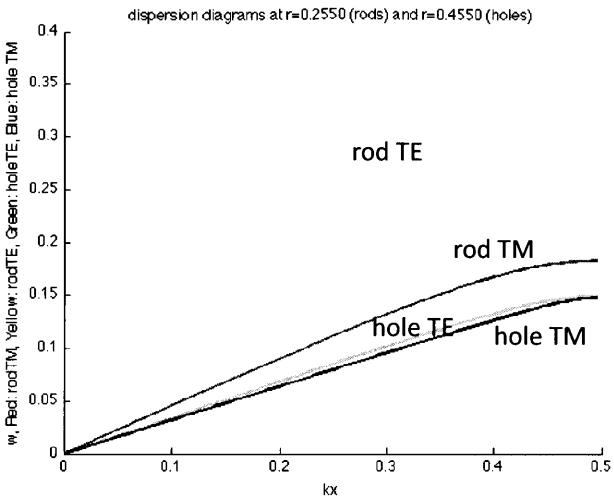

Figure 3.3.5: First mode of the dispersion diagram for TE and TM modes in 2D rod and hole structures for a rod/hole radii of $r = 0.255$.

a "complementary" rod and hole structure pair, which is described in Figure 3.3.7. The TM modes for hole and rod overlap almost completely in this configuration. This means that the two structures can be used interchangably for design. This is advantageous when considering lithography and etching processes such as e-beam lithography, where proximity effects can cause types of distortions where the designed rods or holes become connected (through under exposure or over exposure).

By analyzing these band diagrams for a range of rod/hole diameters, we can obtain the characteristics of each configuration in terms of designing the aperiodic structures, and determine which configuration is suitable for our purpose.

Figure ?? shows a plot of the bottom edge of the first bandgap, which is equivalent to the highest frequency that the first mode can propagate for each configuration. Assuming the lattice constant is fixed in terms of the probing wavelength, it is advantageous to work near $r = 0.25$, where the rod/hole diameter is equal to the spacing between them, since the minimum feature/spacing can be kept at maximum. Looking at the figure, it can be seen that the rod structures have more frequency window (the first bandgap at a higher position in ω), hence more suitable for the aperiodic structures since there is more room for effective index variation.

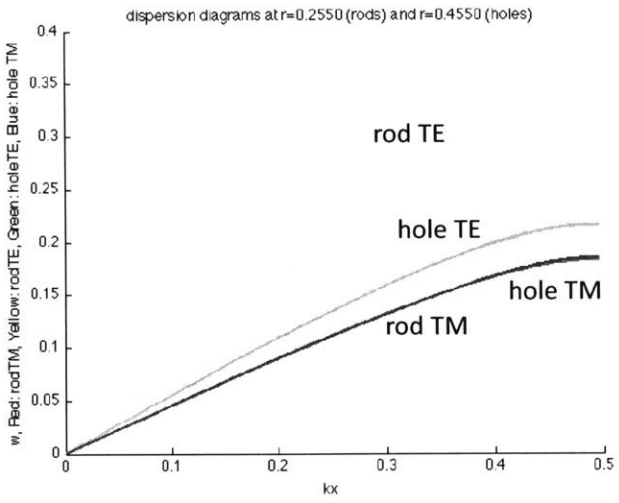

Figure 3.3.6: First mode of the dispersion diagram for TE and TM modes in 2D rod and hole structures for "complementary" rod/hole radii, where $r = 0.255$ for rods and $r = 0.455$ for holes.

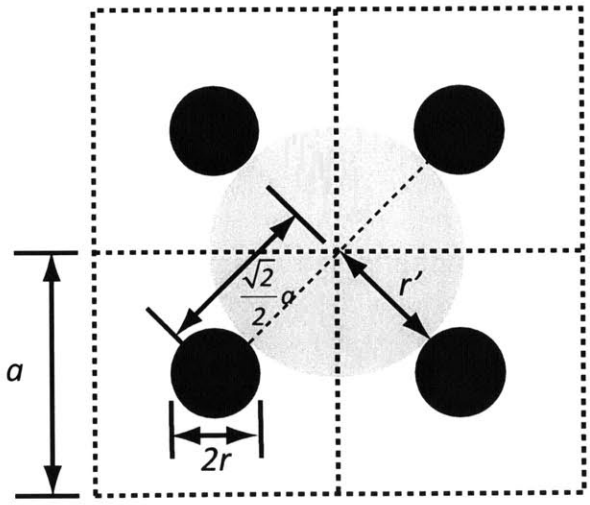

Figure 3.3.7: Schematic illustration of "complementary" rods/holes. The hole has a diameter which covers the maximum possible area between the rods but does not overlap with any of the rods.

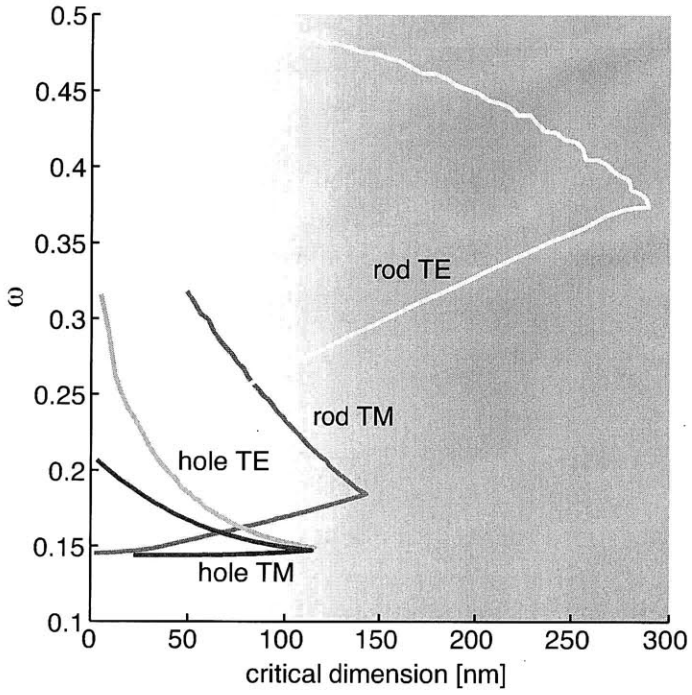

Figure 3.3.8: Plot of the top edge of the first mode of the dispersion diagram for each configuration, as a function of the critical dimension. From the fabrication perspective, it is desirable for the design to be near the right edge of the diagram (darker gray area).

Table 3.3.1: Comparison of fabrication parameters for Luneburg lens designs intended for two different lattice constants. $\lambda = 1.55\mu m$. Note that the minimum feature size (either rod diameter or gap size) is increased from 32nm to 96nm by increasing the lattice constant a.

	$\lambda = 8a$	$\lambda = 6a$
lattice constant	a=193.75nm	a=258.33nm
rod diameter range	$103.1nm < D < 161.78nm$	$96.10nm < D < 150.40nm$
size of gap between rods range	$31.97nm < a - D < 90.68nm$	$107.93nm < a - D < 162.23nm$

Note that, however, this analysis is based on 2D simulations of the structures, hence does not take into account the finite length of the rods or the finite thickness of the slab structure where the holes are fabricated on. The limitations of 3D structures are discussed below.

Fabrication Considerations and 3D Simulation

When considering the fabrication limitations of the Luneburg lens, it is important to have all feature sizes well within the limitations of the e-beam lithography system, and larger feature-size, the structure will exhibit less fabrication error. This means that a larger period size is better in terms of fabrication. However, for a given free-space frequency, as the period becomes larger (*i.e.* as the frequency becomes larger for a given lattice period), nonlinearity and anisotropy of the dispersion diagram becomes larger. Thus, balance must be taken to ensure feasibility of both design and fabrication.

Table 3.3.1 shows a comparison between two Luneburg structures, one designed for wavelength of $\lambda = 8a$, and the other for $\lambda = 6a$. It can be seen that the smallest feature size, which is the gap size between the rods in the case of the former structure and rod diameter in the case of the latter, increases from 31.97nm to 96.10nm. This is due to two effects, namely, the increase in the lattice constant (*i.e.* increase in the overall size of the lattice), and making the duty cycle closer to 1:1.

Thus far, all simulations are conducted in 2D, assuming the fabricated rods are

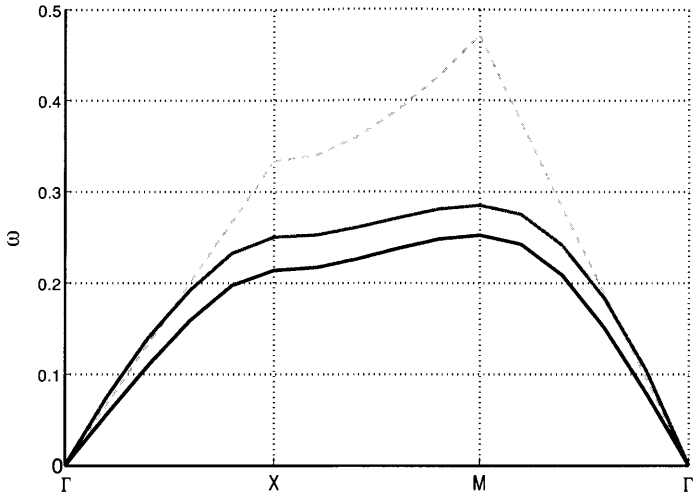

Figure 3.3.9: Dispersion diagram of silicon rods in 2D (blue) and 3D (red). The green light denotes the light line for silicon dioxide, which is underneath the structure. Only the first modes are shown for each structure. Parts of the band in the 3D case are above the dioxide light line, which denotes a leaky mode whereas the band is completely guided in the 2D case.

long enough to be estimated as infinite long. However, the actual device that we fabricated as a proof of concept has a rod length of 320nm, corresponding to $\lambda/5$. Therefore, 3D simulations were conducted to examine the effects of the short rods and the asymmetry of the over- and under-cladding.

Figure 3.3.9 shows 2D and 3D calculations of the dispersion diagram for a lattice with rod radius of $0.25a$ and height of a for the 3D calculation. The inverse of the gradient of the dispersion curves, which correspond to the effective index, is smaller for 3D simulations since it takes into account the mode extending into the air ($n = 1$) region above and the silicon oxide ($n = 1.5$) region below, lowering the effective index seen by the propagating wave.

MPB was used to obtain the dispersion diagram incorporating the 3D structure. A single supercell as shown in Figure 3.3.10 was used to do this calculation. The vertical cell size was adjusted to make sure the top and bottom boundaries, which have Bloch boundary conditions, do not cause artifacts.

By using the dispersion diagrams of the 3D simulated structures, we can redo the Hamiltonian ray tracing. Note that the only modification required is to replace the

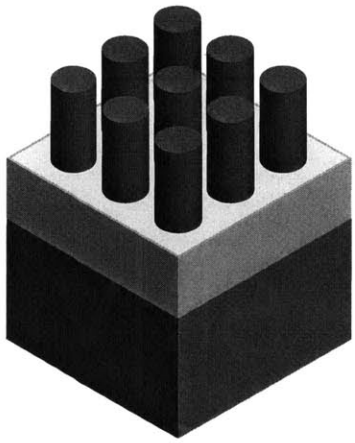

Figure 3.3.10: Schematic of the 3D structure that was used to solve for the dispersion diagram.

library of dispersion diagrams. Note that, however, in order to implement this into the Hamiltonian ray tracing algorithm, it must be made sure that enough sampling points are taken both in the structure and in k-space.

3.3.3 Fabrication

After designing the structure as described above, an actual device has been fabricated for a proof of concept. The overall process flow is as shown in Figure 3.3.11. An SOI wafer with device layer thickness of 340nm and oxide layer thickness of approximately 1μm. After cleaning procedures, the wafer is spin coated with approximately 100nm of hydrogen silsesquioxane (HSQ), which is a negative electron beam resist. HSQ is then exposed with a scanning electron-beam lithography system, followed by a development process using a salty developer [69]. Then, the silicon layer is reacitve-ion etched (RIE) with hydrogen bromide (HBr)-based gas solution.

Care was taken with the electron-beam lithography process in order to avoid unwanted fabrication errors such as proximity effects. Especially since the rod diameter varies between the edges of the structures and the center, dose compensation similar to those discussed in Chapter 2 was incorporated to provide appropriate electron dose for each position on the nanostructure.

Figure 3.3.12 shows a case where the dose at the center region of the lens structure

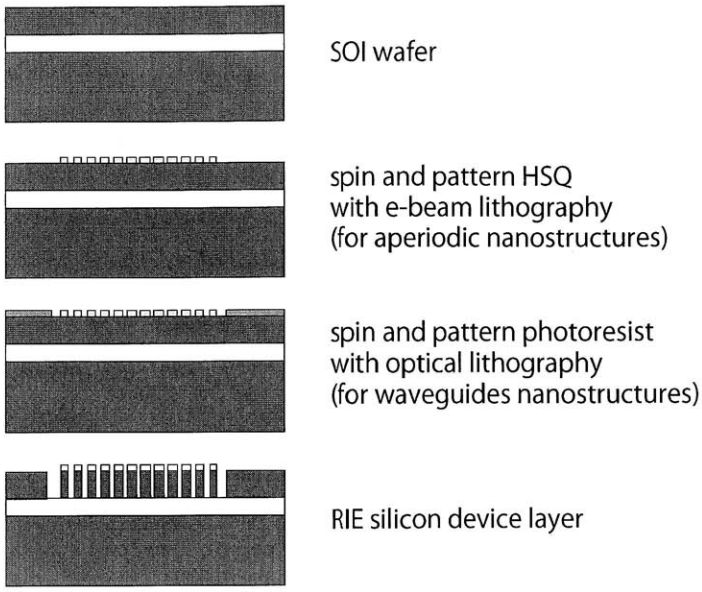

Figure 3.3.11: Fabrication process of the aperiodic nanostructures with waveguides for light coupling.

is excessive, hence the rod structures are connected together. This will cause the effective index at the center of the structure to be larger than designed, and will cause deviations in the ray trajectories which will result in aberrations and shift in the focal point.

Through dose compensation, the structure has been fabricated successfully to have rod features whose diameters are within 2% error from their design (Figure 3.3.13).

In addition to this process, in order to guide light into the structure, waveguides were fabricated onto the substrate as well. This was done with optical lithography using photoresist PFi-88 from Sumitomo Chemical. After developing the HSQ for the nanophotonic structures, the HSQ was annealed to ensure adhesion during the following processes, and then PFi-88 was spin-coated followed by optical lithography. Then, the photoresist was developed using the "salty developer" [69] before RIE. This method was taken instead of writing the waveguides with e-beam lithography along with the nanostructures since the time to write long and wide waveguides with e-beam lithography would be prohibitive.

Specific machines and parameters that were used for the process are shown in

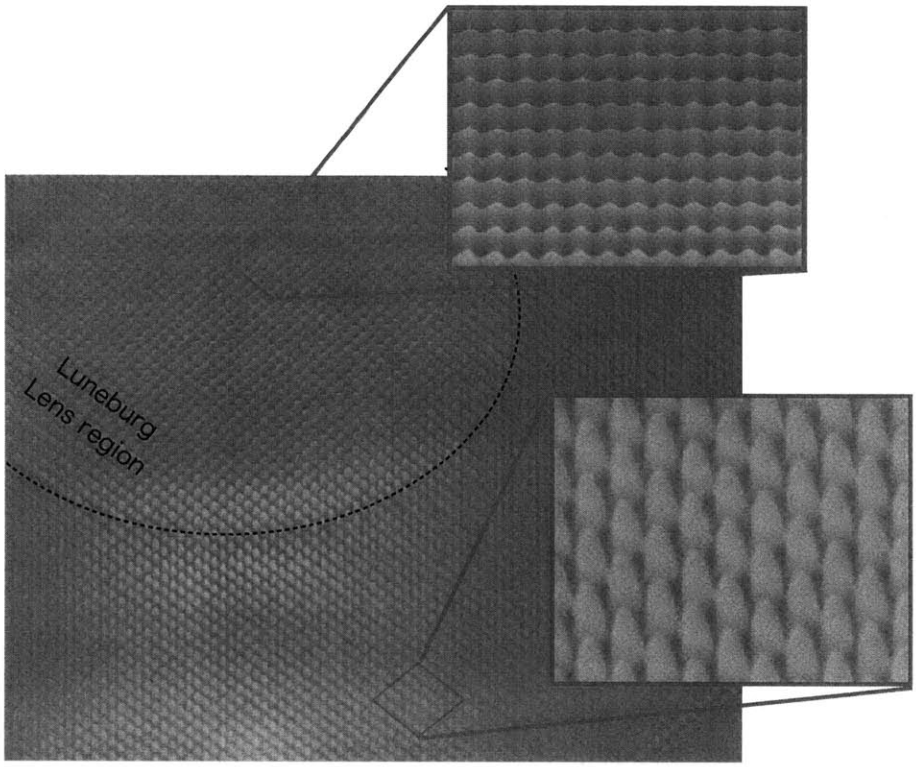

Figure 3.3.12: SEM micrograph of a fabricated Luneburg structure where the center part is attached together as opposed to the designed rods as seen outside of the Luneburg region. This is due to overdose in e-beam lithography at the center, where the structures are much denser. The period of the lattice is 194nm.

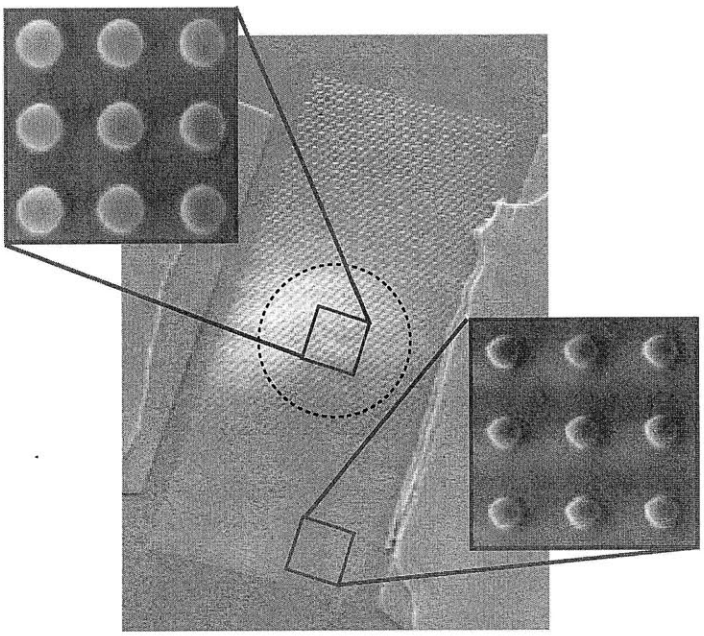

Figure 3.3.13: SEM micrograph of a fabricated Luneburg structure with successful dose compensation. All silicon rods are isolated from each other as opposed to what can be seen in Figure 3.3.12. The period of the lattice is 258nm, and the overall size of the nanostructure region is $50\mu m$ by $20\mu m$. Waveguides for coupling light into the structure can be seen on the left and right of the structure.

Table A.2.1 in Appendix A.

3.3.4 Experiment and Results

The fabricated nanostructured Luneburg was tested to verify its function. A scanning near-field optical microscope (SNOM) was used to measure the intensity distribution across the structure as light was probed in. An SNOM is a technique where near-field light is probed with a probe tip, which is similar to an atomic force microscope (AFM) tip but with a small aperture at the center, and tunneled into a microscope objective, from which the optical signal is propagated into the detecter. With this method, the intensity distribution of the light propagating through the structure can be measured. While some conventional SNOM systems use an optical fiber as a probe to directly extract light from the near field, our setup uses the above-mentioned method since this method has a large advantage of being able to take topological measurements similarly to an AFM at the same time, which is fed back to ensure the position of the probe is at constant distance from the surface when taking near-field optical data, since this distance is critical in obtaining consistent data. The drawback of this method is that the loss along the propagation of the system becomes larger through the multiple optics and coupling and/or reflection at the interface of each component, while the SNOM in general is a highly photon-starving technique. In order to ensure a high enough signal can be obtained above the noise floor, a highly sensitive detector is required, such as a photon multiplier tube (PMT).

Figure 3.3.14 shows a schematic of the experimental setup. A tunable external cavity laser, Tunics-Plus model 3642 HE10 from Photonetics was used as the source at wavelength $\lambda = 1.550\mu m$, guided to the waveguide on the substrate through a single mode fiber (Nanonics, Inc. [12]). The sample is examined through an NSOM system, alpha 300S from WITec [14], where the optical signal is routed to an InGaAs femtowatt photodetector (Thorlabs, PDF10C [13]) from the top of the microscope system. The electronic output from the detector is fed back into the WITec NSOM system, and the FPGA-based WITec controller interprets the signal to output the intensity field.

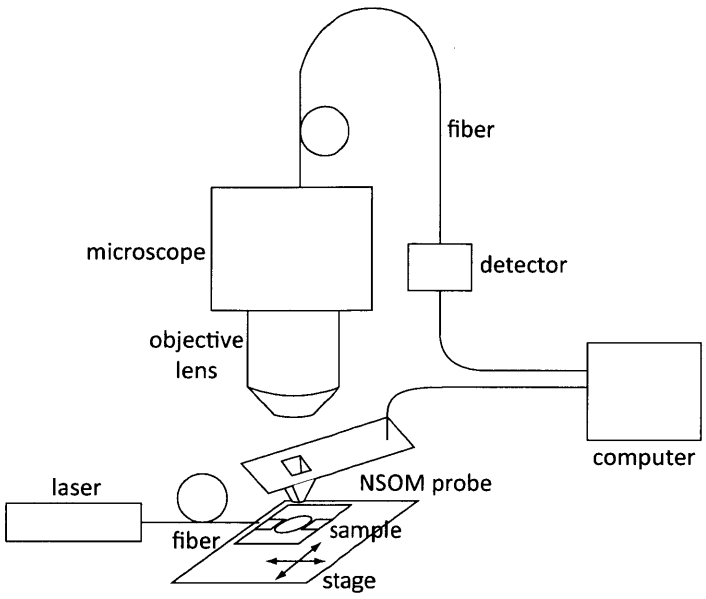

Figure 3.3.14: Schematic illustration of the experimental setup for the Luneburg lens structure using an NSOM.

The default settings of the WITec SNOM system uses a PMT with a silicon detector, but since the spectral range of the detector was not sufficient for our experiment at wavelength of $\lambda = 1.550\mu m$, the femtowatt photodetector was externally attached to the system. While this detector is an inexpensive solution to detect signal from the SNOM system, the detection time is rather slow with a rise-time of approximately 20ms, hence care must be taken in the scan speed, and environment stability is crucial while obtaining large-area data. Figure 3.3.15 shows the time and frequency characteristics of the detector [15]. The minimum noise equivalent power (NEP) at DC for this detector is $7fW/\sqrt{\text{Hz}}$, and the overall output voltage noise is $3.5m\text{V}_{RMS}$.

Figure 3.3.16 shows an NSOM measurement along a waveguide on the substrate leading to the Luneburg structure. Figure 3.3.16 (c) shows a cross-section profile of the intensity inside the waveguide along with a Gaussian showing a full-width at half-maximum (FWHM) measurement of $16.19\mu m$.

Figure 3.3.17 shows an NSOM measurement of the Luneburg Lens, along with a topological measurement taken simultaneously. The IR light is sent from the left side of the image, where the end of the on-chip waveguide is visible. It can be seen

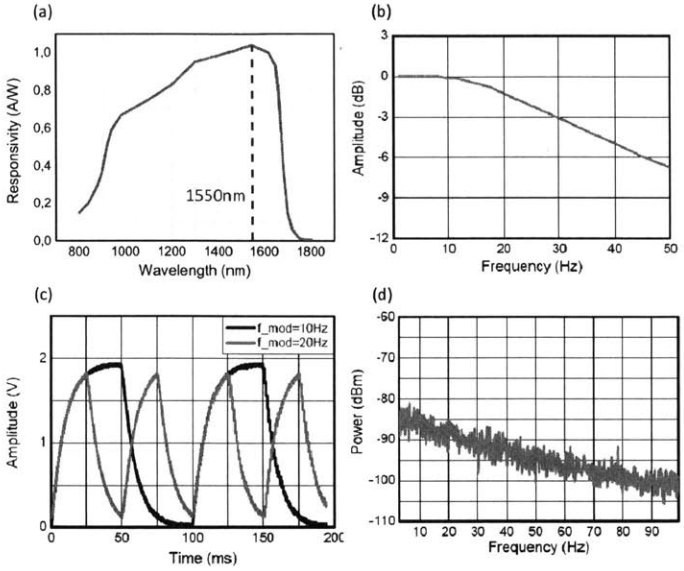

Figure 3.3.15: Characteristics of the infrared detector PDF10C from ThorLabs: (a) responsivity towards wavelengths of light (b) frequency response (c) time response (d) noise spectrum.[15]

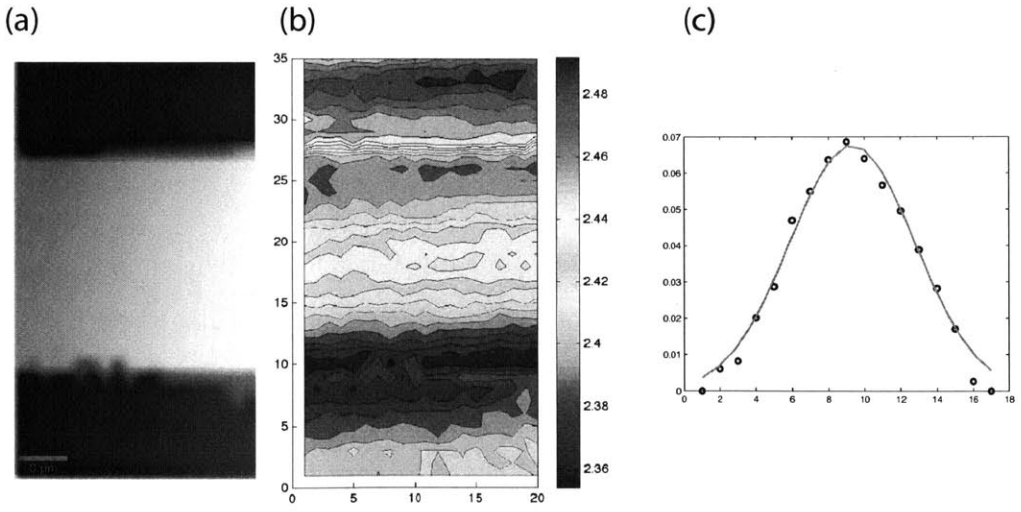

Figure 3.3.16: NSOM measurement along a waveguide leading to the Luneburg structure. (a) shows the profile measurement, the center yellow part showing the waveguide which is 320nm high from the substrate. (b) shows the intensity plot taken from the NSOM. (c) shows a plot of intensity at a cross-section, fitted with a Gaussian profile (red line). FWHM of the Gaussian profile is 16.19μm.

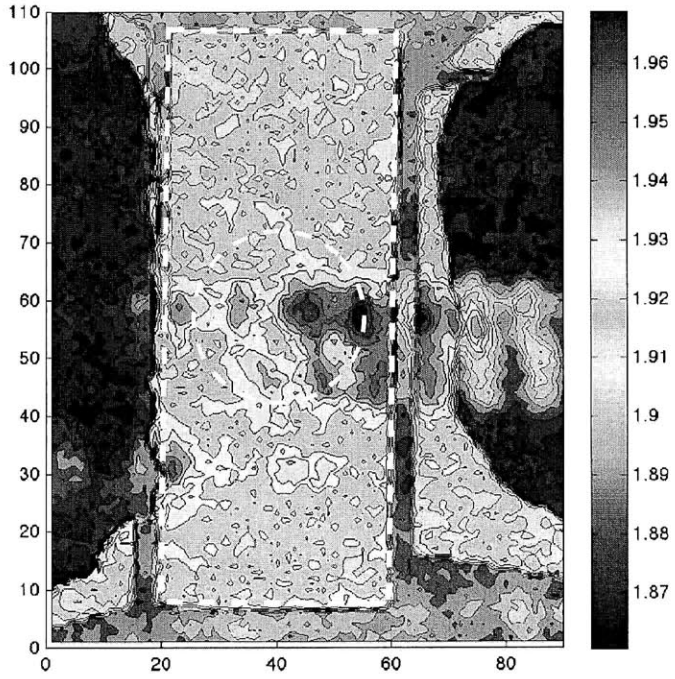

Figure 3.3.17: NSOM measurement of the Luneburg structure with $\lambda = 1.55\mu m$ laser beam probed from the left hand side of the figure. The focus at the right edge of the Luneburg structure, outlined with white dotted line, is evident.

that there is a high-intensity spot at the edge of the Luneburg Lens structure, which corresponds to the focus. Figure 3.3.18 shows the intensity cross-section across the focal point. The FWHM is $10.18\mu m$, confirming focusing of the beam. Note that the focus is slightly off from the edge of the Luneburg lens, and also the focal spot is highly aberrated, which are due to fabrication imperfections and light source being not an ideal plane wave.

Further, the structure was probed at an angle of 45 degrees. Figure 3.3.19 Shows the SNOM measurement of the intensity distribution in the structure. It can be seen that the focus further shifts away from the edge of the Luneburg region. This is due to the innate anisotropy of the structures shifting the effective index of the structures. Nonetheless, it can be seen that the incoming beam forms a focus around 5.5 μm after the edge of the structure, whose spot profile is as shown in Figure 3.3.20. The

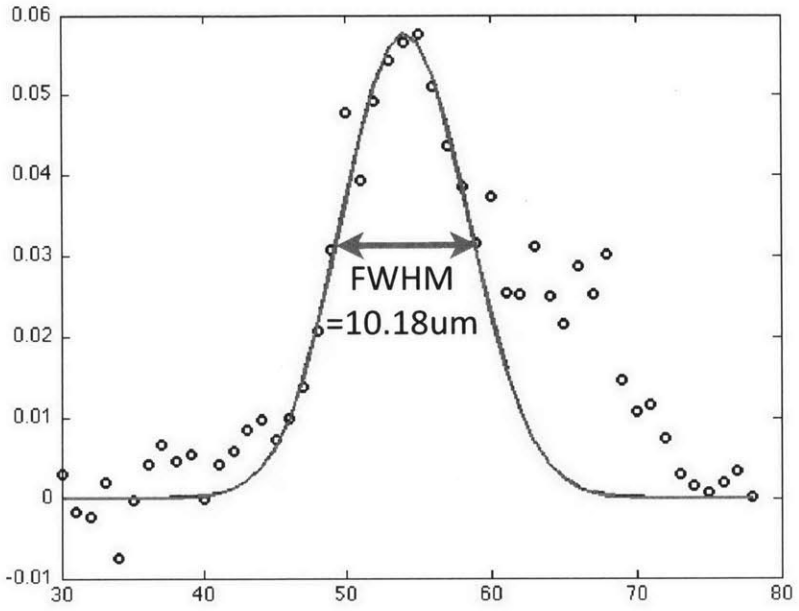

Figure 3.3.18: Intensity cross-section at focus of the Luneburg structure. The FWHM is around $10\mu m$

FWHM of the spot is $3.48\mu m$, with a Gaussian fit of the data.

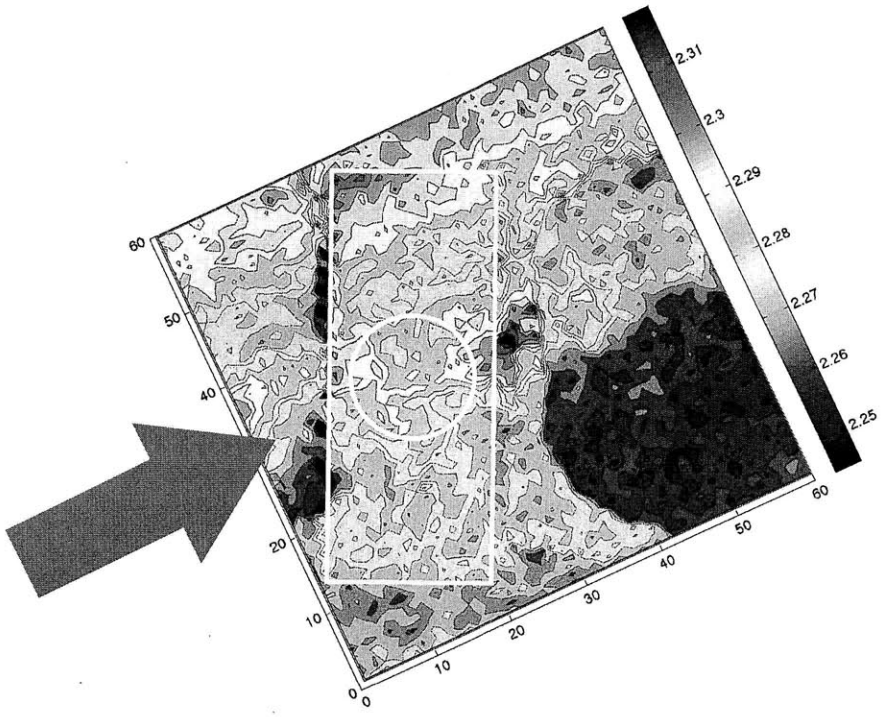

Figure 3.3.19: NSOM measurement of the Luneburg structure with $\lambda = 1.55\mu m$ laser beam probed from the left hand side of the figure. The The focus at the right edge of the Luneburg structure, outlined with white dotted line, is evident.

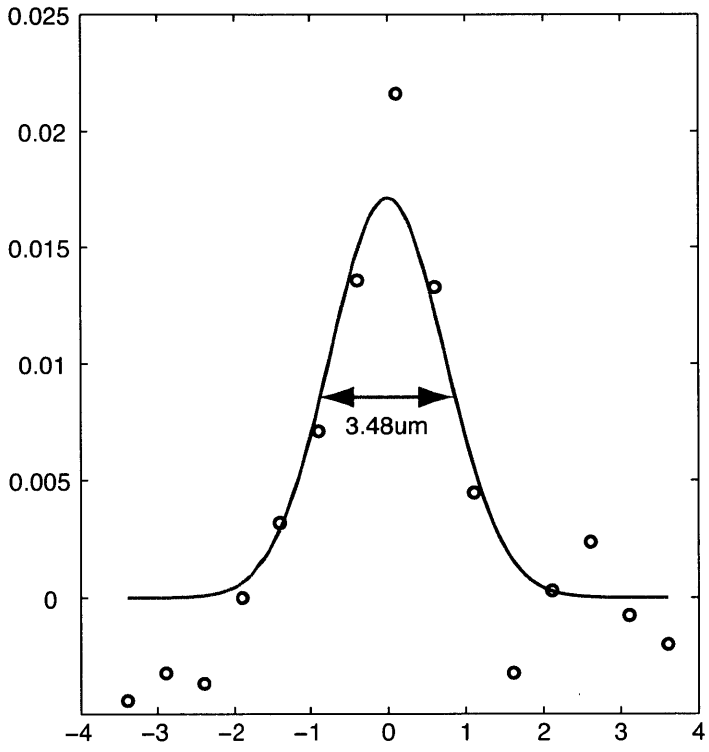

Figure 3.3.20: Intensity cross-section at focus of the Luneburg structure when probed from 45 degrees. The FWHM is around 3.48 μm

Chapter 4

Conclusion and Future Work

In this thesis, design and fabrication of micro- and nano-photonic structures have been discussed. Particularly, optical systems with diffractive elements for application in LCD manufacturing and repair have been designed and experimentally verified. Particularly, the challenges with fabrication of the phase elements have been addressed, in coordination with the design of the element and the overall system. In the CGH lithography system, the reconstructed image was analyzed to reveal high correlation with the design. The exposed resist was successfully developed for a design with feature sizes of hundreds of microns. In the blazed grating matrix, blazed-profile gratings were fabricated using gray scale lithography, and showed controlled ablation of metal and photoresist, as well as control of multiple ablation spots. In the sub-wavelength regime, rod lens and Luneburg lens structures were designed with adiabatic nanostructures using Hamiltonian ray tracing. Aberration correction was shown in rod lenses, and a Luneburg structure was fabricated and optically tested.

4.1 Future Work

Research work described in this thesis has opened up further questions and ideas to be investigated upon. This section will describe a few paths this research can expand as future work.

4.1.1 CGH Lithography

In this research, we investigated binary phase CGHs. However, if we loosen the constraint to multilevel CGHs, larger amounts of information can be encoded into the CGH, resulting in higher contrast, less noise, or capabilities of multiplexing.

Also, designing the depth of focus is important when it is desired to only ablate a specific depth layer. This can be done by including the depth of focus as a constraint in the optimization.

Further, feasibility of multispectral CGH design to reconstruct two different patterns can be investigated, such as the gate and reflection patterns, from the same CGH when probed by plane waves with different operating wavelengths.

4.1.2 Multispot Ablation

Flat-top beam profile generation

When a Gaussian profile coherent beam is used for the ablation, the intensity profile at the substrate of ablation will become Gaussian, with addition of aberration from the optical system. Usually, a flat-top intensity profile is preferred for these applications in order to get uniform intensity across the region of ablation. Hence, beam shaping of the Gaussian profile into a flat-top profile is desirable.

Beam profile modification, especially from Gaussian to flat-top, has been investigated in the past. Further work is desirable to produce a range of spot sizes so that it can be tuned according to the required ablation area geometry and dimensions.

4.1.3 Aperiodic Nanostructures

Fabrication of 3D Structures

In many applications, 3D optical components capable of manipulation of ray propagation in all three spatial dimensions are more desirable than the 2D device that has been fabricated and tested for proof of concept. Since the Hamiltonian design method is valid for 3D structures as well, as long as the 3D dispersion diagrams (the

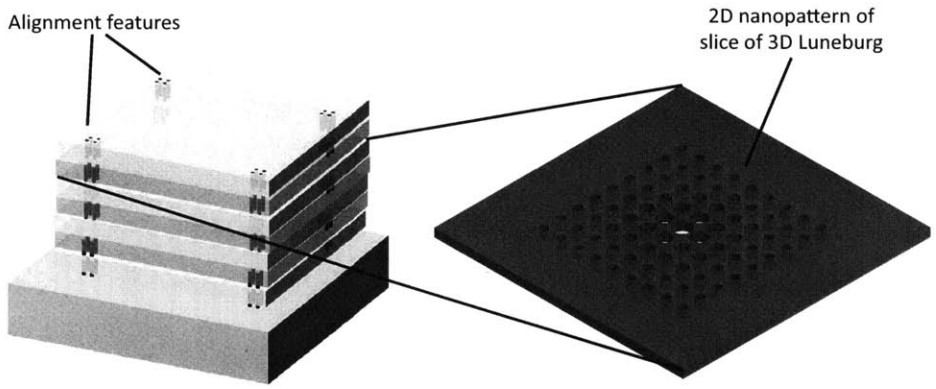

Figure 4.1.1: Schematic illustration of a 3D Luneburg lens fabricated through stacking of 2D features generated by fabrication methods such as e-beam lithography.

dispersion hyperplanes) are calculated and stored as libraries. In fact, the advantage of low computational power becomes more significant for 3D structures compared to finite difference methods where the full 3D volume must be calculated at every step. Therefore, the ability to materialize a 3D aperiodic structures depends solely on fabrication capabilities. The nature of these structures being in tens to hundreds of nanometers for optical frequencies, as well as being non-periodic makes 3D fabrication a significant challenge.

There has been several works on 3D nanostructure fabrication, such as those introduced in Chapter 1. These techniques can be applied to fabrication of 3D nanostructured Luneburg lenses. For example, femtosecond laser micromachining techniques can be used to directly write the structures into a transparent material [31]. Another possibility of an implementation of a 3D Luneburg lens is shown in Figure 4.1.1,where multiple layers of nanostructures are stacked together to form a 3D Luneburg lens, using a similar technique as described in [43, 54]. The advantage of this technique is that 2D fabrication techniques (such as what is shown in Chapter 3) can be utilized and directly extended to create a 3D device.

Investigation into Anisotropy

In this work, we have designed our structures so that the effects of the inherent anisotropy of the subwavelength structures are kept to minimum. However, this

anisotropy can be explored to be a useful feature instead. Figure 3.1.2 shows a dispersion diagram of a rectangular lattice with different lattice constants in x and y. It can be seen that the dispersion is not symmetric in x and y anymore, and therefore this structure has different effective index in the two directions, *i.e.*, birefringence.

Some work has been done with so-called form birefringence, where sub-wavelength structures are incorporated to generate birefringence artificially [29], but this phenomenon can be extended to design of an artificial anisotropic inhomogeneous media. These types of material can be used to design an optical cloak, for example. As shown in works by Pendry [37], cloaks require anisotropic inhomogeneous media through design by conformal mapping. Smith *et al.* use quasi-conformal mapping in order to facilitate the fabrication [58], but this causes effects that are not desirable for cloaking, such as shift in the ray trajectory that could reveal the cloak. This problem can be alleviated through design of anisotropy with aperiodic structures as shown in Chapter 3.

Appendix A

Fabrication Processes

All fabrication of optical components were conducted in the Microsystems Technology Lab (MTL), the Nano Structure Laboratory (NSL), and Scanning Electron Beam Lithography (SEBL) facility at the Massachusetts Institute of Technology (MIT).

Here, the detailed fabrication processes of each components will be described.

A.1 Fabrication Process of the Computer Generated Hologram

The fabrication process in Table A.1.1 was conducted on a 4-inch fused silica wafer.

Table A.1.1: Fabrication Process of the CGH described in Chapter 2. The machine column refers to the machine that has been used in the Nanostructure Laboratory (NSL) at MIT unless otherwise noted.

Step	Description	Recipe	Machine
1	RCA clean		acid hood
2	spin HSQ		spinner
3	evaporate Al	3 - 5nm	e-beam evaporator (MTL EML[1])
4	e-beam pattern		Raith 150 (SEBL[2])
5	develop	NaOH + NaCl[69]	wet bench
6	rinse and dry		wet bench

A.2 Fabrication Process of the Blazed Grating Matrix

The fabrication process in Table A.2.1 was conducted on a 4-inch fused silica wafer.

Table A.2.1: Fabrication Process of the aperiodic Luneburg lens described in Chapter 3. The machine column refers to the machine that has been used in the Nanostructure Laboratory (NSL) at MIT unless otherwise noted.

Step	Description	Recipe	Machine
1	RCA clean		acid hood
2	HMDS		HMDS oven
3	spin resist	OCG825-20 $1\mu m$	spinner
4	prebake	20min, 90 °C	oven
5	expose		EV1
6	develop	OCG934 1:1	solvent hood
7	rinse and dry		solvent hood
8	postbake	2hrs, 90 °C	oven
9	RIE	CF4 + O2	wet bench
10	ash		asher

A.3 Fabrication Process of the Aperiodic Nanostructures

Table A.3.1: Fabrication Process of the blazed grating matrix described in Chapter 2. The machine column refers to the machine that has been used in the Microstructures Technology Laboratory (MTL).

Step	**Description**	**Recipe**	**Machine**
1	RCA clean		acid hood
2	spin HSQ		spinner
3	evaporate Al	3 - 5nm	e-beam evaporator (MTL EML)
4	e-beam pattern		Raith 150 (SEBL)
5	develop	NaOH + NaCl[69]	wet bench
6	rinse and dry		wet bench
7	spin resist	PFi-88	spinner
8	bake	90 sec	hot plate
9	expose	waveguide pattern	OAI
10	develop	CD-26	wet bench
11	rinse and dry		wet bench

Bibliography

[1] PhD thesis.

[2] http://ab-initio.mit.edu/wiki/index.php/meep. On Web.

[3] http://canyonmaterials.com/. On Web.

[4] http://photonix.com/. On Web.

[5] http://www.advancerepro.com/index.htm/. On Web.

[6] http://www.bostonmicromachines.com/deformable-mirrors.htm. On Web.

[7] http://www.dlp.com/. On Web.

[8] http://www.dowcorning.com/. On Web.

[9] http://www.holoeye.com/. On Web.

[10] http://www.lumerical.com/. On Web.

[11] http://www.mitutoyo.co.jp/. On Web.

[12] http://www.nanonics.co.il/. On Web.

[13] http://www.thorlabs.com/. On Web.

[14] http://www.witec-instruments.com/en/products/snom/alpha300s/. On Web.

[15] Operation manual thorlabs instrumentation pdf10x series femtowatt photoreceivers pdf10a pdf10c.

[16] Personal conversation with james sungjin lee.

[17] J. S. Kot A. J. Parfitt and G. L. James. The luneburg lens as a radio telescope element. *Antennas and Propagation Society International Symposium, 2000. IEEE*, 1:170, 2000.

[18] T. Shih A. Sinha, W. Sun and G. Barbastathis. Volume holographic imaging in transmission geometry. *Appl. Opt.*, 43:1533, 2004.

[19] J. P. Ebling G. V. Eleftheriades B. Schoenlinner, W. Xidong and G. M. Rebeiz. Wide-scan spherical-lens antennas for automotive radars. *Microwave Theory and Techniques, IEEE Transactions on*, 50:2166, 2002.

[20] T. Baba. Slow light in photonic crystals. *Nature Photon.*, 2:465, 2008.

[21] M. Born and E. Wolf. *Principles of Optics: Electromagnetic Theory of Propagation, Interference and Diffraction of Light.* Cambridge University Press, 1999.

[22] B. R. Brown and A. W. Lohmann. Complex spatial filtering with binary masks. *Appl. Opt.*, 5:967, 1966.

[23] et al. C. D. Carey. Computer-generated hologram etched in gaas for optical interconnection of vlsi circuits. *Elec. Lett.*, 28:22, 1992.

[24] C. Caratheodory. *Geometrische Optik.* Springer, 1937.

[25] J. A. Dominguez-Caballero. *Optimization of the Holographic Process for Imaging and Lithography.* PhD thesis, Massachusetts Institute of Technology, Cambridge, MA, 2010.

[26] E. Ozbay S. Foteinopoulou E. Cubukcu, K. Aydin and C. M. Soukoulis. Electromagnetic waves: Negative refraction by photonic crystals. *Nature*, 423:604, 2003.

[27] J. D. Joannopoulos et al. *Photonic Crystals Molding the Flow of Light Second Edition.* Princeton, second edition, 2008.

[28] S. Bhling A. J. M. Nellissen L. Wang F. Wyrowski, E.B. Kley and M. Dirkzwager. Proximity printing by wave-optically designed masks. *Nature Photon.*, 4436:130, 2001.

[29] P.-C Sun Y. Fainman C.-C. Cheng F. Xu, R.-C. Tyan and A. Scherer. Fabrication, modeling, and characterization of form-birefringent nanostructures. *Opt. Lett.*, 20:2457, 1995.

[30] D. Gabor. A new microscopic principle. *Nature*, 161:777, 1948.

[31] R. R. Gattass and E. Mazur. Femtosecond laser micromachining in transparent materials. *Nature Photon.*, 2:219, 2008.

[32] D. Gil. *Maskless nanolithography and imaging with diffractive optical arrays.* PhD thesis, Massachusetts Institute of Technology, Cambridge, MA, 2003.

[33] L. C. Gunderson and G. T. Holmes. Microwave luneburg lens. *Applied Optics*, 7:801, 1968.

[34] S. Matsuo H.-B. Sun and M. Hiroaki. Three-dimensional photonic crystal structures achieved with two-photon-absorption photopolymerization of resin. *Appl. Phys. Lett.*, 74:786, 1999.

[35] Hecht. *Optics Fourth Edition.* Pearson Education, fourth edition, 2002.

[36] et al I. B. Baek. Electron beam lithography patterning of sub-10nm line using hydrogen silsesquioxane for nanoscale device applications. *J. Vac. Sci. Technol. B*, 23:3120, 2005.

[37] D. Schurig J. B. Pendry and D. R. Smith. Controlling electromagnetic fields. *Science*, 312:1780, 2006.

[38] T. Haist J. Liesener, M. Reicherter and H. J. Tiziani. Multi-functional optical tweezers using computer-generated holograms. *Opt. Comm.*, 185:77, 2000.

[39] R. J. Perlmutter J. R. Freyer and J. W. Goodman. Digital holography: Algorithms, e-beam lithography, and 3-d display. *Proc. Soc. Photo-Opt. Instrum. Eng.*, 437:38, 1983.

[40] et al. J. Salo. Millimeter-wave bessel beams using computer holograms. *Elec. Lett.*, 37:13, 2001.

[41] T. Zentgraf-G. Bartal J. Valentine, J. Li and X. Zhang. An optical cloak made of dielectrics. *Nat. Materials*, 8:568, 2009.

[42] C. Jacobsen and M. Howells. Projection x-ray lithography using computer-generated holograms: A study of compatibility with proximity lithography. *J. Vac. Sci. Technol. B*, 10:6, 1992.

[43] M. Nishioka-M. Nomura S. Iwamoto K. Aoki, D. Guimard and Y. Arakawa. Coupling of quantum-dot light emission with a three-dimensional photonic-crystal nanocavity. *Nature Photon.*, 2:688, 2008.

[44] J. P. Kirk and A. L. Jones. Phase-only complex-valued spatial filter. *JOSA*, 61:8, 1971.

[45] S. Matsuo-S. Juodkazis K.?K. Seet, V. Mizeikis and H. Misawa. Three-dimensional spiral-architecture photonic crystals obtained by direct laser writing. *Adv. Mater.*, 17:541, 2005.

[46] P. Lalanne and J. P. Hugonin. High-order effective-medium theory of subwavelength gratings in classical mounting: application to volume holograms. *J. Opt. Soc. Am. A*, 15:1843, 1998.

[47] U. Leonhardt. Optical conformal mapping. *Science*, 312:1777, 2006.

[48] R. K. Luneburg. *Mathematical theory of optics.* University of California Press, 1964.

[49] M. T. Harrison R. G. Denning M. Campbell, D. N. Sharp and A. J. Turberfield. Fabrication of photonic crystals for the visible spectrum by holographic lithography. *Nature*, 404:1982, 1999.

[50] A. Shinya J. Takahashi C. Takahashi M. Notomi, K. Yamada and I. Yokohama. Extremely large group-velocity dispersion of line-defect waveguides in photonic crystal slabs. *Phys. Rev. Lett.*, 87:253902, 2001.

[51] P. T. Rakich S. G. Johnson J. D. Joannopoulos E. P. Ippen M. Qi, E. Lidorikis and H. I. Smith. A three-dimensional optical photonic crystal with designed point defects. *Nature*, 429:538, 2004.

[52] et al. M. Shigeki. Proximity-effect correction software for epl using the pattern classify method. *Proc. of SPIE*, 5446:897, 2004.

[53] D. T. Moore. Design of singlets with continuously varying indices of refraction. *J. Opt. Soc. Am.*, 61:886, 1971.

[54] A. J. Nichol and G. Barbastathis. Sub-30nm alignment accuracy between layered photonic nanostructures using optimized nanomagnet arrays. In *Optical MEMs and Nanophotonics, 2008 IEEE/LEOS International Conference on*, page 9, August 2008.

[55] S. Tandon M. Ibanescu M. Soljacic G. S. Petrich J. D. Joannopoulos L. A. Kolodziejski P. T. Rakich, M. S. Dahlem and E. P. Ippen. Achieving centimetre-scale supercollimation in a large-area two-dimensional photonic crystal. *Nature Mat.*, 5:96, 2003.

[56] D. Psaltis and G.W. Burr. Holographic data storage. *Computer*, 31:52, 1998.

[57] H. F. Ma Q. Cheng and T. J. Cui. Broadband planar luneburg lens based on complementary metamaterials. *Applied Physics Letters*, 95:181901, 2009.

[58] J. J. Mock J. Y. Chin T. J. Cui R. Liu, C. Ji and D. R. Smith. Broadband ground-plane cloak. *Science*, 323:366, 2009.

[59] P. S. J. Russell and T. A. Birks. Hamiltonian optics of nonuniform photonic crystals. *J. Lightwave Technol.*, 17:1982, 1999.

[60] M. A. Skorobogatiy M. Ibanescu E. Lidorikis S. G. Johnson, P. Bienstman and J. D. Joannopoulos. Adiabatic theorum and continuous coupled-mode theory for efficient taper transitions in photonic crystals. *Phys. Rev. Lett.*, 70:036612, 2004.

[61] M. Himdi S. Rondineau and J.Sorieux. A sliced spherical luneburg lens. *Antennas and Wireless Propagation Letters, IEEE*, 2:163, 2003.

[62] P. R. Krauss S. Y. Chou and P. J. Renstrom. Imprint of sub?25 nm vias and trenches in polymers. *Appl. Phys. Lett.*, 67:3114, 1995.

[63] K. Sakoda. *Optical Properties of Photonic Crystals 2nd Edition.* Springer, 2005.

[64] P. Brenner J. B. Pendry T. Ergin, N. Stenger and M. Wegener. Three-dimensional invisibility cloak at optical wavelengths. *Science*, 16:337, 2010.

[65] K. B. Wolf. *Geometric Optics on Phase Space.* Springer, 2004.

[66] S. Fan Y. Jiao and D. A. B. Miller. Designing for beam propagation in periodic and nonperiodic photonic nanostructures: Extended hamiltonian method. *IEEE J. Quantum Electron*, 70:036612, 1999.

[67] B. Gates Y. Xia and Z.-Y. Li. Self-assembly approaches to three-dimensional photonic crystals. *Adv. Mater.*, 13:409, 2001.

[68] E. Yablonovitch. Inhibited spontaneous emission in solid-state physics and electronics. *Phys. Rev. Lett*, 58:2059, 1987.

[69] J. K. W. Yang and K. K. Berggren. Using high-contrast salty development of hydrogen silsesquioxane for sub-10?nm half-pitch lithography. *J. Vac. Sci. Technol. B*, 25:2025, 2007.

[71] K. B. Wolf. *Geometric Optics on Phase Space.* Springer, 2004.

[72] S. Fan Y. Jiao and D. A. B. Miller. Designing for beam propagation in periodic and nonperiodic photonic nanostructures: Extended hamiltonian method. *IEEE J. Quantum Electron*, 70:036612, 1999.

[73] B. Gates Y. Xia and Z.-Y. Li. Self-assembly approaches to three-dimensional photonic crystals. *Adv. Mater.*, 13:409, 2001.

[74] E. Yablonovitch. Inhibited spontaneous emission in solid-state physics and electronics. *Phys. Rev. Lett*, 58:2059, 1987.

[75] J. K. W. Yang and K. K. Berggren. Using high-contrast salty development of hydrogen silsesquioxane for sub-10?nm half-pitch lithography. *J. Vac. Sci. Technol. B*, 25:2025, 2007.